NANOLITER ELECTRONICS FOR WIRELESS CHEMISTRY

A Dissertation
Presented to the Faculty of the Graduate School
of Cornell University
in Partial Fulfillment of the Requirements for the Degree of
Doctor of Philosophy

by
Samantha Norris
May 2023

NANOLITER ELECTRONICS FOR WIRELESS CHEMISTRY

Samantha Norris, Ph.D.
Cornell University 2023

Experiments at the frontier of chemical and biological research increasingly require operation in very small fluid volumes for applications such as drug discovery, *in vivo* sensing, and microfluidics. This shrinking of sample volumes requires the development of a new toolkit for chemistry in environments inaccessible to macroscopic techniques. In this thesis, we show that microscale electronics is an invaluable tool for interacting with chemical environments at the microscale.

We begin by presenting optically powered microscopic devices that drive electrochemical synthesis under incident light. This innovation results in an electrosynthesis technique that is compatible with existing infrastructure for high-throughput drug discovery. We then discuss progress toward the development of a wireless microscopic electrochemical sensor that is capable of onboard computation and optical wireless data transmission. We show initial results of this sensor and use it to detect a change in fluid salinity. Finally, we discuss electrochemical propulsion methods, and demonstrate a device with onboard silicon electronics that propels itself through solution by producing and ejecting bubbles electrochemically. Each of these devices demonstrates a different aspect of the functionality of this platform for wireless chemistry. Most significantly, these devices pave the way for more complex functionality in the future.

BIOGRAPHICAL SKETCH

Samantha Norris was born in 1993 to her parents, Herb and Debbie. She was raised in the cornfields of central Illinois, noteworthy for nothing except their unhampered view of the night sky. Like any annoying little sister, she constantly imitated her older sister, Bethany. Despite the challenges of being first-generation college students, when Bethany got her Ph.D., Sam had to as well.

After changing majors too many times as an undergraduate at Illinois State University, she ended up graduating with a physics degree in 2016 while working for Profs. Charles Su and Rainer Grobe. She then joined Paul McEuen's group at Cornell, where she got to work on a wide range of absolutely wild projects like studying beating heart cells, implanting electronics into fruit flies, fabricating graphene and carbon nanotubes, and making microscopic robots.

As a grad student, Sam took advantage of the academic flexibility to travel to eight different countries and take up random hobbies like Spartan racing and snowboarding. After graduation, she'll be working at a startup in the Boston area developing implantable neural sensors.

To my cats, Melanie and Murphy.

ACKNOWLEDGEMENTS

Over the past seven years, I've had the remarkable privilege of interacting with some amazing people. First, my Ph.D. advisor, Paul McEuen. Paul always knew when to be patient and when to push me to be better. He's taught me an incredible amount of science but more importantly, how to think critically about the world, especially concerning whether birds are real.

There are so few people in the world that can say that they genuinely enjoy interacting with each of their coworkers, but I am one of them. First and foremost, a fellow McEuenite, Michael Reynolds. It's so rare that such an accomplished scientist is also an absolute joy to work with. His mentorship as an older graduate student was crucial to my development as a scientist, and his friendship means even more.

Thank you to my work besties, Conrad, Tanner, and Baris, for always being there for me. I'm glad that our friendship spread outside the lab and I'm excited to see what the future has in store for you guys! Conrad, thank you for the encouragement and commiseration as we both approach the end of our grad school experience. I've had the privilege of working with a lot of other grad students and postdocs – late-night talks at CNF with Yanxin, cider tastes with Kyle, mid-day ice cream with Kathryn, learning about entrepreneurship and science from Alejandro, and fantastic conversations with Zexi, Alice, Melody, Kemper, Qingkun, and Marcos.

I've gotten to work with people from all over Cornell as collaborators. From chemistry (Bartosz, Jonas, Samson) to biology (Tyler) to electrical engineering (Sunwoo, Daniel, Shahab), these relationships were invaluable.

A special thank you to the fellow residents of my second home, the CNF. The CNF staff, especially Jeremy Clark and Tom Pennell, have helped me with everything from nanofabrication woes to motorcycle repair to career advice. It's been a real privilege, and I'm going to miss you!

A special shout-out to my Spartan race crew – Allie, Nick Gotem, J.C., Rachel, Ally, and Erin. Thanks for training with me, and look forward to running many more with you guys.

Finally, my nerd friends: Jake, Daniel, Jim, Cullen, Siobhan and Jordan, Josue, Riley, Eric, Drew and Will, Diana, Janay, Corinne, Paul, Ashley, Other Sam, Kat, and Izzy. I love you all, and really don't know what I'd do without you. A special shoutout to my Swede-est friend, Marianne.

The love and support from my family cannot be understated, especially from my sister Bethany. I'm pretty sure we spoke everyday while I struggled through graduate school. She commiserated with me, encouraged me, and sent me vacuum-sealed stuffed cats. Most importantly, she and her husband Aron gave me the best nephew I could ever ask for, Addison.

Thank you to my dad, whose encouragement has been invaluable over the years. I love you, and thank you for being who you are.

Finally, a thank-you to my mom, who passed away from cancer in my fourth year of grad school. She was my biggest cheerleader, and after her passing I found a copy of my master's thesis (the A exam, to those familiar) on her bedside table. She was so impossibly proud of me and I wish she were here to watch me defend my Ph.D. I made it, Mom!

TABLE OF CONTENTS

LIST OF TABLES

LIST OF FIGURES

CHAPTER 1

INTRODUCTION

Less than three years after the beginning of the COVID-19 pandemic, one hardly needs to convince the reader of the significance of the microscopic world. After all, what serves as a more effective demonstration than the disruption of the global economy by a particle less than 100 nanometers in size? During the pandemic, we all became intimately acquainted with the microscopic world in another way as well – for many of us, the pandemic was the first time we were exposed to a key topic presented in this thesis: the world of small-volume chemistry.

After COVID tests were developed in late 2020, many of us recall regularly swabbing our nasal passages and inserting the swab into a small fluid-filled container. These vials, shown in Fig. 1.1a, contain a reagent to inactivate the virus and release the viral antigen for detection. The volume of this biochemical reaction, performed by many of us in our own homes, is about 1 mL.

As the world sought to reopen after lockdown, society required this sort of testing but on a massive scale. Cornell alone required the processing of 7,000 PCR tests per day at the height of the pandemic. The Cornell COVID-19 Testing Laboratory (CCTL) used automated fluid handling and measurement techniques to perform high-throughput analysis to meet this demand. These fluid-handling robots are optimized for high-throughput screening of significantly smaller fluid volumes, often 1-100 µL. One of these robots is shown in Fig. 1.1b.

High-throughput testing and experimentation with extremely small fluid volumes is ubiquitous in chemical and biological research. To continue the

COVID-19 example, this infrastructure for chemical screening allowed for the testing of nearly 12,000 existing drug compounds to identify candidates for COVID-19 therapies early on in the pandemic. This work, published in *Nature* in July 2020, utilized fluid volumes of less than 100 μL[21]. To further contextualize the fluid volume scales discussed in this thesis, we note that 1 nL corresponds to a typical volume for a microorganism like those shown in Fig. 1.1c.

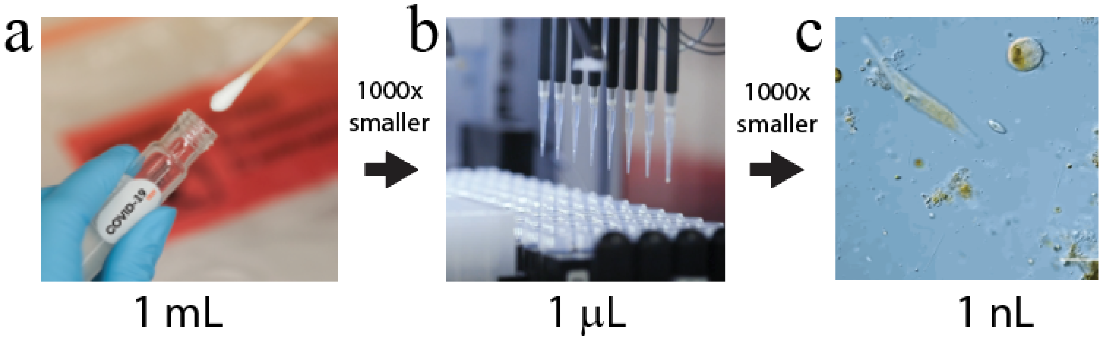

Figure 1.1: **Examples of Fluid Volumes from Nanoliter to Milliliter Scale**. **a)** Nasal swab and a container with reagent for rapid antigen testing. **b)** Automated fluid handling for COVID-19 testing at the Cornell COVID-19 Testing Laboratory. Image from news.cornell.edu. **c)** Microorganisms under a microscope, each containing a fluid volume on the order of 1 nL.

This shrinking of sample volumes for high-throughput experimentation demonstrates the need for a novel set of tools for interaction with these microscopic environments. Applications at the frontier of chemical and biological science increasingly require operation in environments like these – those inaccessible to usual macroscopic methods and devices.

With the miniaturization of integrated circuits as predicted by Moore's Law, microelectronics-based systems are uniquely poised to solve many of these challenges. As standard experimentation volumes in chemistry and biology have shrunk in the past few decades, electronics manufacturing has demonstrated the same capability for miniaturization. These fabrication approaches are innovative yet robust. The newest iPhone, for instance, has over 10 billion transistors less than 10 nm in size. Clearly, the development of electronics for very small volumes is not limited by their manufacturing.

In this thesis, we discuss microscopic electronics designed to operate in these small fluid volumes. These devices consist of onboard silicon electronics and are wirelessly powered using light. They occupy a volume in the nL range and can perform chemical synthesis, sensing, or locomote in their environment. Specifically, we demonstrate the use of these devices with the same infrastructure for high-throughput experimentation previously described.

1.1 Applications for Microscopic Electronics

The use of microscopic electronics for operation in previously inaccessible environments is not a novel concept. Here, we discuss existing research in these areas and some potential applications.

One of the most tantalizing applications for microscale electronics is implantation into the body for *in vivo* monitoring. For example, “Neuralink”[22] and “Neural Dust”[23] are millimeter-scale brain implants for neural sensing and stimulation that are powered by induction and ultrasound respectively. Other externally powered devices include inductively coupled sensors to measure blood pressure[24] and pulse rate[25] by integration with a stent in blood vessels.

Implantable sensors can also be powered by internal biological processes, such as pacemaker battery chargers that are powered by heartbeats via piezoelectricity[26] and biofuel-powered systems that use an onboard catalyst to generate electricity via reactions with surrounding biomolecules[27]. Implantable electronics have been developed to utilize nearly every method of power and data transmission available for macroscale systems, but some are particularly attractive for operation in vivo. In particular, ultrasound and induction are common powering and data transmission techniques due to their limited attenuation through tissue. Microscale circuits have also been integrated with the body without implantation in the form of skin-integrated circuits[28], smart contact lenses for tear-based glucose sensing[29], and photodiode-based retinal prostheses[30].

Although implantable systems for in vivo operation are obvious applications for microscale devices, the use of such devices in non-living environments is also advantageous for the advancement of biomedical engineering. Microfluidic channels for instance are commonly used for applications such as cell sorting[31], and low-cost diagnostics[32]. Standalone microscale sensors have been developed and placed in microfluidic channels for measurements of fluid conductivity[33], but generally for biological applications the electronics are integrated with the microchannels during fabrication, limiting their versatility.

Likewise, advancements in pharmaceutical drug discovery necessitate chemical synthesis and sensing in very small fluid volumes. The complexity and cost of organic chemical synthesis continues to increase – in fact, the cost to develop new drugs doubles about every nine years, referred to as Eroom's Law[34], in contrast to Moore's Law. As the complexity of synthesized molecules outpaces the capabilities of computational chemistry, new drug development increasingly takes advantage of combinatorial chemistry and high-throughput experimentation. These synthesis reactions are often performed in fluid volumes less than 1 µL with thousands performed simultaneously, and are thus ideal candidates for integration with microscopic electronic devices. A brief review of applications for small-volume chemistry is shown in Fig. 1.2.

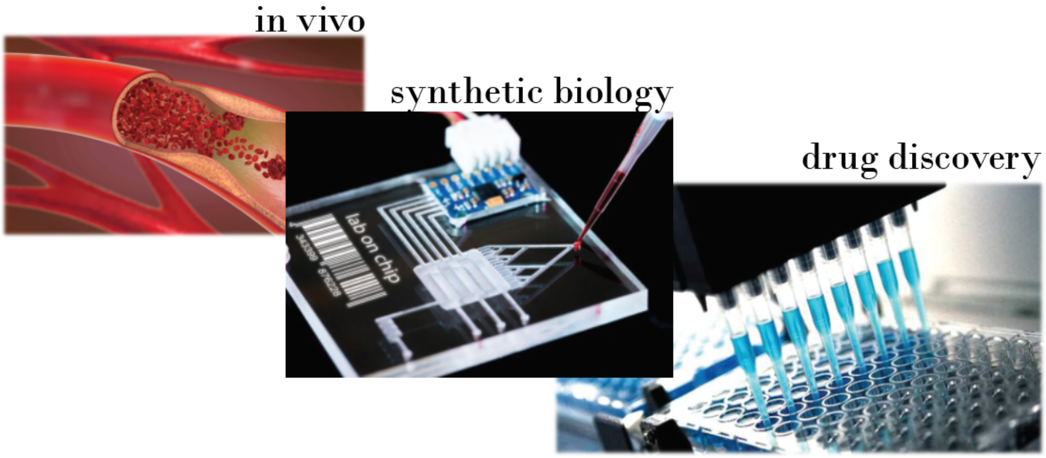

Figure 1.2: **Examples of Applications Utilizing Small Fluid Volumes**. Small-volume chemical reactions are crucial in *in vivo* environments, synthetic biology, and drug discovery in the pharmaceutical industry.

As the size of these electronic systems approaches the microscale, these devices benefit from advances in the field of microscopic robotics. The primary distinction between microscopic robots and other microscopic electronics is the ability for micro-robots to move in their environment. Much like microorganisms at a similar size scale, these micro-robots can swim or walk with a variety of mechanisms, and have demonstrated abilities such as cargo towing[35] and in vivo drug delivery[17]. In fact, we recently demonstrated the first truly autonomous micro-robot, which can walk on a solid-liquid interface with no input of information[13].

1.2 Electrochemistry and Microelectronics

For an electronic system to be of use in a microscopic chemical environment, we must consider how such a device would interact with its environment. Interestingly, microelectronic systems with onboard electrodes can affect the chemical composition of nearby fluid and vice versa, allowing for more in depth interaction between microscopic devices and their environment. This interplay between electronics and chemistry, called electrochemistry, is key to the operation of systems discussed throughout this thesis.

Electrochemically active molecules are those that can either gain (reduction) or lose (oxidation) an electron under an applied electric field, reducing the energy barrier for charge transfer between a nearby electrode and the surrounding fluid. In the most practical terms, the presence of a reduction/oxidation (redox)-active molecule near the surface of an electrode changes the current-voltage characteristics of that electrode, allowing the electrochemical behavior of that molecule to be quantified by purely electronic means. Likewise, electrochemical reactions can be performed simply by applying a voltage between two electrodes in a solution containing redox molecules. Redox molecules include those that have a net charge or are polar – including water – and are found in fluids across the natural world and synthetic chemistry, enabling the interaction between electronic devices and a wide range of environments.

1.3 Overview & Outline

The ultimate goal for this technology is the development of a wirelessly powered microscopic device that uses electrochemistry to perform a range of functions such as synthesis, sensing, onboard computation, wireless data transmission, and locomotion. Specifically, we envision a system that utilizes onboard photodiodes and LEDs for wireless power and data transmission and microtubes for bubble propulsion, all encapsulated in a device occupying about 1 nL of volume. A schematic of such a device is shown in Fig. 1.3.

In this thesis, we discuss progress towards the individual components of this device. Specifically, we demonstrate electrochemically fueled bubble-propelled microswimmers, electrolytic devices used in drug discovery, and initial steps toward the development of an integrated electrochemical sensor.

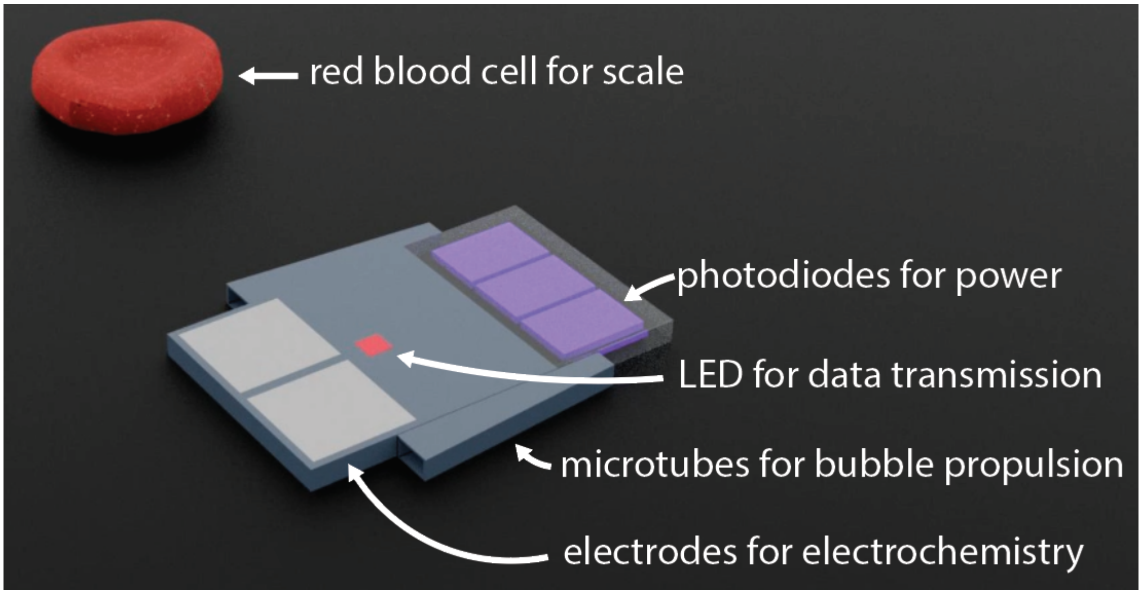

Figure 1.3: **Diagram of a microscopic device that can perform a range of functions.** A depiction of a device that can sense its environment, perform onboard computation, wirelessly transmit data, perform electrolysis, and locomote.

The chapters will be broken down as follows:

Chapter 2 – We will discuss the current status of high-throughput experimentation for pharmaceutical drug discovery and demonstrate optically powered devices to drive electrochemical synthesis in this context.

Chapter 3 – We will discuss prior work in electrochemical sensors, with a focus on wirelessly powered microscale systems.

Chapter 4 – We will demonstrate first steps toward the design of an optically powered microscopic electrochemical sensor used to identify and measure the concentration of nearby redox molecules.

Chapter 5 – We discuss prior work on microscopic robots that use electrochemistry as a method for propulsion, specifically electrochemical actuators.

Chapter 6 – We consider the use of bubbles for electrochemical propulsion and discuss existing work in this area.

Chapter 7 – We will present optically powered microswimmers that propel themselves through fluid by making and ejecting bubbles. These microswimmers operate in any aqueous solution by performing water electrolysis.

Chapter 8 – We will discuss the electrochemical dynamics of a bubble-producing electrode. Specifically, we consider tube-like electrode geometries such as those used in the microswimmers in Chapter 6.

Chapter 9 – We will summarize the results presented in this thesis, and discuss the future of microscale electrolytic devices and electrochemical sensors.

CHAPTER 2

ELECTROCHEMICAL SYNTHESIS FOR DRUG DISCOVERY

2.1 High-Throughput Experimentation for Drug Discovery

As the field of pharmaceuticaul drug discovery advances, the organic synthesis reactions required to develop new drugs have been increasing in complexity. As a result, pharmaceutical companies now increasingly rely on high-throughput experimentation (HTE) to synthesize new pharmacologically relevant molecules.

HTE is simply a game of combinatorics – by performing hundreds or thousands of chemical reactions simultaneously with slightly different parameters, the reaction products can be rapidly screened for novel and useful organic molecules. In combinatorial chemistry, chemical building blocks such as amino acids and organic molecules are combined in a systematic way to create a library of synthesizable compounds.

These experiments are performed in well plates. Examples of a 96-, 384-, and 1536-well plate are shown in Fig. 2.1a. One experiment is performed in each well. HTE often utilizes automated fluid handling and analysis techniques, so the overall plate size does not change significantly with the number of wells it contains. As a result, the fluid volumes for e.g. a 1536-well plate are incredibly small, often less than 1 µL. This significantly reduces the cost of synthesis with expensive reactants.

After the experiments, the reaction products in the well plates are analyzed using automated machines. In general, these analyses are spectroscopic in nature such as chromatography, mass spectrometry, nuclear magnetic resonance or IR spectroscopy. This experimental process is extremely common in the pharmaceuticaul industry, and most major pharmaceutical companies have devoted resources to enhancing HTE processes[36].

Recently, HTE-compatible infrastructure has been developed to enable photochemical synthesis, further extending the library of molecules that can be synthesized. Further, these reactions are often more selective, as specific molecules can be targeted with particular wavelengths without unwanted byproducts. In these reactors, shown in Fig. 2.1b, a standard well plate is integrated with an LED array underneath. Like standard combinatorial chemistry, these reactions can be performed simultaneously.

Similarly, by applying a potential between two electrodes in a well, electrochemical reactions that can occur that can further synthesize new molecules inaccessible to standard chemical or photochemical techniques, again expanding the library of synthesis reactions available to the pharmaceuticaul industry. The adoption of combinatorial electrochemistry in this manner has not occurred on a large scale in pharmaceutical drug discovery due to the difficulty of integrating HTE infrastructure with the wires and electrodes needed for electrochemical synthesis.

A preliminary electrochemical HTE-compatible reactor was developed recently by a group at Cornell[3]. This reactor, called HTe^{-}Chem, was developed for a 24-well plate and utilizes four current sources, each powering a row of six electrode pairs, wired in series. The reactor is shown in 2.1c. These electrodes are commercially available electrodes of varying materials that are several inches long and inserted into the well for electrosynthesis.

Although successful high-throughput electrochemical synthesis was performed with this device, we note several significant limitations to the scalability of this approach. For one, as the authors note, the power scheme is precarious. Because each cell is wired in series, if one electrochemical cell has insufficient conductivity to support the demanded current and voltage the synthesis efficiency of the entire row is changed.

In addition, the scability of this reactor toward smaller fluid volumes has several limitations. First, commercially available electrodes for electrochemical synthesis are too large to be inserted into smaller reaction volumes. In addition, there is no process available for the mass manufacturing of these electrode-plate-PCB designs.

Separately, high-throughput electrochemical reactors have been produced that utilize electrode arrays connected to CMOS electronics and multiplexers for drug discovery[37]. These electrode arrays require either multiplexers to control current flow with series/parallel wiring or independent power sources. These electrical components can be fabricated on the electrode array itself, but this drives up the cost of the well plate-sized arrays, rendering them prohibitively expensive for many applications. Alternatively, these components can be located off-chip, which requires making thousands of electrical connections, a notoriously challenging endeavor in electronics. In addition, these electrode arrays are non-trivial to customize and mass produce, limiting their versaility and cost effectiveness.

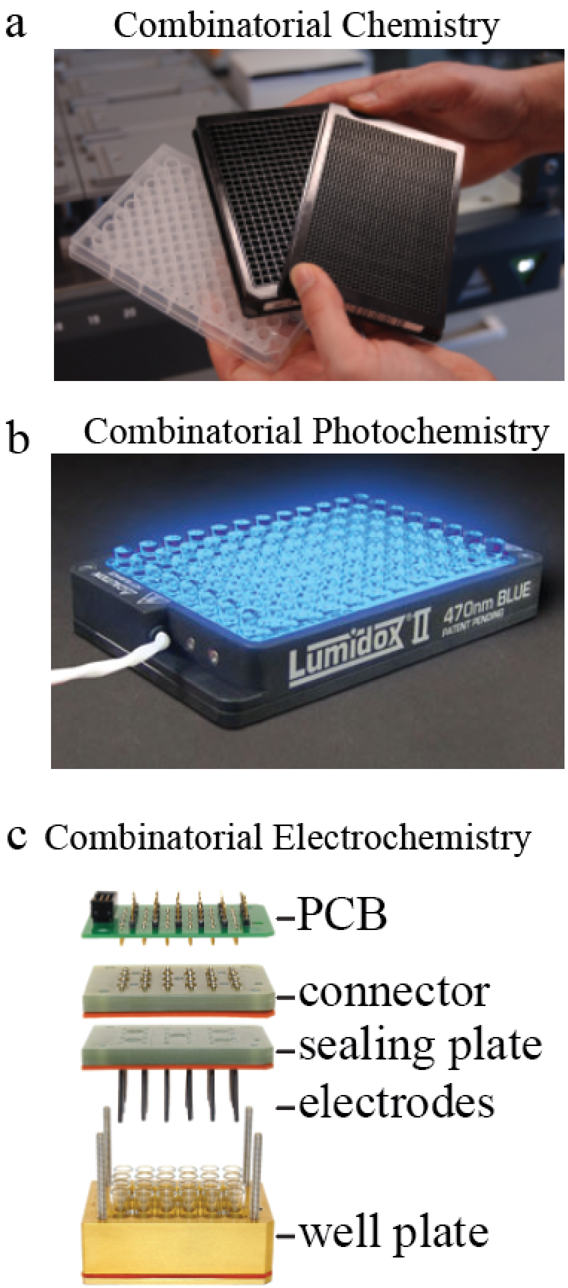

Figure 2.1: **Combinatorial Methods of Drug Discovery. a)** A 96-, 384-, and 1536-well plate used for combinatorial chemistry during HTE. Image adapted from [1]. **b)** A well plate integrated with an LED array for combinatorial photochemistry. Image adapted from [2]. **c)** A printed circuit board integrated with electrodes and a 24-well plate for combinatorial electrochemistry. Image adapted and modified from [3].

2.2 Optically Powered Devices for Electrochemical Synthesis

We have developed miniature devices capable of electrochemical synthesis that are compatible with existing infrastructure for high-throughput experimentation in drug discovery. These devices are referred to as SPECS - Small devices for Photo-induced ElectroChemical Synthesis.

SPECS are millimeter-scale devices that are mass produced at low cost and can be inserted into individual wells of a well plate to drive electrochemical synthesis while powered by incident light. They are designed to drive a current density similar to a standard electrochemical synthesis reaction while being powered by an LED array of a standard photochemistry reactor like that shown in Fig. 2.1b.

2.2.1 SPECS Operation and Characterization

A diagram of a SPECS device is shown in Fig. 2.2a, with a cross-section shown in Fig. 2.2b. Each SPECS is powered by 6-10 onboard silicon photodiodes wired in series. The open-circuit voltage of one photodiode is about 650 mV and the responsivity is about 0.3 A/W under 455 nm illumination. The maximum voltage applied by the SPECS is proportional to the number of photodiodes, and the current is proportional to the optical power incident on each diode. The diodes are wired in series with two external electrodes; the rest of the device is insulated so that the diodes and interconnects are not shorted to solution during experimentation.

The current-voltage characteristics of a SPECS device are shown in Fig. 2.2c.

For this measurement, microprobes were connected to the external electrodes with a DC triangle wave applied to the electrodes. The resulting current was measured with a transimpedance amplifier and PC oscilloscope. The result is a simple diode curve. The data shown in Fig. 2.2c is consistent with several photodiodes wired in series.

The exact current and voltage the SPECS produces under incident light is dependent on the impedance between the electrodes, which includes the electrode/electrolyte interface and the impedance of the fluid itself. Specifically, the operating point is the intersection of the I-V curves of the SPECS device and the other impedances in series with the electrodes. Examples of low- and high-impedance operating points are shown in Fig. 2.2c.

A constant current is desired for electrochemical synthesis so that the exact charge transferred to the molecules can be quantified during analysis, although the relevant impedance may change as the synthesis reaction proceeds. The SPECS shown in Fig. 2.2c apply a constant current up to 2V, and therefore are suitable for electrochemical synthesis when the total system impedance is less than 250 kΩ.

A scanning electron micrograph (SEM) of a SPECS is shown in Fig. 2.2d. Here, the bright spiral pattern corresponds to the two electrodes, which are the only conductive portions exposed to solution. The rest of the device is covered in insulating material and shows up as a darker material on the SEM. The SPECS drive electrochemistry at these electrodes, whose geometry and design can be trivially changed in the design stage of these devices.

An optical micrograph of a SPECS, like that shown in 2.2e, reveals that the device is optically opaque. This is intentional to prevent light from entering the chemical solution when there is a SPECS at the bottom of a well. This allows electrochemical synthesis to be performed without the risk of other undesired photochemical reaction byproducts.

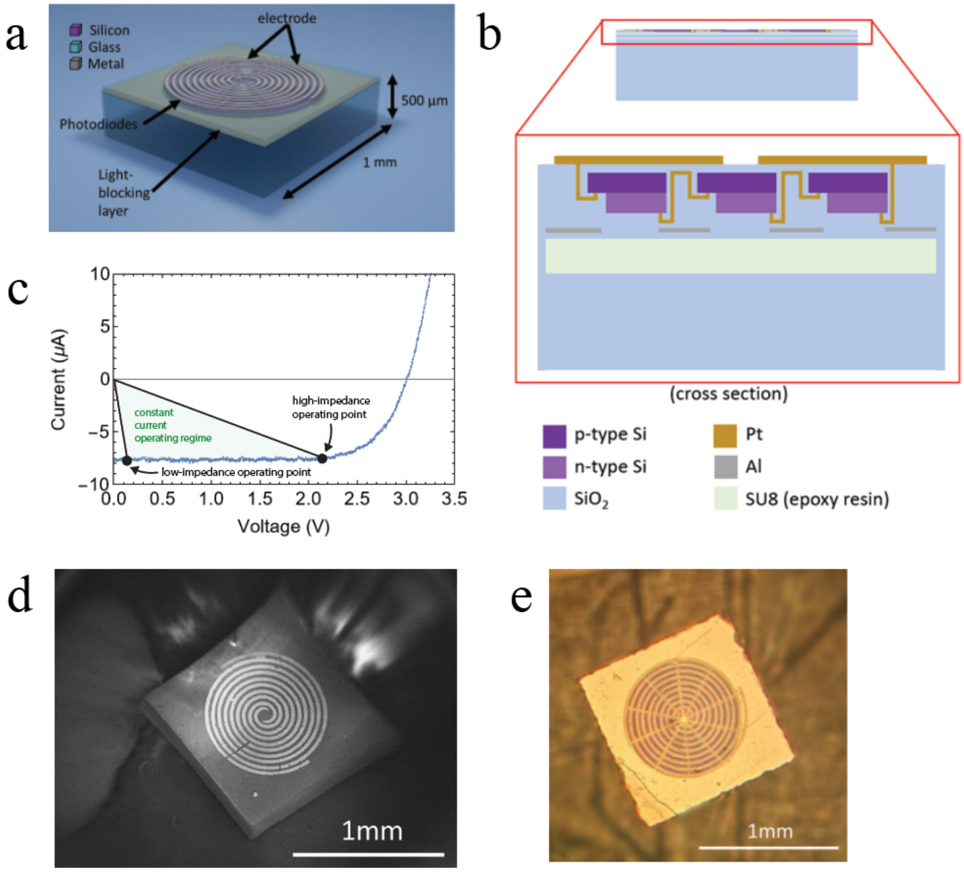

Figure 2.2: **SPECS diagrams and characterization. a)** 3D render of SPECS device showing photodiodes, light-blocking layer, and electrodes. **b)** Diagram of a SPECS cross-section showing the vertical Si P-N junction. **c)** Current-voltage characteristics of a SPECS device. **d)** Scanning electron micrograph of a SPECS showing the spiral electrodes on its surface. **e)** Optical micrograph of a SPECS.

2.2.2 Experimentation with SPECS

These devices are easily fabricated in massive parallel and then diced into separate devices for experimentation. A photo of a single SPECS on a human fingertip for scale is shown in Fig. 2.3a, with a pile of mass-produced SPECS shown in Fig. 2.3b.

These devices can be manipulated with a small suction tool or with tweezers – in the future, they are also fully capable of being manipulated with a commercial pick-and-place tool, allowing for more automatic integration with HTE reactors. These devices are mechanically rigid enough to be sonicated, allowing for the removal of fabrication-caused residue before experimentation. Before placement into the well plates, we test each device individually to confirm that the electrical connections are functioning properly.

In Fig. 2.3c. we see a SPECS device inside a micro-cuvette which is then inserted into a well plate for experimentation - this setup is the same as for combinatorial chemistry. This particular device is used to drive Shono oxidation, an electrochemical synthesis reaction shown in Fig. 2.3d, upper.

After placing SPECS in their respective wells using tweezers, the well plate is placed on a photochemical reactor like that shown in Fig. 2.1b. The photochemical reactor used in this experiment provides a light intensity of about 2 $kW/\mu m^2$ at 455 nm. Given the responsivity of the SPECS at this wavelength, we'd expect them to provide a current of about 10 µA. The reaction proceeds for a similar timescale as a standard combinatorial chemistry experiment, which can take several hours to react with all the molecules in the solution.

After the experiment, the reaction products are analyzed using automated spectroscopy tools. For this reaction, nuclear magnetic resonance spectroscopy was performed for each well on the plate. One sample data set from this run is shown in Fig. 2.3d.

The reaction byproducts of this particular oxidation reaction are identified by a pair of peaks in the NMR spectrograph shown in Fig. 2.3d for the reaction performed by the SPECS. In contrast, a well with the same reaction mixture but no SPECS did not produce the desired results. We have demonstrated the use of SPECS for a variety of electrosynthesis reactions using photochemical reactors in a standard well plate.

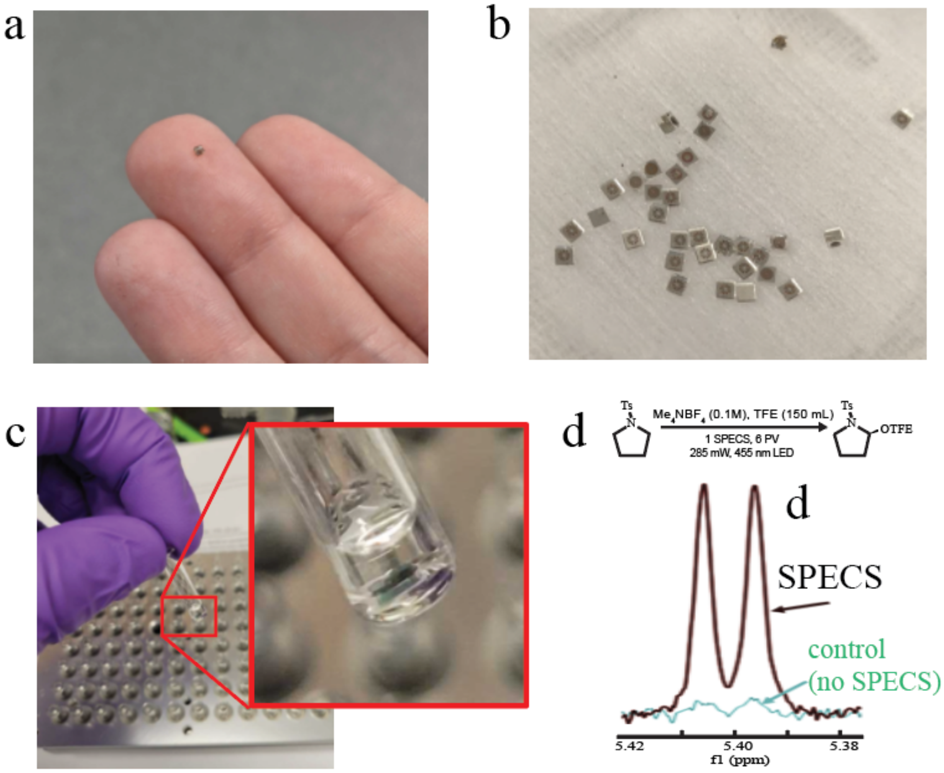

Figure 2.3: **SPECS Images and Experimental Results.** **a)** A SPECS on a human fingertip. **b)** Multiple SPECS after fabrication. **c)** SPECS in a micro-cuvette used in a standard HTE reactor. **d)** Nuclear magnetic resonance spectrograph of reaction products with and without a SPECS showing successful electrochemical synthesis during a Shono oxidation.

2.2.3 Fabrication

The primary difficulty of the SPECS fabrication is that these devices remain at the bottom of the wells during experimentation. To be integrated with a standard photochemical reactor, they require bottom-side illumination and top-side electrodes so that they can perform electrochemical synthesis on the fluid on top of them. Because the photodiodes are fabricated on an opaque wafer, the integration of SPECS onto a transparent substrate requires special consideration.

A detailed process flow is shown in Fig. 2.4. The silicon photodiodes are fabricated in massive parallel using traditional planar lithography. The doping for the P-N junctions is done via diffusion doping of a silicon-on-insulator (SOI) wafer with phosphosilicate spin-on glass and followed by etching to produce a vertical junction. Ti-Pt is then deposited for both the contacts to the diodes and to wire up the individual photodiodes.

After production of the photodiodes and patterning of an Al light-blocking layer, the sample containing the diodes is thermally bonded to an SiO_2 substrate with SU-8 to increase the mechanical stability of the SPECS. The handle Si of the SOI is then dry etched, and further lithography performed to create electrodes and wire them to the diodes. The SPECS can then be separated via dicing.

One clear advantage of using traditional lithography to produce the SPECS is their customizability. The possible synthesis reactions that can be performed with a SPECS depends on its electrode material. With this fabrication approach, SPECS can be fabricated with almost any thin film material as its electrode material, and SPECS with different geometries and electrode materials can even be fabricated on the same wafer. We also note that before the SU-8 thermal bond, the SPECS entirely consist of CMOS-compatible components, and can therefore be integrated with more complex circuitry.

In addition, the mass production of these devices results in a very low cost per device. For 1 mm SPECS on a 100 mm wafer, the fabrication cost per device can be less than 10 cents. Especially compared with the other costs associated with a single high-throughput experiment for drug discovery, this cost is small enough to render the SPECS effectively disposable.

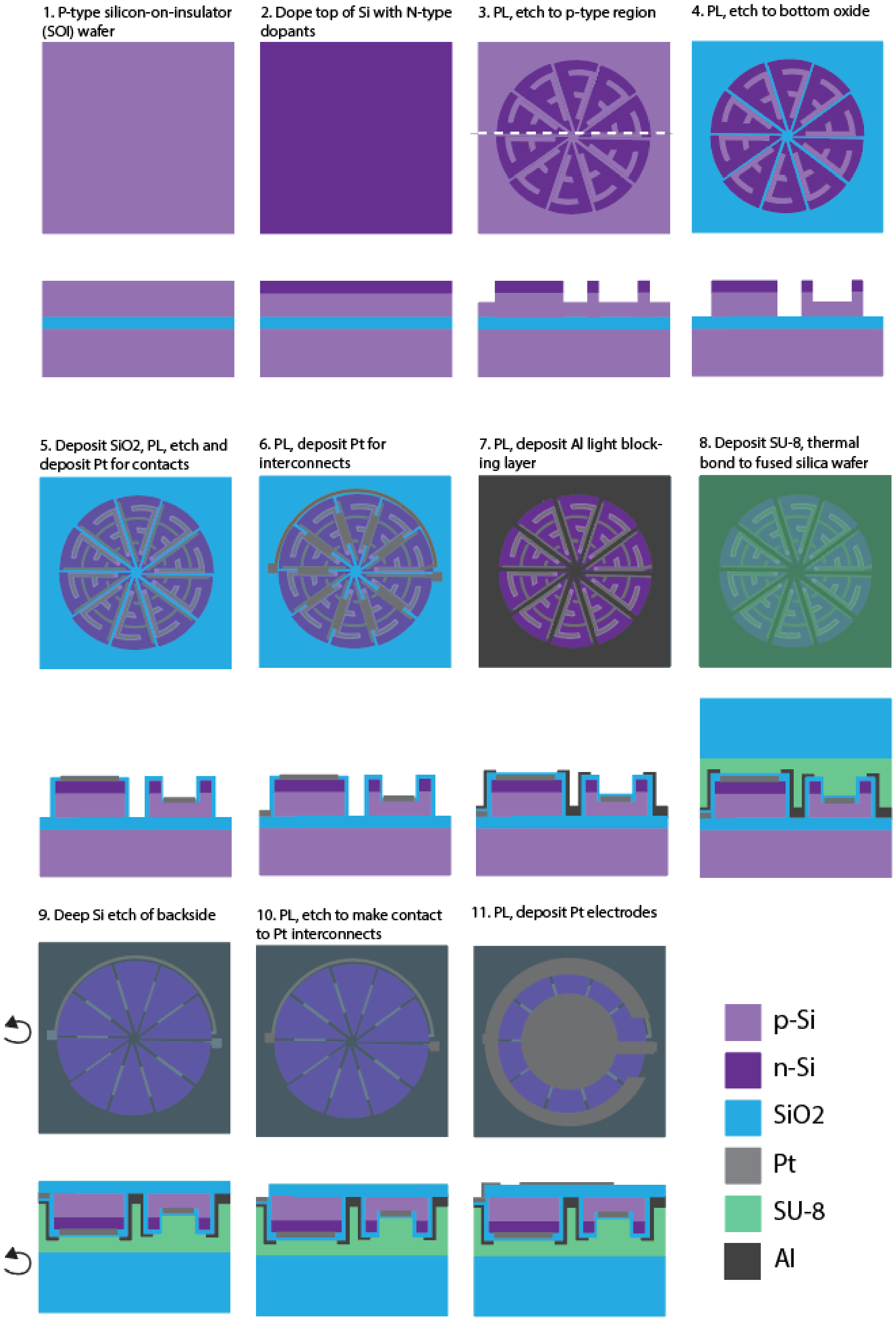
1. P-type silicon-on-insulator (SOI) wafer

2. Dope top of Si with N-type dopants

3. PL, etch to p-type region

4. PL, etch to bottom oxide

5. Deposit SiO2, PL, etch and deposit Pt for contacts

6. PL, deposit Pt for interconnects

7. PL, deposit Al light blocking layer

8. Deposit SU-8, thermal bond to fused silica wafer

9. Deep Si etch of backside

10. PL, etch to make contact to Pt interconnects

11. PL, deposit Pt electrodes

Figure 2.4: **SPECS Fabrication.** Step-by-step process flow for manufacturing SPECS.

2.2.4 SPECS Device Yield

We now turn to a more detailed discussion of electrochemical synthesis reactions and how to quantify the success of a reaction. Specifically, we want to determine the efficiency of these reactions performed by the SPECS and compare this efficiency to that of standard electrosynthesis techniques.

In the most generic electrosynthesis reaction, an electrode in a solution containing molecules A and B drives a reaction $A + B \rightarrow AB$. The exact mechanism depends on the particular reaction, but in general the charge transfer induced at an electrode with an applied potential can be thought of as a catalyst for these reactions. We have used SPECS to perform two types of simple electrochemical synthesis reactions called oxidation and bromination. In these reactions, oxygen- or bromine-containing compounds are added to organic molecules via electrolysis.

The amount of product synthesized during a reaction can be quantified spectroscopically by comparing the spectrographs of the reaction product (AB) to a solution of known concentration. The product yield is the fraction of reactant (A or B) that is converted into product (AB). Once we know the total amount of synthesized product produced in a given time, we can estimate the average current produced during the reaction.

The product yield and estimated average current for six SPECS performing an electrosynthesis reaction are shown in Table 2.1. Three of the SPECS, denoted in green, produced an average current of about 10 μA. This is consistent with the current expected for this light intensity and wavelength. These results are typical for electrosynthesis results with the SPECS – some devices produce the expected current, while others produce an average current significantly lower. The experimental yield for the SPECS in these experiments tends to be 30-50%.

After inspection, we find that the primary failure mechanism during experimentation is fluid penetration through the SU-8 bonding layer due to insufficient encapsulation. Fluid reaching the device can cause failure as some electrosynthesis reactions utilize volatile chemicals that can etch the photodiodes on the SPECS. More generically, bonding polymers tend to be quite reactive, causing unwanted reaction byproducts.

Moreover, the use of a polymer causes a drop in yield during their manufacturing as well. During fabrication, we find that some SPECS delaminate from the bonding polymer during exposure to fluid after thermal cycling such as metal deposition, photoresist baking, or etching. This was independent of bonding polymer material (SU-8, spin-on glass, photoresist) and thickness (from 500 nm to 20 μm). We now turn to a discussion of polymer-free fabrication approaches for the SPECS.

Sample Number	Product Yield (%)	Average Current (µA)
1	3	0.5
2	4	0.7
3	68	12
4	59	9.7
5	59	9.7
6	2	0.3

Table 2.1: **Experimental Performance of SPECS.** Product yield and average current from six SPECS during the bromination of organic compounds.

2.2.5 Polymer-Free Fabrication Approaches

We here consider two other nanofabrication techniques for the manufacturing of the SPECS. As a reminder, the main challenge to overcome here is the use of bottomside illumination with topside electrodes.

In Fig. 2.5a, we depict a fabrication approach that utilizes ″windows″ etched through the backside of the chip to allow incident light to interact with the photodiodes without being blocked by the handle silicon. Here, the photodiodes are manufactured on-chip with topside electrodes using standard planar lithography. After the photodiode fabrication and connection to electrodes, we use contact lithography with backside alignment to pattern and etch holes in the back side of the Si handle wafer through to the bottom oxide beneath the photodiodes.

This ″backside windows″ method yielded very promising preliminary results. To test the mechanical stability of this thin photodiode-containing membrane, we produced devices on chip as shown in Fig. 2.5a. These devices were able to perform successful electrochemical synthesis. The device yield for this fabrication approach was about 50%. The yield increased with bottom oxide thickness and with decreasing window dimension. The next step in the investigation of this fabrication approach is fabrication on a thicker wafer to increase the stiffness of this windowed section.

Yet another approach, shown in Fig. 2.5b, is the use of through-silicon vias (TSVs) to electrically connect the top and bottom of the device. In this technique, silicon photodiodes are manufactured as usual, and then a via is etched all the way through the chip before electrodes are patterned on the other side. This is a common approach in the literature, but has some challenges. Specifically, a deep silicon etch results in fluoropolymer deposition on the sidewalls, making it difficult to insulated the deposited metal vias from the handle silicon.

During experimentation with the TSV approach, we found that the via was difficult to insulate electrically, such that the anode and cathode of the SPECS were shorted through the handle silicon, reducing the current flow through the solution. As a result, the device yield during electrochemical synthesis for this approach was near zero, with no obvious path forward for increased yield. The TSV approach also presents scalability challenges, as we found the optimal TSV size to be 100 µm, adding significant size to the SPECS.

SPECS have demonstrated functionality using the bonding polymer approach as mentioned earlier, and there are additional polymer-free fabrication approaches that show promise, especially the backside window method. In general, since the key components of the SPECS are CMOS-compatible, their fabrication is quite versatile and we anticipate further refinement in the future.

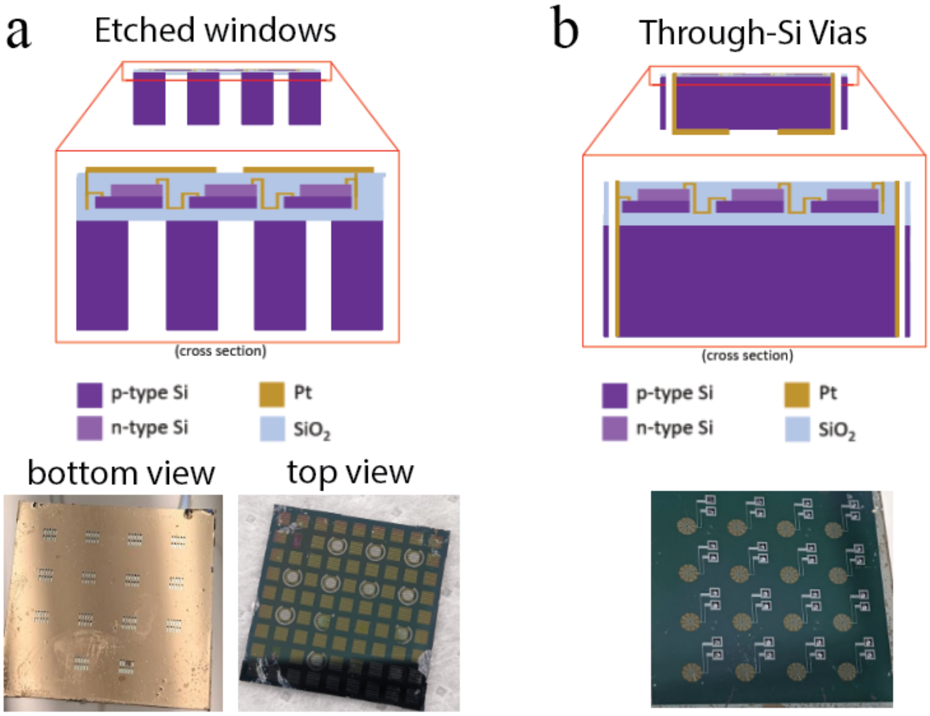

Figure 2.5: **Non-polymer Methods for SPECS Fabrication. a)** Diagram showing holes through the backside of an SOI wafer to allow light to hit the onboard diodes. **b)** Diagram showing through-silicon vias used to electrically connect the top side of the chip to the bottom side.

2.3 Outlook for SPECS

We have successfully demonstrated electrochemical synthesis with SPECS, optically powered microscopic devices that are easily integrated with existing infrastructure for high-throughput experimentation. We show that these SPECS are capable of providing a voltage and current typical for electrosynthesis reactions but without wires or power supplies.

In the future, we look forward to using these SPECS to perform thousands of small-volume experiments simultaneously, rivaling standard combinatorial chemistry as a method for drug discovery. Specifically, we aim to use these SPECS to drive novel electrosynthesis reactions made possible by the broad range of electrode materials that are easily integrable onto the SPECS. The promising future of the SPECS is enabled by our collaboration with the Lin group at Cornell, who will continue the fabrication and experimentation with the SPECS.

CHAPTER 3

A REVIEW OF ELECTROCHEMICAL SENSORS

In the last chapter, we demonstrated novel microscopic devices that drive electrochemical synthesis for drug discovery. The integration of electronics with electrochemistry for miniature devices, however, is not new. We now turn to discuss the most prevalent application for miniature devices that perform electrochemistry – electrochemical sensors.

Here, we briefly describe the general principles behind electrochemical sensing and then discuss some miniaturized sensors. The literature on electrochemical sensors is vast, so we will limit our discussion to electrochemical sensors smaller than 1 cm in size. Specifically, we consider those can wirelessly receive power and transmit data. Most of the sensors to be discussed here are optimized for *in vivo* applications, but many of the approaches used are generic to sensing in any small fluid volume.

3.1 Operating Principles for Electrochemical Sensing

The most common mode of operation for microscopic electrochemical sensors is utilizing the same methods of electrochemical analysis that are available in macroscale experiments. In these experiments, redox reactions are performed at electrodes, and the effect of these reactions on the charge-transfer characteristics of the electrodes is measured, revealing details about the surrounding electrochemical environment.

One common technique, called voltammetry, consists of applying a known electric potential waveform to a working electrode with respect to a reference electrode in the solution of interest, and measuring the current between the working electrode and a separate counter electrode. A typical electrode setup for this experiment at the macroscale is shown in Fig. 3.1a. A current can also be applied and the potential measured, called potentiometry.

As a simple example of voltammetric electrochemical sensing, we consider a triangle wave potential applied to a working electrode while the resulting current is recorded, called a cyclic voltammogram, as shown in Fig. 3.1b. For solutions containing redox molecules, there is a current peak in both the forward and reverse sweeps; the potential at which this peak occurs is the redox potential of the molecule of interest, allowing identification of the molecules in the solution.

The peak current amplitude is directly proportional to the concentration of analyte in the solution[38], allowing one to quantify the amount of analyte in a solution just by performing a simple electrical measurement. For example, cyclic voltammograms are shown in Fig. 3.1c for different concentrations of paracetamol along with the peak current for each concentration. This method of electrochemical analysis is very common at the macroscale. In the next section, we turn to the miniaturization of these electrochemical analysis techniques.

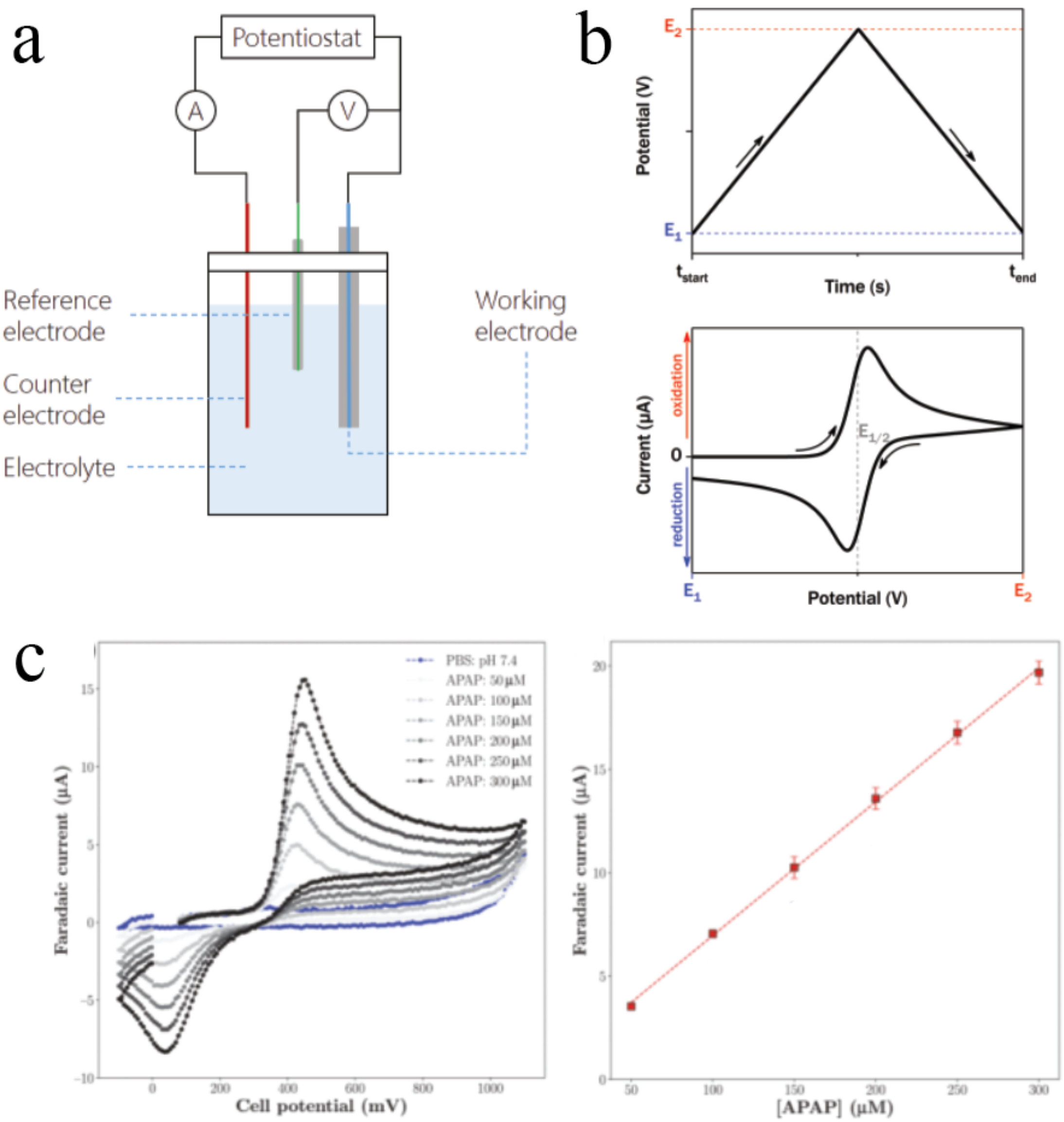

Figure 3.1: **Standard Methods for Electrochemical Analysis. a)** Standard setup for voltammetry experiments. Figure adapted from [4]. **b)** Voltage sweep (top) and resulting current (bottom) for cyclic voltammetry in a solution containing a redox molecule. Figure adapted from [5]. **c** Cyclic voltammograms for varying paracetamol concentrations, and the relationship between the peak current and concentration. Figure adapted from [6].

3.2 Scalability of Electrochemical Sensing Techniques

The principles of electrochemistry discussed above apply to electrochemical devices at any size scale. In fact, we note that the sizes of electrodes used for sensing and synthesis span 10 orders of magnitude - from nanotubes[39] to macroscale water electrolysis units[40]. The subtleties of these electrochemical dynamics, however, depend on electrode size and geometry. Here we consider the advantages and challenges of performing electrochemical sensing at very small size scales.

First, the miniaturization of sensing electrodes allows for higher temporal resolution. The time constant τ for a sensing electrode – the time that the system takes to respond to an electrochemical change – is proportional to its double layer capacitance C_{DL} and the fluid resistance R_F by $\tau = C_{DL}R_F$. The electrode capacitance is related to the electrode area A by $C_{DL} \propto A$. The fluid resistance can be approximated by the resistance of the cube of fluid on top of the electrode; the resistance of this cube of fluid is inversely proportional its linear dimension, so $R_F \propto 1/\sqrt{A}$. The total time constant, then, scales as $\tau \propto \sqrt{A}$. It is therefore advantageous to use small electrodes for rapid electrochemical sensing.

On the other hand, larger electrodes can pass more current, resulting in a higher sensitivity[38]. As a result, many miniaturized sensors have electrodes integrated with functional nanomaterials such as enzymes in order to increase sensitivity and specificity for the desired reaction[41].

One additional consideration is the integration of these sensors with a reference electrode. By definition, a reference electrode serves as the ”ground” electrode in an electrochemical experiment, and the electrode is chosen to minimize the voltage drop between the electrode and electrolyte. This is easiest with a large electrode (i.e., low impedance); as a result, designing a sensor to be used with small electrodes requires careful consideration.

The most significant advantage of electrochemical sensor miniaturization is simply the physical footprint of the device. Especially for *in vivo* applications, shrinking down the overall sensing devices to minimize invasiveness is crucial. Keeping in mind the scalability considerations above, we note that microscopic devices can use the same forms of electrochemical analysis described previously, and we now turn to the fascinating world of miniature electrochemical sensors that have been developed recently.

3.3 Sub-Centimeter Electrochemical Sensors

First, let us carefully define the limits for our discussion of electrochemical sensors. More than their size, we are interested in the miniaturization of these sensing technologies, so will not discuss the enormous space of handheld or point-of-care sensors. Specifically, we will consider electrochemical sensors that are 1 cm in size or smaller. We also only discuss sensors that can transmit data and receive power wirelessly through onboard circuitry.

Miniaturized electrochemical sensors can be divided into two categories: those with small sensing components that are integrated with larger devices for wireless data transmission, and those that are integrated with small onboard wireless receivers/transmitters.

Microscopic sensors that are integrated with larger devices for power/data transfer have successfully transcended into commercially available products, especially for glucose sensors which comprise 85% of the biosensor market[42]. As an example, we show in Fig. 3.2a the FreeStyle Libre 2, a commercially available glucose sensor. This sensor consists of a macroscale component that remains on the outside of the skin for Bluetooth connectivity, and an attached needle used to take electrochemical measurements of glucose levels inside the body. Although the exact measurement protocols for commercially available sensors are often proprietary, similar sensors have been developed that utilize microneedle arrays and amperometric techniques to measure glucose concentrations in human blood while transmitting via Bluetooth[43]. Many of these sensors are coated with an enzyme to increase reaction sensitivity; for glucose, this is often glucose oxidase.

Even without integration with invasive microneedles, microscopic sensors can still perform biological measurements with sweat[44, 45, 46, 47], saliva[48, 49], tears[8], or gas in joint cavities[50]. As one example, Fig. 3.2b shows a glucose sensor integrated with a contact lens. Like other sensors discussed thus far, there is a several-cm onboard structure for wireless data transfer and power.

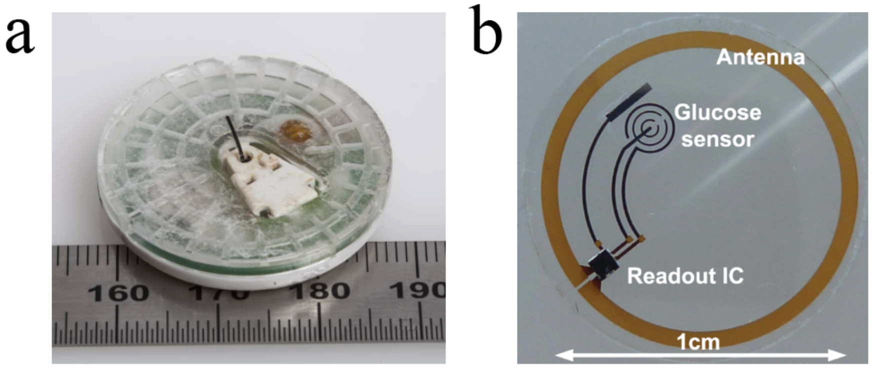

Figure 3.2: **Examples of Electrochemical Sensors with Macroscopic Components for Data Transfer. a)** The FreeStyle Libre glucose sensor, with a needle for insertion into the skin and a macroscopic portion that sits outside the skin for wireless data transmission and powering with Bluetooth. Image adapted from [7]. **b)** Electrochemical electrodes integrated onto a contact lens for glucose sensing. The data transmission occurs via induction by the onboard coils. Image adapted from [8].

Although not yet commercially available, sensors have also been developed that combine a sensing unit and a wireless power/data transfer unit into a sub-cm package. For instance, Fig. 3.3a shows an implantable amperometric sensor for the measurement of local lactate concentrations and pH. This sensor has been tested in an anatomical phantom of human breast tissue and uses on-board piezoelectric transducers and external ultrasound to power the device and transmit data[9]. Sensors of a similar device size have been used to measure neurotransmitters in the brain (Fig. 3.3b)[10], glucose concentrations in blood[51],, and gastric activity in the GI tract[52].

Very recently, electrochemical sensors have been developed that utilize CMOS electronics from a commercial foundry for truly miniature sensors. One example, shown in Fig. 3.3c, is an RF-powered mm-scale glucose sensor that operates via amperometry and is manufactured with standard lithography. The same group also published on a similar sensor operating in blood[53].

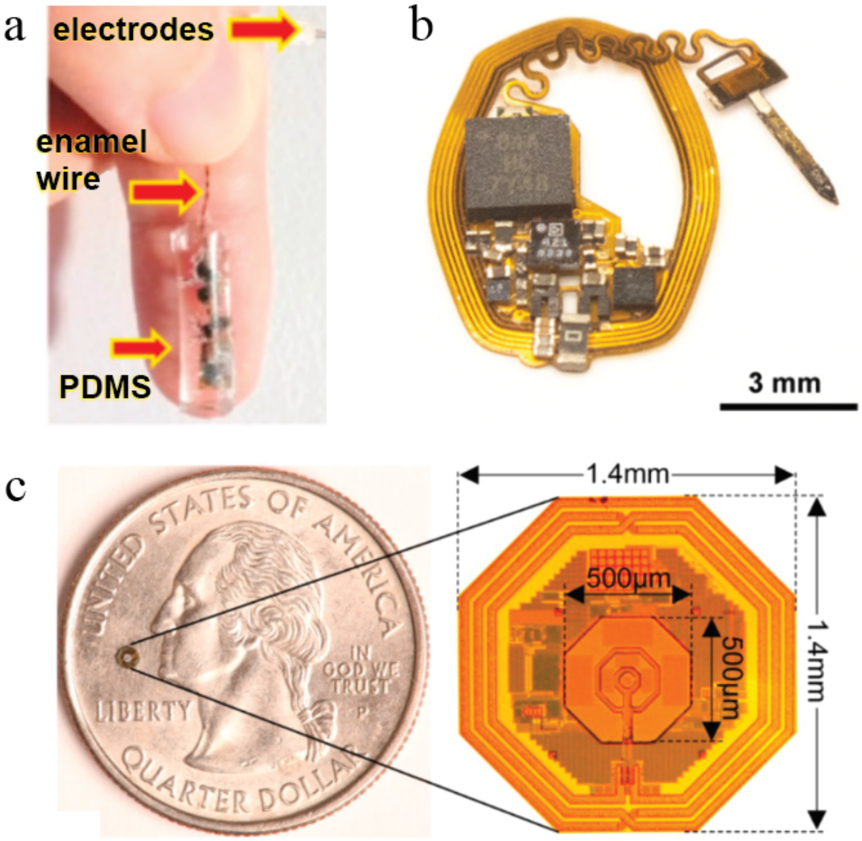

Figure 3.3: **Examples of Sub-cm Electrochemical Sensors. a)** Implantable pH and lactate sensor powered by onboard piezoelectric tranducers with a human finger for scale. Image adapted and modified from [9]. **b)** Implantable neurotransmitter measurement scheme powered by an onboard antenna. Image adapted from [10]. **c)** Implantable RF-powered glucose sensor manufactured using CMOS from a commercial foundry and planar lithography. Image adapted from [11].

With the invention of electrochemical sensors that can be manufactured in massive parallel as shown in 3.3c, it is apparent that the limitation to further miniaturization is not device fabrication. Instead, the challenge becomes the miniaturization of power receivers.

The small sensors demonstrated here use ultrasound or RF signals to receive power, both of which face additional challenges for further miniaturization. As piezoelectric transducers (for ultrasound) and antennae (for RF) decrease in size, the wavelength of the incoming signal must also decrease to maintain the same transduction efficiency. However, attenuation of these signals is more pronounced at lower wavelengths, so the efficiency of power transfer decreases with miniaturization of the device. In contrast, by using light for wireless power transmission, microscopic sensors can be designed to operate in ambient light, like a well-lit room or the outdoors on a sunny day.

3.4 Microscopic Sensors Developed at Cornell

Optical power is easily scalable to microscopic sensors, as incoming light beams can be easily collimated and focused to power small devices from a significant distance. To this end, our collaborators at Cornell have developed a platform for optically powered sensors. These sensors have onboard CMOS circuits and have been developed for biological applications such as neural sensing. These devices are referred to as MOTEs: Microscale Optically Transduced Electrodes.

A diagram of these devices is shown in Fig. 3.4a. The MOTES are passive voltage sensors consisting of two onboard electrodes (denoted as $V_{IN}+$ and $V_{IN}-$), an onboard PV-LED, and CMOS circuitry from a commercial foundry

(X-FAB, TSMC). The potential difference between the two external electrodes is encoded into light pulses of the PV-LED, allowing the voltage data to be wirelessly transmitted. The PV-LED is also used to optically power the MOTE.

After receiving the circuits from the foundry, these devices undergo post-processing in the Cornell Nanoscale Facility (CNF). The AlGaAs PV-LEDs are transferred to the MOTEs, which are then released in parallel from the substrate. An SEM of a MOTE released from the substrate is shown in Fig. 3.4b.

This optically powered voltage sensor is a crucial launch point for the development of other similar microscopic sensors. Specifically, we build off this technology to take the first strides toward a microscopic electrochemical sensor.

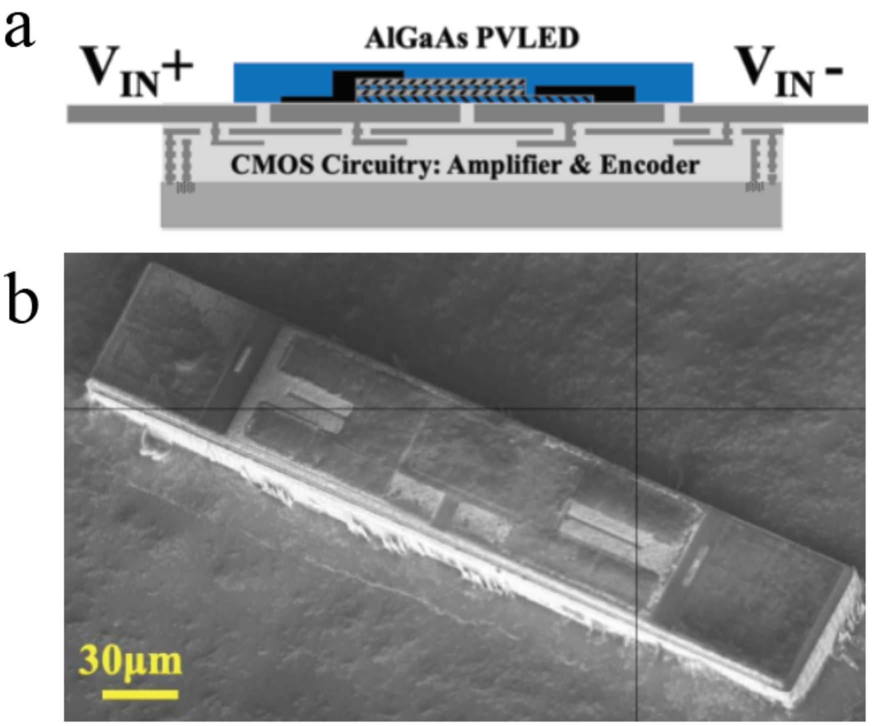

Figure 3.4: **Optically powered microscopic sensors at Cornell.** **a)** Diagram of MOTE showing electrodes for input, and an onboard PV-LED for power and data transmission. Image adapted and modified from [12]. **b)** Scanning electron micrograph of a MOTE released from the substrate. Image adapted from [12].

CHAPTER 4

THE REMOTE: A MICROSCOPIC ELECTROCHEMICAL SENSOR

Here, we demonstrate the first steps toward a wireless microscopic sensor for performing electrochemical measurements in small fluid volumes. We call these devices ReMOTES: Redox Microscale Optically Transduced Electrode Sensors. ReMOTES use light for power and data transmission and utilize onboard CMOS electronics for advanced computation. We describe the measurement scheme for these sensors and report on the design and characterization of the first generation ReMOTES used to measure salinity. We then discuss future plans for ReMOTES that can be used for redox molecule sensing.

4.1 Electrochemical Analysis Scheme for the ReMOTES

The ReMOTE utilizes constant-current chronopotentiometry to measure the electrochemical properties of its surroundings. In this electrochemical analysis technique, a constant current is applied between two electrodes, driving electrolysis in the solution near the electrodes. This change in the electrochemical properties of the solution affects the voltage on the electrode, which is simultaneously measured.

The effect of a constant current on the electrode potential in this measurement scheme is depicted in Fig. 4.1a. There are three regions in the voltage trace that give information about the chemical environment near the sensor.

I. The current i applied to an electrode at zero potential causes the electrode potential to rise. This current is comprised of a Faradaic component i_f and a capacitive current i_c such that $i = i_f + i_c$. The former is used to drive redox reactions in the solution at a constant rate proportional to i_f, and the latter charges the double-layer capacitance of the electrode. When the concentration of redox molecules is very low such that $i \approx i_c$, the electrode potential V increases linearly as $dV/dt = i/C$, where C is the electrode double-layer capacitance.

II. If redox molecules are present in the solution, the electrode potential rate of change decreases as it approaches the formal potential of these redox molecules, allowing them to be identified by their unique redox potential.

III. When the redox molecules near the electrode have been reacted with, charge transfer is limited by the diffusion of unreacted molecules to the electrode, and the electrode potential again begins to rise toward the next-lowest formal potential for redox molecules in the solution. The time before the potential rises is related to the concentration of redox molecules near the electrode and their diffusion coefficients, allowing the chemical components of the solution to be quantified.

A diagram of a ReMOTE is shown in Fig. 4.1b. Each device consists of several onboard silicon photodiodes for power, a micro-LED for optical data transmission, and two external electrodes for potentiometry. During fabrication, the entire device is encapsulated in oxide to ensure that the exposed electrodes are the only pathway for the contained electronics to interact with their chemical environment.

The ReMOTE performs constant current potentiometry by applying 10 nA to one electrode. The other electrode is held at ground for the device, such that current flows from one electrode to the other. The potential at the electrode with the applied current is encoded into pulses of the onboard LED. We designed the circuitry for the ReMOTE to be produced in a commercial foundry; its internal components and circuit layout are shown in Fig. 4.1c.

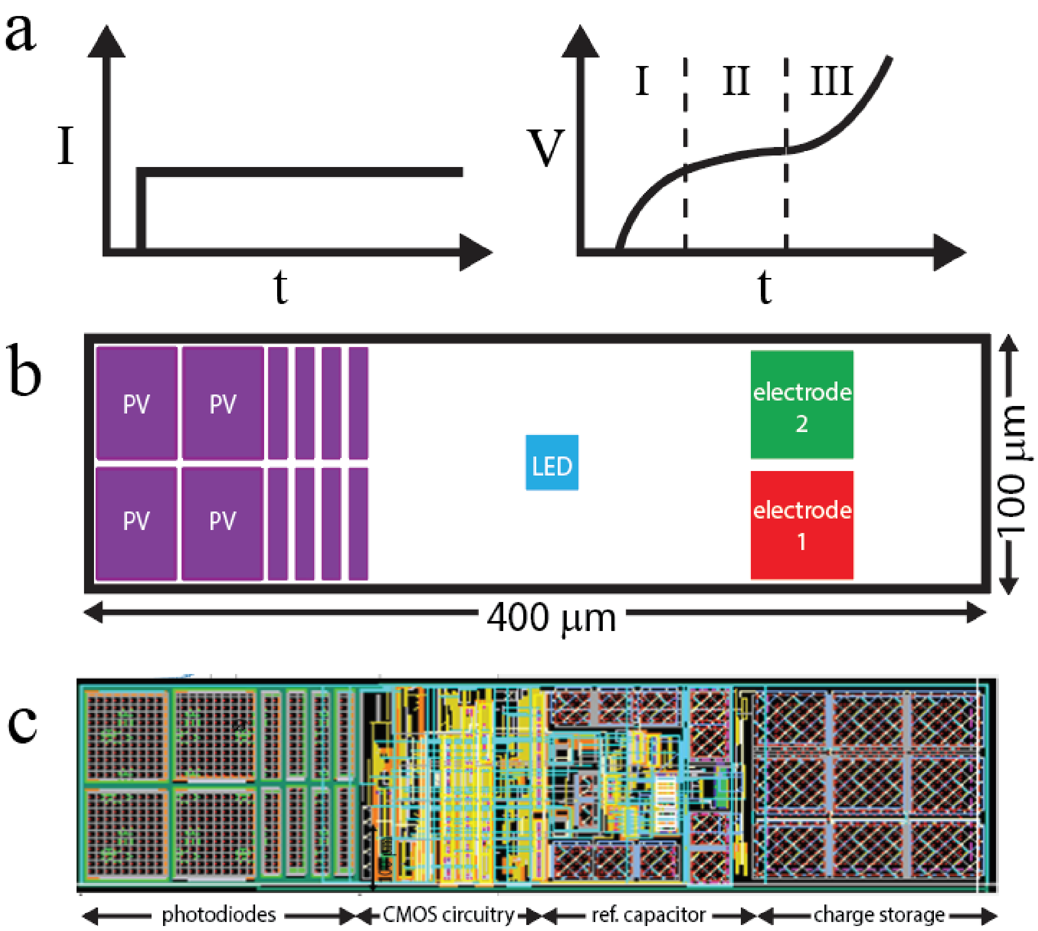

Figure 4.1: **ReMOTES Measurement Scheme and Device Overview.** **a)** The applied current trace and voltage response typical of constant-current chronopotentiometry in a solution containing redox molecules. **b)** Basic diagram of a ReMOTE showing photodiodes, micro-LED, and the two exposed electrodes. **c)** Physical circuit layout of the ReMOTE.

4.2 System Overview of the ReMOTES Circuit

The development of a potentiometric sensor that can wirelessly transmit data to the outside world requires advanced onboard computation that is only possible through CMOS circuitry. To this end, we have designed the circuit for the ReMOTE in Cadence *Virtuoso* to be manufactured in a commercial foundry, X-FAB. Like the MOTE, these devices will be integrated with an LED and released from the substrate in post-processing after receiving the circuits from the foundry.

A block diagram of a ReMOTE device is shown in Fig. 4.2a. The silicon photodiodes power a proportional-to-absolute-temperature (PTAT) current source to ensure a stable current supply over a range of light intensities. This PTAT powers all other circuit components. We use a relaxation oscillator to generate the clock frequency, and a series of D flip-flops to divide the clock frequency down from 20 kHz to about 1 kHz, the measurement frequency.

The 10 nA current is applied to electrodes with a timing controlled by a three-bit current multiplexer. This multiplexer consists of three switches as depicted in Fig. 4.2b. The current from the PTAT can either be diverted to one of the two electrodes, an on-chip reference capacitor, or a small 10 fF capacitor. Each component is shorted to the ground of the circuit when it is not the active component (i.e., the component to which the current is applied).

A timing diagram is shown in Fig. 4.2c. The multiplexer switches under two conditions: one, when the voltage on the active component reaches some threshold value, or two, when 100 ms has elapsed since the most recent switch. We utilize the 15 pF reference capacitor to ensure constant calibration of the ReMOTES. The electrode potential on the reference capacitor reaches the multiplexer switch condition after about 10 ms. The purpose of the 10 fF capacitor is to allow the other components to be shorted for a brief time in between measurements; the electrode potential on this capacitor reaches the switch condition after only 10 µs.

The potential on the active component is fed into a pulse generator to encode the voltage into timed pulses using pulse-position modulation (PPM). The PPM encoding scheme is depicted in Fig. 4.2d. The LED pulses in pairs; one of each pair occurs at a regular frequency given by the clock frequency. The second of each pair, the secondary peak, is time-shifted by a time related to the measured voltage. In between LED pulses, charge builds up on a 50 pF capacitor which is suddenly discharged on demand to pulse the LED. Under 2 kW/m^2 incident light intensity, the LED is driven with about 1 mA with a FWHM of about 80 ns.

The ReMOTES can measure voltage with a bandwidth of about 1 kHz and a noise floor of 50 µV RMS. They are optimized to operate under about 1 kW/m^2 incident light intensity or about 10 µW of power.

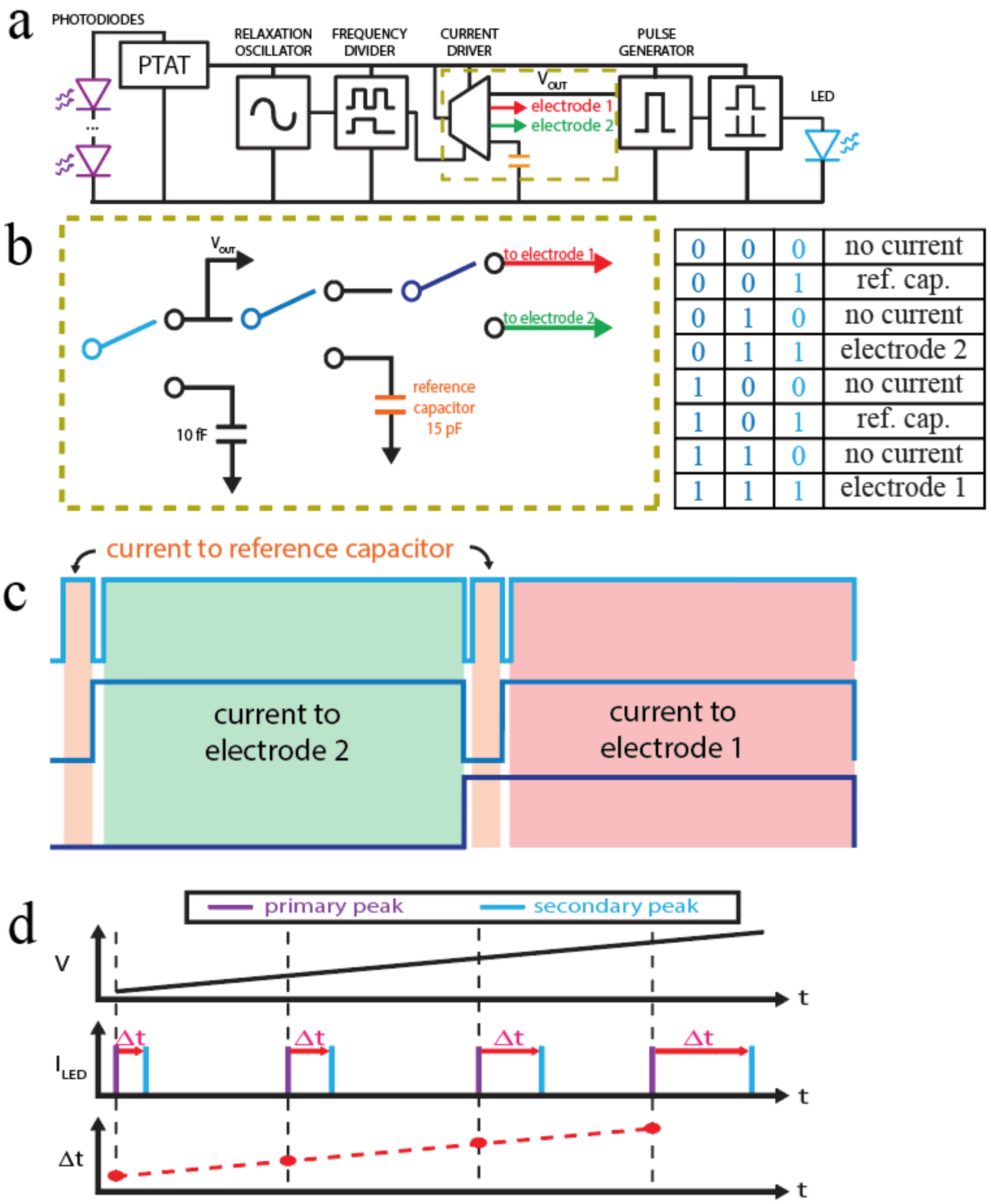

0	0	0	no current
0	0	1	ref. cap.
0	1	0	no current
0	1	1	electrode 2
1	0	0	no current
1	0	1	ref. cap.
1	1	0	no current
1	1	1	electrode 1

Figure 4.2: **ReMOTE Circuit and Timing Diagrams. a)** Circuit block diagram of ReMOTE. **b)** Depiction of the current multiplexer used to divert current toward the electrodes or the onboard reference capacitor. **c)** Timing diagram for current flow through the external electrodes and onboard reference capacitor. **d)** Scheme for encoding measured voltage into pulses of a micro-LED using pulse-position modulation.

4.3 On-Chip Characterization

To demonstrate initial functionality of the ReMOTES, we performed electrical measurements without releasing the devices from the substrate. After receiving the 200 mm diameter wafer from X-FAB as shown in Fig. 4.3a, the wafer is diced into 20 mm chips, each containing every circuit designed by various Cornell collaborations. One chip is shown in Fig. 4.3b. The ReMOTES, seen in Fig. 4.3c, are arranged in a grid.

For testing of the ReMOTE, wires were lithographically patterned connecting the four input/output terminals (two for the LED, two for the external electrodes) to macroscopic pads on the perimeter of this 20 mm chip. The wires were then insulated except for the pads for connection and the exposed electrodes on the device used for electrochemical measurements. This measurement scheme was designed to allow measurements in fluid without interference from the wires.

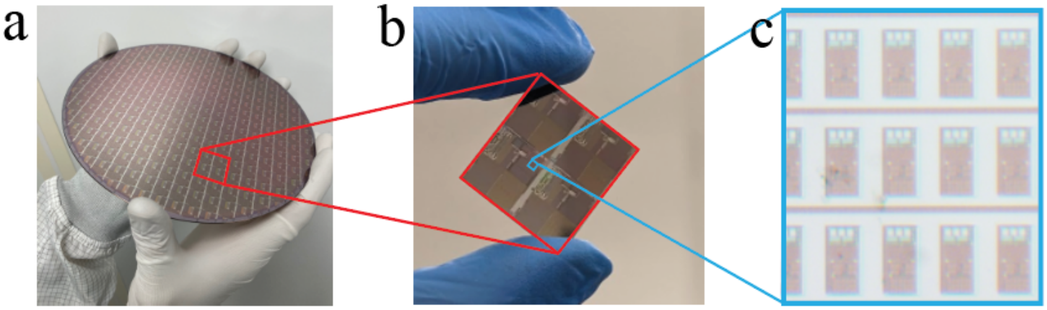

Figure 4.3: **Wafer received from X-FAB, a commercial foundry, containing ReMOTES. a)** SOI wafer as received from X-FAB. **b)** One 20mm chip diced from the wafer in **a)**. **c)** ReMOTE devices arranged in a grid on-chip as received from the foundry.

The ReMOTES were optically powered during this on-chip characterization.

In lieu of placing LEDs on the prototype devices, the output current was measured using a transimpedance amplifier.

To test the ReMOTES, we first connected the electrodes to physical capacitors. When a constant current is applied to a capacitor, the potential increases linearly at a rate inversely proportional to its capacitance, allowing the capacitance to be measured by the ReMOTE. Red (650 nm) light is shone on the sample with an intensity of about 2 kW/m^2 to power the ReMOTES, and the current was measured between the terminals designed to power a micro-LED.

Raw current data showing the pulse timing is shown in Fig. 4.4a. As expected, we see primary and secondary peaks in the current trace. The amplitude of the secondary peak is slightly diminished as the capacitors used to store charge for the LED do not have time to charge fully. These current spikes have smaller amplitudes and are longer than designed for a micro-LED due to the time constants inherent in using long wires to measure the ReMOTE on chip.

For this first generation of the ReMOTES, the time between peaks scales exponentially with the transmitted voltage, such that taking the logarithm of the peak spacing allows the voltage to be decoded. This decoded voltage is shown in Fig. 4.4b.

As shown, the measured voltage increases linearly with time, which is characteristic of a steady current being applied to a capacitor. A linear fit to these voltage data is shown in yellow in Fig. 4.4b. The slope dV/dt is inversely proportional to the measured capacitance and proportional to the applied current. In between the regions with a linear fit is the voltage measured across the reference capacitor, used to calibrate the voltage measured on the external capacitor.

On average, this potential rises 600 mV in about 1 ms. As a sanity check, given the reference capacitance this shows that the ReMOTE is producing about 10 nA as expected.

The ReMOTE-measured capacitance is compared to the physical capacitance in Fig. 4.4c. We note a fairly good agreement between the measured and expected values, especially at capacitances above 1 nF. The disagreement at low capacitance may be due to stray capacitances from the wires, which we expect to have a capacitance of roughly 500 pF based on their length.

Next, we tested the ability of the ReMOTES to perform salinity measurements. Varying concentrations of the salt NBu_4PF_6 were dissolved in acetonitrile and pipetted onto the device, and the device was measured using the same technique as for the dry measurement. The voltage again linearly increases with time, consistent with successful constant-current potentiometry in a salt solution without redox-active molecules.

Given the known current, the capacitance derived from dV/dt is plotted as a function of salt concentration in Fig. 4.4d. The measured capacitances increases with solution salinity. A 100x increase in salinity results in about a 50% increase in capacitance.

The capacitance-salinity relationship can be theoretically predicted by relating an electrode in fluid to a macroscopic capacitor. A standard capacitor with area A and thickness d has two oppositely charged plates and a total capacitance of $C \propto A/d$. Instead of two metal plates, an electrode in solution has charged particles on the metal surface, and oppositely charged particles in the solution near the electrode. The thickness d of this capacitor is called the Debye length, and is the thickness of the ionic layer that is needed to compensate for the charge on the electrode.

As the ionic concentration of the fluid increases, the ion layer thickness d needed to screen the charge of the electrode decreases, increasing the capacitance C of this double layer. From this model, we would expect the capacitance to scale with the square root of salinity; we do not see the expected factor of 10 increase in capacitance for a 100x increase in salinity. However, this is a very simplified model, and other literature sees a diminished scaling of capacitance with salinity as well[54]. The salinity-capacitance relationship measured by the ReMOTES, then, is consistent with the literature and we assert that these ReMOTES are truly measuring the electrochemical dynamics in fluid.

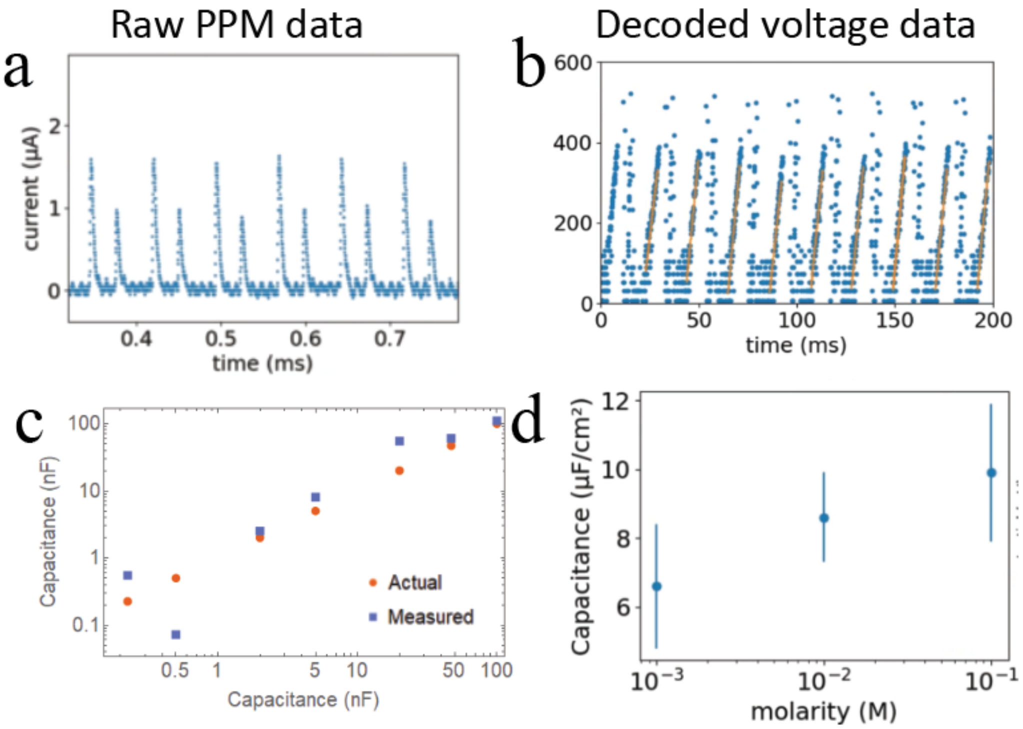

Figure 4.4: **Preliminary Results from the ReMOTE Circuit. a)** A raw current trace showing the PPM pulses. **b)** Voltage data after decoding raw PPM data. **c)** Comparison of ReMOTE-measured capacitance to the capacitance of macroscopic, physical capacitors. **d)** Electric double-layer capacitance of Pt electrode in fluid as a function of salinity, as measured by the ReMOTE prototype on chip.

4.4 Outlook

Here, we have demonstrated the first steps toward an optically powered microscopic electrochemical sensor. We discussed their measurement scheme and the operation of the onboard CMOS circuitry. Further, we characterized the first generation ReMOTES on chip and demonstrated their ability to detect changes in salinity.

The next generation of ReMOTES has been designed, manufactured at X-FAB, and awaits on-chip characterization and further processing. These ReMOTES contain many of the same components as the first generation.

Unlike the first generation of ReMOTES, these new devices are designed to power a vertical-cavity surface-emitting laser (VCSEL), but can also power an LED as previously described. The light from a VCSEL is emitted primarily in one direction, compared to a micro-LED that emits in all directions; this allows a much brighter signal from the ReMOTES and easier data transmission.

Generation two ReMOTES are also designed to measure redox molecule concentrations in addition to salinity. These devices will be able to measure voltages of up to 2V, allowing measurement of a wide range of redox molecules, including water.

To optimize the ReMOTES for electrochemical sensing, there are multiple verions of generation two devices. These ReMOTES have differnt applied currents, reference capacitors, and PPM resolutions. In post-processing, these devices can also utilize different electrode areas to study the effect of these parameters on measurement resolution.

Here we have shown the first steps toward a microscopic optically powered electrochemical sensor. We have shown the on-chip capability of these devices to measure a change in solution salinity, and will use the same technology to measure concentrations of redox molecules in the future. These devices, when released from the substrate, will measure 400 x 100 x 15 μm^3, or about a volume of 1 nL.

We envision a variety of non-invasive measurements enabled by this technology, but as a starting point we aim to monitor in real-time the concentration of redox molecules during reactions in well plates, as described previously in Chapter 2. Moreover, the development of a microscopic electrochemical sensor is a crucial step toward nanoliter electronics for wireless chemistry.

CHAPTER 5

ELECTROCHEMICAL LOCOMOTION FOR MICROSCOPIC ROBOTICS

So far, we have demonstrated electrochemistry as a mechanism by which microscopic electronic devices can perform chemical synthesis and sensing in small fluid volumes. For the remainder of this thesis, we discuss electrochemistry as a propulsion mechanism for microscopic robotics. Specifically, in this chapter we consider previous work in our group to develop electrochemically driven actuators that are fully integrable with silicon electronics.

Microscopic robots have been developed recently that are capable of performing a variety of complex tasks such as drug delivery[55], cargo towing[35], and environmental remediation[56]. These ”microbots” have used a range of propulsion mechanisms including ultrasound[57], electrophoresis[58], bubbles[35], magnets[59], artificial legs[13], and biohybrid propulsion[60]. Despite the versatility of propulsion mechanisms, very few are electronic in nature. Most methods of propulsion, then, are not integrable with onboard electronics for control, so there is very little existing work in this microscopic realm.

5.1 Surface Electrochemical Actuators

To this end, our group has recently spearheaded the development of electrochemically driven actuators that are fully integrable with silicon electronics. These surface electrochemical actuators (SEAs) are controlled by applying a potential to the actuator with respect to the surrounding fluid. A schematic of a typical SEAs experiment is shown in Fig. 5.1a. A microprobe is used to apply a potential to the actuators with respect to an Ag/AgCl reference electrode in the electrolyte solution.

The SEAs are bimorph structures as shown in the cross-section in Fig. 5.1b. The electrochemically active material, a 7 nm thick layer of platinum, is capped by an electrochemically inert material, titanium in this case. We note that the entire stack is only about 10 nm thick. The ultrathin nature of the SEAs is crucial to decreasing their bending stiffness in order to maximize the response of their curvature to an applied potential.

A depiction of the mechanism for the SEAs is shown in Fig. 5.1c. Ions in an electrolyte solution adsorb/desorb from a platinum surface in response to an applied potential between the platinum and the electrolyte. This ion adsorption changes the surface stress of the platinum. If one side of the platinum is capped with a nonreactive layer (e.g., titanium), the bimorph stack will bend in response to the unequal stress.

A demonstration of a SEA bending in response to an applied potential is shown in Fig. 5.1d. The adsorbed ion species depends on the applied potential; the SEA shown here is demonstrating the adsorption of an oxygen species. These actuators curl more with higher positive potentials. Fig. 5.1e shows a plot of measured actuator curvature as a function of applied potential, demonstrating successful actuation at voltages less than 500 mV.

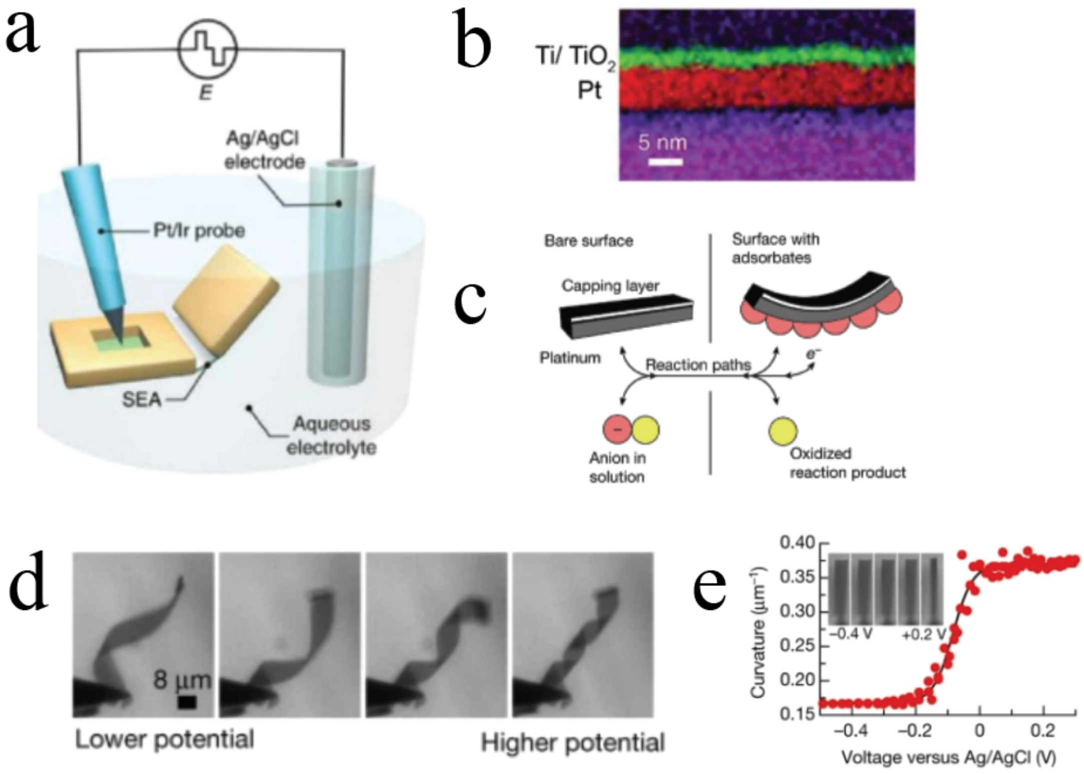

Figure 5.1: **Mechanism and Demonstration of Surface Electrochemical Actuators (SEAs).** **a)** Diagram of measurement setup for SEA characterization. Image by Michael Reynolds. **b)** Cross-sectional TEM image of a titanium-platinum bimorph stack. Image adapted from [13]. **c)** Schematic showing electrochemically driven adsorption resulting in curvature of a SEA. Image adapted from [14]. **d)** Micrographs showing SEAs curvature with different applied potentials. Image adapted from [14]. **e)** Measured SEA curvature as a function of applied potential. Image adapted from [14].

These actuators are fabricated and released in parallel from the substrate using planar lithography, entirely compatible with the manufacturing of electronics. In fact, Miskin *et al.* demonstrated the use of these SEAs with silicon photovoltaics to make a rudimentary walking robot[14]. Liu *et al.* has also demonstrated similar actuators utilizing film oxidation instead of surface adsorption resulting in a shape-memory effect[61].

5.2 Microscopic Robots with Electrochemical Actuator Legs

The true potential of this technology was realized when our group successfully integrated these electrochemically driven actuators with CMOS circuitry for advanced control. This team includes myself and was led by Michael Reynolds. These microbots are optically powered and locomote autonomously under incident light. The circuits for these microscopic robots were designed in Cadence *Virtuoso* and manufactured at a commercial foundry (X-FAB), and the SEA legs were fabricated in post-processing at the Cornell Nanoscale Facility.

These robots measure about 100 µm in size, and are shown next to an ant in Fig. 5.2a. An optical micrograph of a device in Fig. 5.2b shows the onboard photodiodes, integrated circuit, and legs. The SEAs are seen in Fig. 5.2c with rigid SiO_2 panels to define the leg hinge and support the device when walking.

The integrated circuit produces a series of phase-shifted square waves to drive the legs of the device. The layout for the circuit is shown in Fig. 5.2d. Similar to the ReMOTES, the circuit contains photodiodes for power, an onboard relaxation oscillator, a PTAT current source, and frequency dividers. Fig. 5.2e shows an optical micrograph of the circuit after production by X-FAB. The exact details of the circuit depend on the desired functionality and gait for each microbot. Because of the versatility of CMOS circuit design, robots with multiple gaits were manufactured in parallel.

Perhaps the most significant innovation of this work is the post-processing of these circuits to enable their release from the substrate. The robots must be thin enough to be supported by their ultrathin SEA legs, and therefore must be separated from the handle wafer on which they are fabricated. Thirteen layers of lithography are required to pattern the SEA legs and release the devices from the substrate. An optical micrograph of released devices are shown in Fig. 5.2f.

After release, these devices are simply powered by incident light at about an intensity of 1 kW/m^2, about that of a sunny day. The onboard circuit drives the electrochemical actuator legs, enabling the robots to crawl across a solid-liquid interface as shown in Fig. 5.2g. These robots are also capable of receiving optical commands to control their speed and direction[13].

5.3 Outlook for Electrochemical Actuators

We have now shown the first autonomous microscopic robots. These microbots use onboard CMOS circuitry to drive electrochemical actuators to locomote across a solid-liquid interface. This technology demonstrates not only the utility of electrochemical propulsion methods, but the feasibility of their integration with electronics, paving the way for microbots that can interact with their environment and perform complex functions. In addition to microscopic robotics, these actuators have been used in other applications as well, such as artificial cilia for fluid pumping[62].

In this chapter, we demonstrated the use of electrochemically driven actuators to enable locomotion at the microscale. In the next chapters, we adapt a known technique for electrochemical bubble propulsion to develop the first electronically integrated bubble-propelled microswimmer.

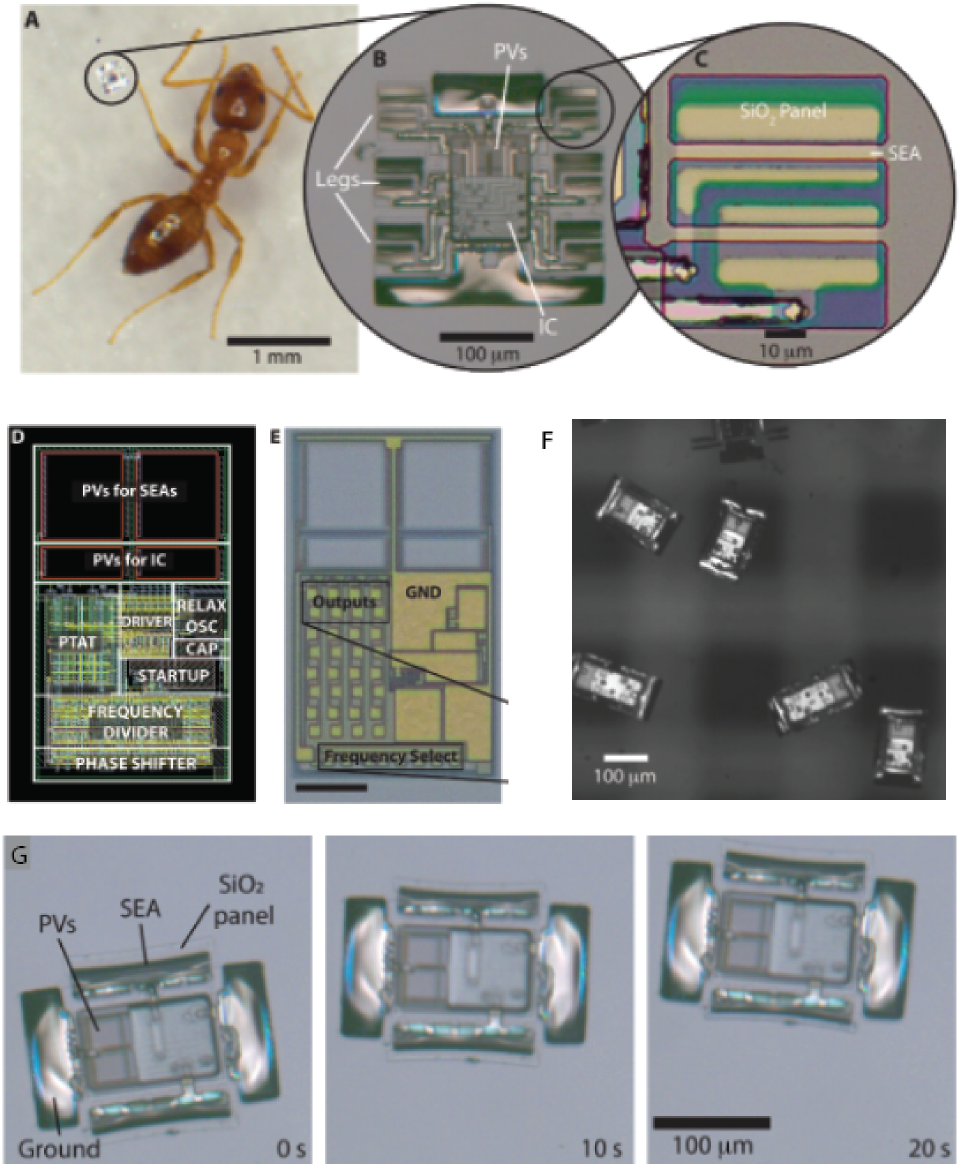

Figure 5.2: **Microscopic Robots with Onboard Digital Control and SEAs. Figure adapted from [13] a)** Microscopic robot next to an ant for scale. **b)** A micrograph of a robot showing onboard photodiodes and integrated circuit. **c)** SEAs and SiO_2 panels for rigidity in select locations. **d)** Physical layout for the microscopic robot circuit. **e)** Optical micrograph of the control circuit for the robots. Scale bar 20 µm. **f)** Multiple microscopic robots released from their substrate. **g)** Time lapse of microscopic robot locomoting on a solid-liquid interface.

CHAPTER 6

A REVIEW OF BUBBLE-PROPELLED MICROSWIMMERS

In the previous chapter, we discussed electrochemical actuators and demonstrated their integration with silicon electronics to make the first autonomous microscopic robots. There is yet another propulsion technique that utilizes electrochemical reactions: bubble propulsion. Bubbles are the most common electrochemical propulsion technique in the literature[63, 64, 65, 35, 15, 66, 67]. Bubble-propelled microswimmers have been developed at size scales ranging from less than a micron[68] to over a millimeter[69], spanning the entire size range of microscopic robotics.

The remainder of this thesis will be devoted to considering this type of microswimmer. Here, we discuss the physics behind bubble propulsion as well as existing work on bubble-propelled microswimmers. In the next chapter, we will use this propulsion technique to develop the first bubble-propelled microswimmer with onboard silicon electronics.

6.1 Working Principle for Bubble Rockets

Bubble rockets utilize electrochemical reactions that evolve gas as a reaction product. Once the local concentration of gas in solution reaches a critical threshold called supersaturation, a bubble is nucleated. These bubbles can grow, move, and detach from the bubble-producing device. If bubbles detach from a microswimmer in one direction, the swimmer will move in the opposite direction.

To demonstrate functionality of bubble-propelled microswimmers, we'll discuss a typical example from the literature, shown in Fig. 6.1a. This device is a rolled, tapered metallic tube that operates in hydrogen peroxide. Here, the platinum in the tube catalyzes the decomposition of hydrogen peroxide:

$$2H_2O_2 \rightarrow O_2 + 2H_2O \tag{6.1}$$

The produced oxygen gas nucleates into bubbles if produced at a fast enough rate. These bubbles rapidly grow inside the tube and are subject to a capillary force due to the different radii of curvature of the two bubble ends in the tapered tube[66]. As a result, the bubble is ejected from the larger end of the tube.

It's important to note that the term "bubble rocket" here is misleading - in fact, microswimmers do not utilize inertial forces from mass ejection for propulsion. The sum of forces on the microswimmer is $\sum F = ma$, but at low Reynolds number a force from mass ejection induces a viscous force that almost exactly balances it such that $\sum F = 0$.

Multiple models have been proposed for the exact mechanism of bubble propulsion[70], and we here discuss the most commonly accepted mechanism found by equating the Stokes forces of the ejected bubble and microswimmer over a time τ in which the swimmer and bubble are separated. In this time, the bubble and swimmer of Stokes radii r_B and r_S respectively move distances d_B and d_S. In this model, the microswimmer moves forward gradually while the bubble separates from the tube. A diagram of this process is shown in Fig. 6.1b. Equating the Stokes forces between the microswimmer and the bubble, we find

$$6\pi\eta r_B d_B/\tau = 6\pi\eta r_S d_S/\tau \tag{6.2}$$

Importantly, the only geometry-dependent term here is the Stokes radius. By definition, during ejection the bubble moves its diameter with respect to the swimmer, such that $d_B + d_S = 2r_B$. The microswimmer velocity is simply $v_s = d_s f$ where f is the bubble ejection frequency. Thus, the theoretical velocity of a bubble-propelled microswimmer is

$$v_s = 2\frac{r_B^2}{r_S + r_B} f. \tag{6.3}$$

This model is simplified and neglects other forces such bubble motion in the tube, bubble growth forces, and the interaction of the microswimmer with other objects or boundaries. However, this model allows us to roughly estimate the velocity of a bubble-propelled microswimmer and predict its dependence on geometric parameters. In Fig. 6.1c the velocity vs. tube length is shown for a bubble rocket operating in peroxide. At some rocket length, bubbles begin to be ejected out of both ends, causing the velocity to drop to zero. At lower lengths, the actual microjet velocity is roughly consistent with the theoretical velocity given by this model[16]. Although a tube-like geometry is shown here, bubble-propelled microswimmers can be any geometry, as long as the bubbles are ejected from the device non-isotropically.

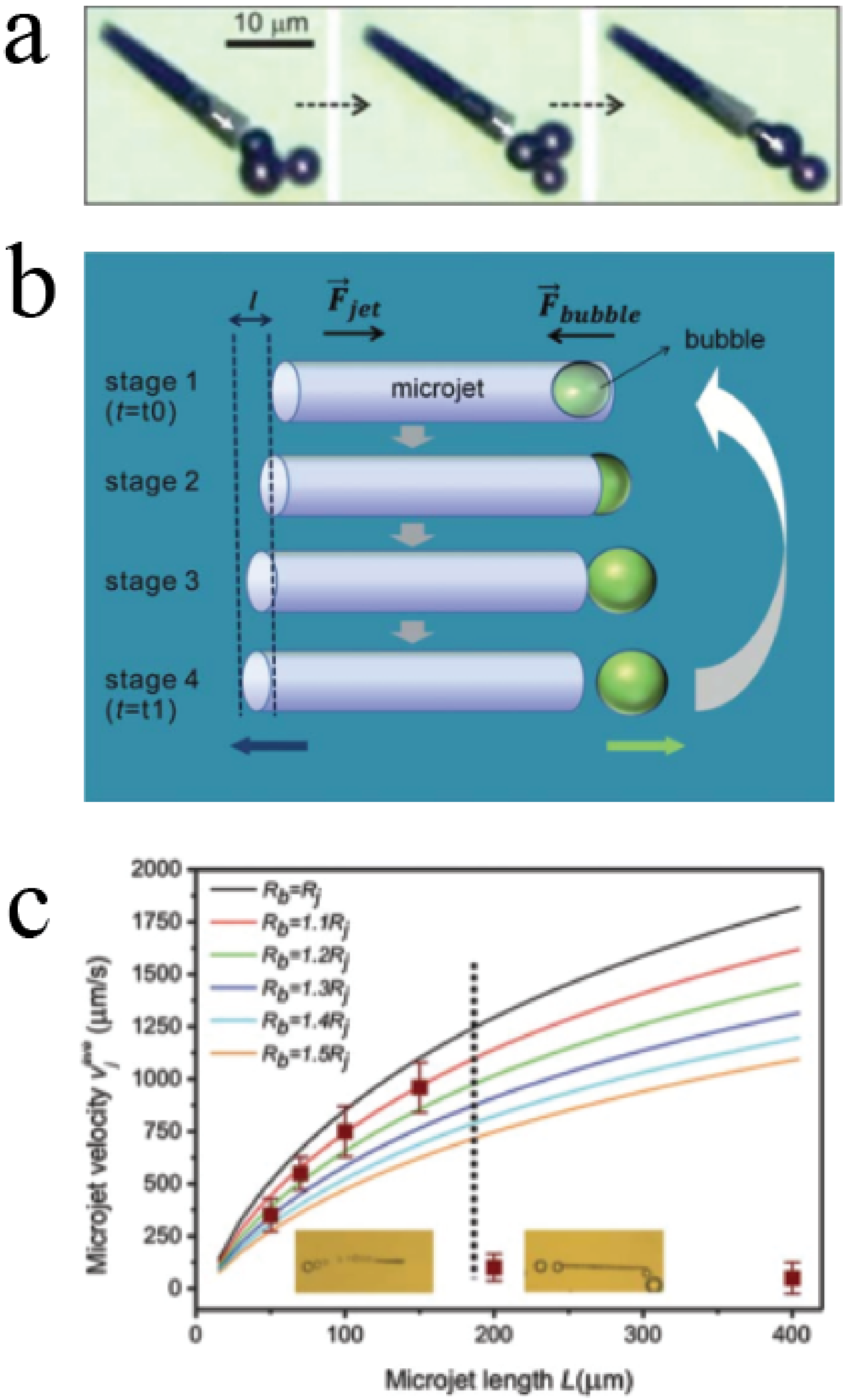

Figure 6.1: **Introduction to Bubble Propelled Microjets. a)** Micrograph of Pt microtubes that produce and eject bubbles by reacting with H_2O_2. Image adapted from [15]. **b)** Diagram showing propulsion mechanism for bubble rockets. Image adapted from [16]. **c)** Bubble rocket velocity vs. tube length. Figure adapted from [16].

6.2 Chemical Fuels for Bubble Generation

The vast majority of bubble-propelled microswimmers fall into at least one of two categories: those that are fueled by a chemical in their environment, and those that contain a consumable fuel onboard the device.

In the first category, we find bubble-propelled microswimmers that are fueled by hydrogen peroxide[16, 15, 67] and strong acids[55, 71], specifically gastric acid. In fact, the operation of Zn micromotors was shown *in vivo* recently in a mouse's stomach for drug delivery[17]. An image of these micromotors operating in gastric acid is shown in Fig. 6.2a.

In the second category, we find microswimmers that operate in a wider range of solutions by using an onboard fuel. These gas-evolving reactions often proceed spontaneously at metals in solution even without an applied voltage. As a common example, alkali metals (lithium, potassium, magnesium, etc.), react spontaneously with water to produce hydrogen gas. A magnesium micromotor operating in phosphate buffered saline (PBS) is shown in Fig. 6.2b. Similar micromotors can operate in pure water[18]. These devices that utilize an onboard fuel have very limited lifetimes (minutes) as the onboard metal fuel is consumed during the reaction.

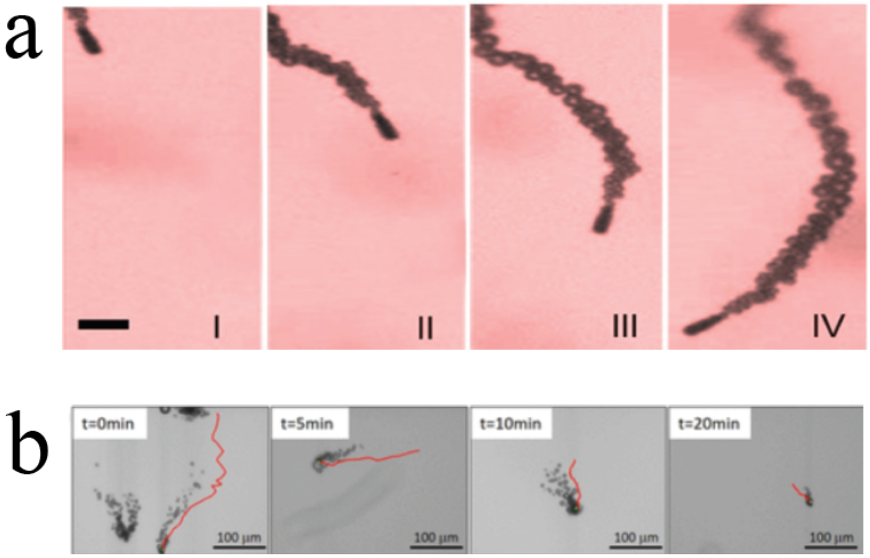

Figure 6.2: **Bubble-propelled Microswimmers Utilizing Chemical Fuels for Locomotion. a)** Micrograph of Zn bubble rockets operating in gastric acid at physiological temperature. Scale bar 20 µm. Image adapted from [17]. **b)** Time lapse of Mg bubble rockets operating in phosphate-buffered saline. Image adapted from [18].

6.3 Steering and Control

The bubble rockets discussed thus far have all utilized reactions that proceed spontaneously, but by definition microscopic robots require some level of control. The most rudimentary form of control is on/off behavior. To this end, Fig. 6.3a shows $TiO_2 - CaCO_3/PEGDA$-based microswimmers that utilize photocatalytic hydrogen peroxide breakdown. This reaction only proceeds under incident UV light, allowing the microswimmer velocity to be turned on and off depending on the illuminating light intensity.

Many of the microswimmers discussed thus far are easily integrated with various mechanisms for steering. For instance, many bubble rockets are integrated with ferromagnetic materials to enable steering in a magnetic field. One example of this is shown in Fig. 6.3b, where a bubble-propelled micromotor steered with a magnet is used to pick up cargo. The micromotor adheres to the cargo due to surface forces, and releases the cargo when forced to rapidly change directions due to a change in the magnetic field[20]. Non-ejected bubbles can also be controlled with an acoustic field, enabling more advanced steering as well[72]. The use of onboard CMOS to control bubble propulsion has also been demonstrated, but these devices exceed 1 mm in size, and are therefore not suited for this discussion of microscopic swimmers[69].

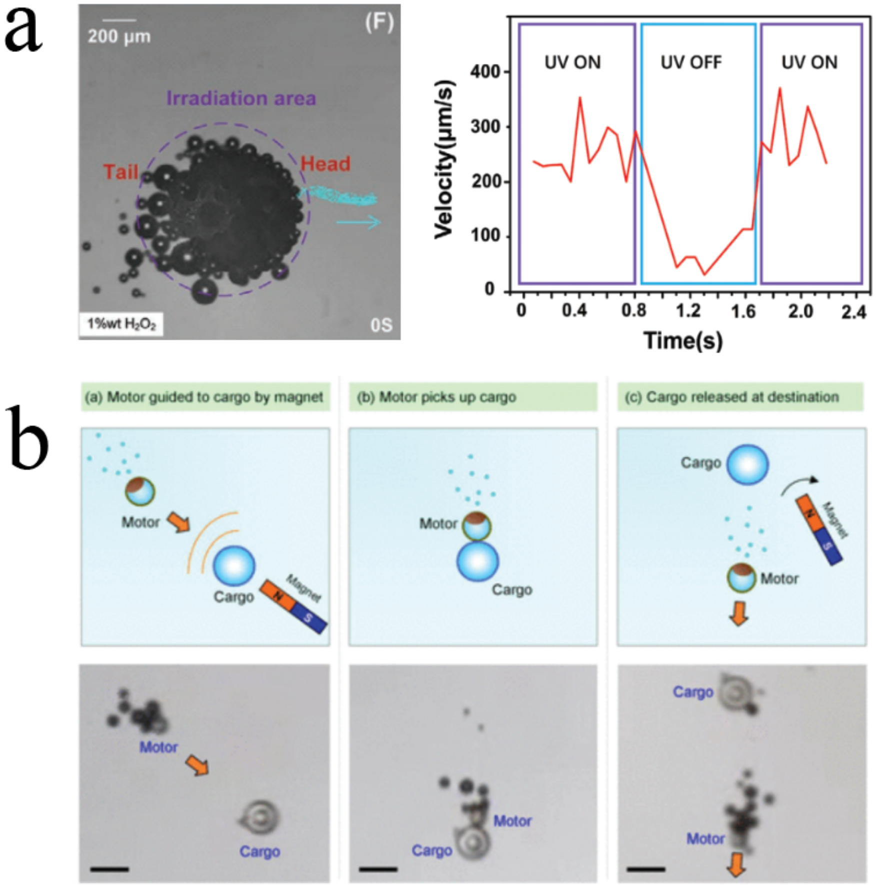

Figure 6.3: **Bubble-propelled Microswimmers Demonstrating Advanced Control. a)** Image of photocatalytic micromotor in UV-illuminated area (left) and velocity vs. time with light on and off (right). Image adapted from [19]. **b)** Bubble-propelled micromotor manipulating cargo while being steered with a magnetic field. Image adapted from [20].

6.4 Outlook for Bubble Propulsion

Compared to electrochemical actuator locomotion, bubble propulsion has some specific advantages. The velocities of many of the bubble-propelled microswimmers discussed here are extraordinarily high – in some cases, more than 100 body lengths/second, on par with some of nature's most efficient locomoting microorganisms. Moreover, there is a vast range of chemical fuels, device materials, and microswimmer shapes for which bubble propulsion is achievable. All of the silicon devices shown here sink in fluid due to silicon being denser than water, but unlike the SEAs robots, bubble-propelled swimmers can leverage produced bubbles to control their buoyancy. In general, the motivation for pursuing both the SEAs and the bubble rockets is simply that the preferred locomotion mechanism for microscopic robots is application-dependent, and we simply seek to expand our toolbox of locomotion mechanisms for microscopic robotics.

Despite the enormous field of microscopic bubble rockets, none have yet been integrated with silicon electronics or advanced nanofabrication strategies to enable their advanced control. However, in Chapter 2 we already demonstrated the ability of optically powered microscopic devices to drive electrochemical reactions at onboard electrodes. We now turn to a similar technology to drive electrolytic bubble production for propulsion.

CHAPTER 7

OPTICALLY POWERED MICROSCOPIC BUBBLE ROCKETS

In the previous chapter, we discussed the wide range of existing work on bubble-propelled microswimmers. Here, we adapt these known techniques for bubble propulsion with silicon electronics to develop an optically powered microswimmer that can operate in any aqueous solution.

We begin by discussing how these microswimmers are manufactured, and then demonstrate swimming behavior in a saline solution. We then show how the swimming trajectory of these microbots depends on their design and demonstrate dynamic steering. We reveal a novel method for bubble propulsion on solid-liquid interfaces, and conclude with a discussion of integration of these microswimmers with CMOS circuits for more advanced control.

7.1 Fabricating and Manipulating Bubble Rockets

We begin with a discussion of how these microswimmers are fabricated and manipulated. Importantly, they are manufactured using planar lithography, allowing them to be fabricated and released from the substrate in parallel.

We start fabrication with a p-type (B) silicon-on-insulator (SOI) wafer from Ultrasil Corp. with a 2 μm device thickness and a 500 nm bottom oxide (BOX) layer thickness. We dope the top of the device layer by spinning 8% phosphosilicate glass (PSG) on the wafer before a high-temperature (1050 °C) rapid thermal anneal and subsequent removal of the PSG in 6:1 BOE. Using contact lithography, we pattern and etch the device Si to the p-type region using an HBr plasma, and then repeat to etch to the bottom oxide to separate the diodes. At this stage, the rockets are also defined in silicon. We deposit a 50 nm conformal SiO2 using ALD which we then pattern and etch in 6:1 BOE before performing a lift-off process to sputter 2/80 nm Ti-Pt contacts to the n- and p-type regions. We then repeat this lift-off procedure to pattern the interconnects to wire up the diodes and to define the electrodes on top of the silicon rocket shape, followed by a CHF3/O2 etch to the Si handle around the device to define its shape.

At this point, if desired, we perform a lift-off process and deposit 50 nm Co via e-beam evaporation for the thin-film magnets. We deposit 100 nm PECVD SiO2 followed by 600 nm PECVD tetraethyl orthosilicate (TEOS) to encapsulate the device, again etching with CHF3/O2. Al is sputtered onto the device, patterned, and etched in MIF 726 to define strips of material to connect the devices to the surrounding SiO2. The devices are then undercut with a XeF2 vapor etch, which also etches the Si defining the rockets resulting in a hollow rocket shape. The devices are then submerged in 0.2% tetramethylammonium hydroxide (TMAH) to etch the aluminum and release the devices from the substrate. After release from the substrate, the TMAH used to release the devices was diluted 1000x by the desired solution, often 1-10 mM PBS.

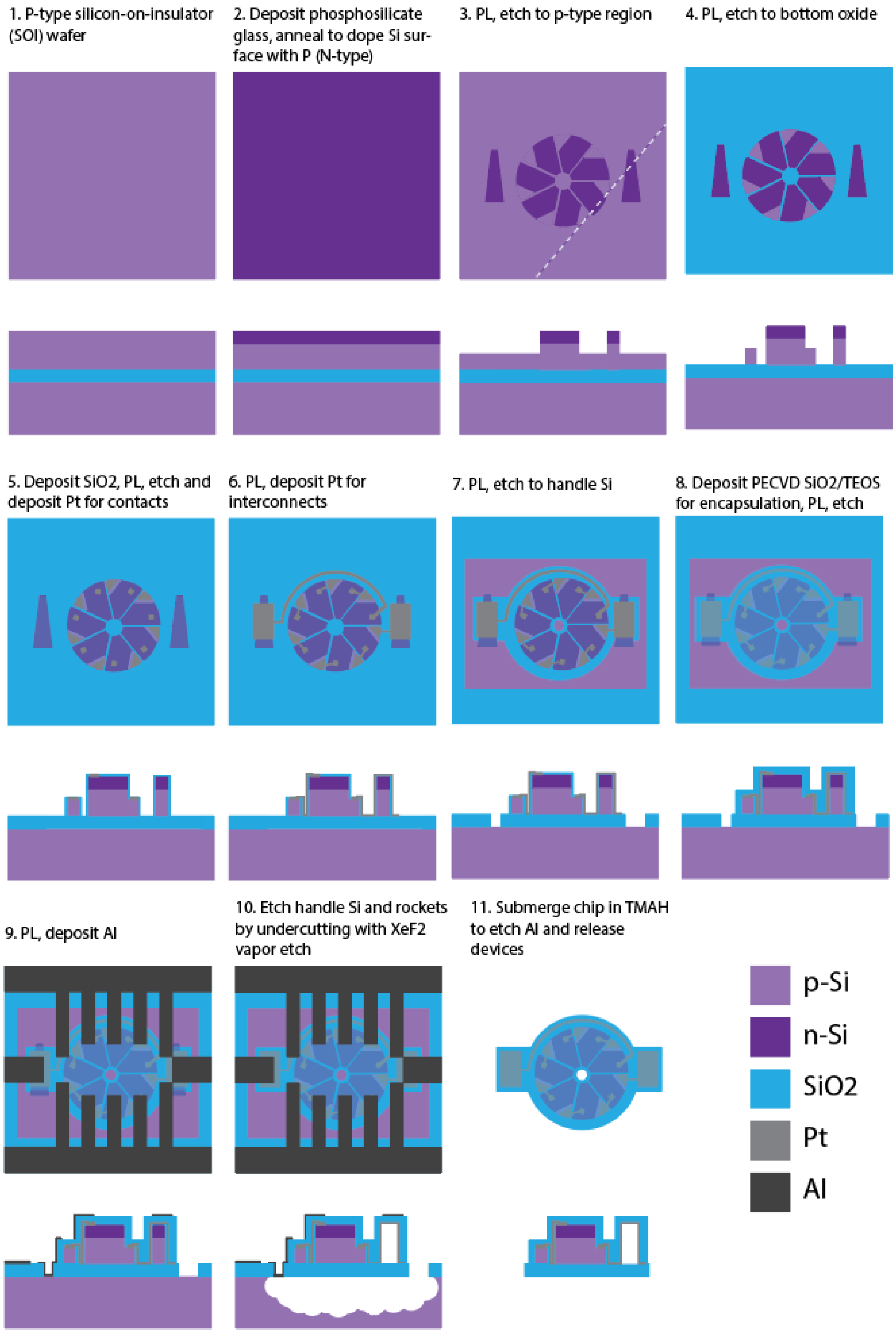

Figure 7.1: **Process Flow for Manufacturing Optically Powered Microscopic Bubble Rockets.** Top-down and cross-section views of bubble rockets during fabrication.

A microscope image showing multiple bubble rockets on chip during fabrication is shown in Fig. 7.2a. After release from the substrate, these bubble rockets are manipulated in bulk with micropipettes, or individually with a pulled glass pipettes attached to a micromanipulator and syringe pump. A micrograph showing the latter is shown in Fig. 7.2b.

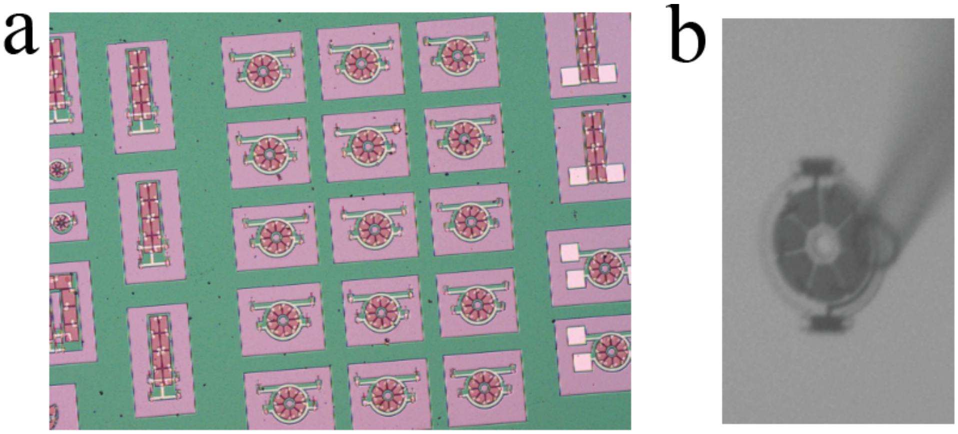

Figure 7.2: **Bubble Rocket Fabrication and Manipulation.** **a)** On-chip micrograph showing parallel fabrication of bubble rockets. **b)** A bubble rocket being manipulated with a micropipette.

7.2 Operation of Microswimmer

Although their fabrication is complex, the components of these bubble rockets can be understood quite simply. A diagram of a microswimmer is shown in Fig. 7.3a. Each device consists of multiple silicon photodiodes wired in series with a hollow tapered electrode. The entire device is encapsulated in silicon dioxide except for the interior of the hollow electrodes. Under incident light, the onboard photodiodes apply a voltage between the two electrodes sufficiently high to drive water electrolysis, splitting water into hydrogen and oxygen gas:

$$2H_2O \rightarrow 2H_2 + O_2. \tag{7.1}$$

The water electrolysis reaction at the cathode produces hydrogen gas:

$$2H_2O + 2e^- \rightarrow H_2 + 2OH^- \tag{7.2}$$

At the anode, oxygen gas is produced:

$$2H_2O \rightarrow O_2 + 4H^+ + 4e^- \tag{7.3}$$

Just as in our previous discussion of bubble-propelled swimmers, this evolved gas rapidly nucleates into bubbles. The capillary force on these bubbles in the tapered cylinder forces them to be ejected from the tube, propelling the microswimmer forward.

A time lapse for a microswimmer locomoting on an air-water interface is shown in Fig. 7.3b. This device is illuminated by roughly 20 kW/m^2 Hg lamp illumination in 10 mM PBS solution, and is swimming at the air-liquid interface in a petri dish. As shown in the distance vs. time curve in Fig. 7.3c, the instantaneous velocity of this microswimmer is 30 ± 5 µm/s throughout its swimming trajectory.

In the previous chapter, we discussed the most prevalent model for bubble propulsion, resulting in a theoretical swimmer velocity dependent on swimmer and bubble radius given in eq. 6.3. Now, we consider this microswimmer in that same framework. In Fig. 7.3b, the bubbles ejected have a mean radius of about 2 µm and have an ejection frequency of roughly 120 Hz. The Stokes radius of this flat-ish disk is 34 µm, and therefore this device has a theoretical velocity given by eq. 6.3 of roughly 30 µm/s. This theoretical velocity lines up well with the experimental value.

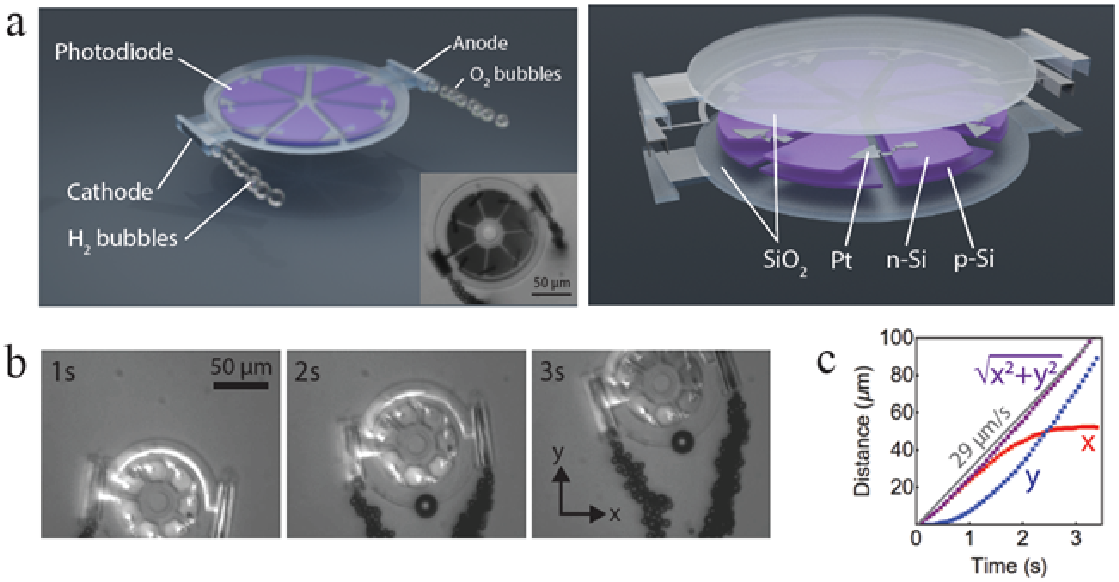

Figure 7.3: **Microswimmer Locomoting via Water Electrolysis. a)** Diagrams of optically powered microswimmer showing encapsulated photodiodes, hollow platinum electrodes, and bubble production. Inset: microswimmer operating on glass-water interface in 10 mM PBS solution under Hg lamp illumination. **b)** Time lapse of a device swimming under mercury lamp illumination at an air-water interface in 10 mM PBS solution. **c)** Displacement vs. time for the swimming device shown in b.

In Fig. 7.3b, we can see that this device does not swim in a straight line, but has a curved trajectory. For this device, the hydrogen-producing cathode is on the right, with the oxygen-producing anode on the left. The two electrodes are equidistant from the microswimmer center of mass. The net torque on this device, then, is due to the 2:1 ratio of produced H_2 to O_2 (see eq. 7.1).

7.3 More Microswimmer Examples and Designs

We have now demonstrated optically powered bubble-propelled microswimmers swimming on a liquid-air interface. Surface tension alone is enough to hold them at liquid-air or liquid-liquid interfaces. However, these microswimmers are primarily made of silicon and glass, and therefore sink in the fluid bulk. As a result, most of our bubble rocket data is taken on the solid-liquid interface.

Shown in Fig. 7.4a are four bubble rockets operating on a solid-liquid interface in 1 mM PBS solution. The surface under these swimmers is SiO_2, and these devices are all functioning under mercury lamp illumination. The measured velocity of their centers of mass are shown in the table, as well as their theoretical velocity predicted by eq. 6.3.

It is clear from Fig. 7.4a that the predicted velocities are about 2-3x higher than what is measured. In contrast, the predicted velocity agreed well with experimental values for microswimmers on an air-liquid interface. We propose that this disagreement at solid-liquid interfaces may be due to interactions between microswimmers and a nearby solid surface. Specifically, a fluid boundary layer with a no-slip condition at both the solid surface and the microswimmer may cause a friction-like force on the swimmer. In other words, the fluid at the surface of the microswimmer must move with the velocity of the microswimmer, and the fluid at the solid surface must be at rest. The shear force between these two fluid layers is limited by the finite fluid viscosity, slowing down the microswimmer.

Now that we've discussed the variety of interfaces at which these devices can operate, we now turn to the versatility of their design. These microswimmers are all fabricated lithographically, allowing their geometry to be easily changed. In Fig. 7.4b, we show a broad range of device designs that have been manufactured and released from the substrate.

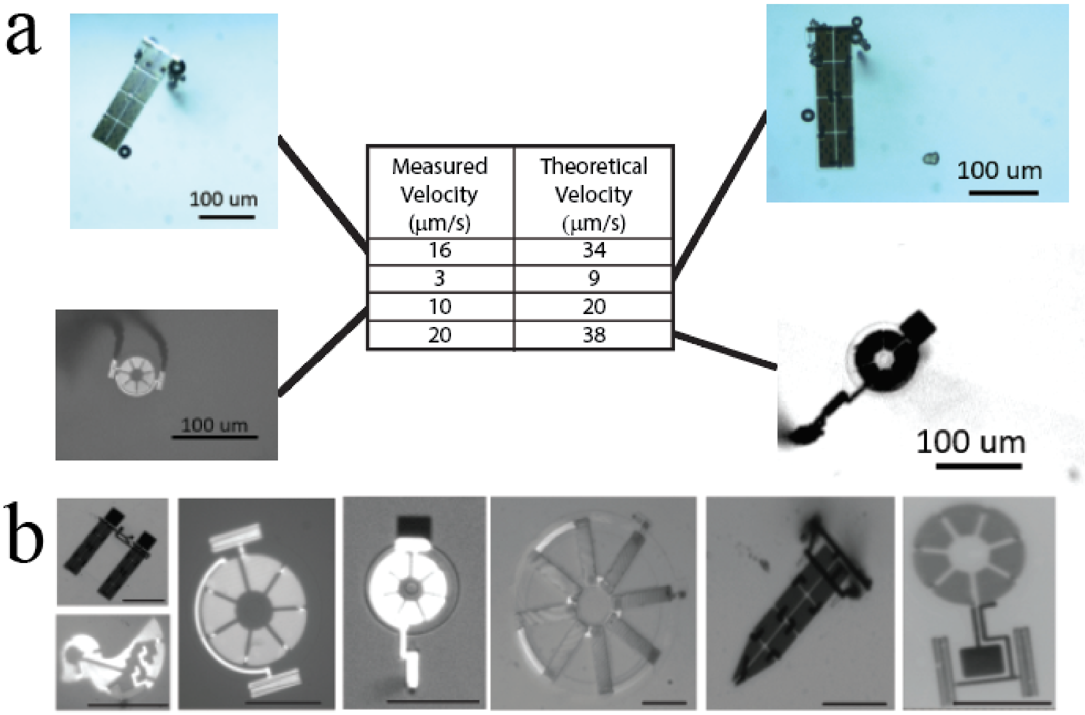

Measured Velocity (µm/s)	Theoretical Velocity (µm/s)
16	34
3	9
10	20
20	38

Figure 7.4: **More Bubble Rocket Swimming Behavior and Designs. a)** Table comparing measured device velocity to theoretical values from eq. 6.3 for microswimmers on a solid-liquid interface. **b)** A variety of bubble rocket designs fabricated using the same approach. These devices are released from the substrate. Scale bar 100 µm.

7.4 Effect of Light Intensity on Microswimmer Behavior

We now turn to a discussion of how light intensity and salinity affect microswimmer behavior. To study these effects, we measured the bubble ejection frequency of a stationary microswimmer on a solid-liquid interface under different Hg lamp intensities and in different PBS concentrations. The results are shown in Fig. 7.5a. The bubble ejection frequency increased with salinity, and with light intensity until saturating at around 6 $\mathrm{kW/m^2}$.

To understand these results, we consider separately the I-V characteristics of the onboard silicon photodiodes and the rocket electrodes. These I-V measurements are shown in Fig. 7.5b. For the photodiodes, a potential was applied between anode and cathode of an 8-PV stack. For the electrodes, on-chip rockets were fabricated using the same process flow as for the microswimmers, and potentials were applied to the electrodes with respect to a Pt reference electrode in the electrolyte. In both cases, the potential was swept and the resulting current measured using a transimpedance amplifier. The photodiode current is proportional to light intensity, so these I-V curves are extrapolated to higher light intensities.

The operating point for the photodiode-electrode system is the intersection of these I-V curves, denoted as circles in Fig. 7.5b. As light intensity increases, the effect of illumination on the operating current is diminished as the photodiodes become voltage-limited. The frequency of bubble ejection is proportional to the gas production rate and therefore current. This saturation of bubble frequency with illumination intensity is then due to the voltage-limited behavior of the photodiodes at high light intensities.

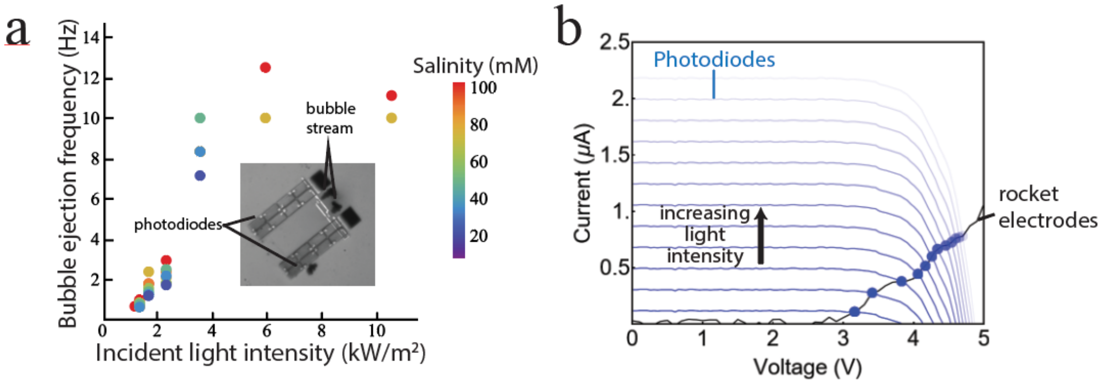

Figure 7.5: **Effect of Illumination Intensity on Microswimmer Behavior and Electrical Characteristics of Photodiode/Rocket System.** **a)** Bubble ejection frequency as a function of incident light intensity for a stationary microswimmer. **b)** I-V characteristics for photodiodes and on-chip rocket electrodes, with the operating points shown as circles.

7.5 Dynamic Steering and Trajectory Control

Next, we demonstrate the dependence of swimming trajectory on device geometry. Specifically, a microswimmer with a bubble propulsive force symmetric about its center of mass will move in a straight line, where any other design will result in a circular trajectory under a uniform light field. We can design our microswimmers to have any electrode geometry and placement, allowing the production of O_2 bubbles, H_2 bubbles, neither or both in order to achieve different swimming trajectories.

One example of a bubble rocket geometry that results in a linear trajectory is shown in Fig. 7.6a. This device has its cathode connected in parallel to two bubble rockets that are symmetric about the axis along which the device locomotes. The anode is connected to a planar electrode that does not produce bubbles. A device that swims with a circular trajectory is shown in Fig. 7.6b. A circular swimming trajectory is shown in Fig. 7.6c, with a linear trajectory in Fig. 7.6d.

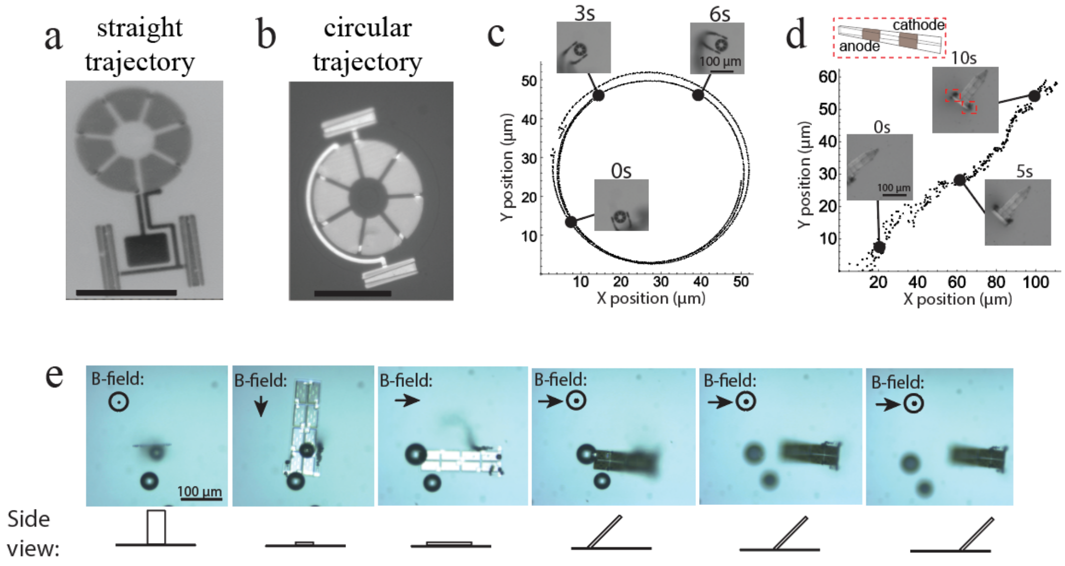

Figure 7.6: **Controlling the Trajectory of a Bubble Rocket. a)** Micrograph of a bubble rocket with a straight swimming trajectory. **b)** Micrograph of a bubble rocket with a circular swimming trajectory. **c)** Time lapse and corresponding circular trajectory of a microswimmer with separate anodic and cathodic rockets on a solid-liquid interface. **d)** Time lapse and corresponding straight trajectory of a microswimmer with each rocket containing both anode and cathode on a liquid-liquid interface. **e)** Microswimmer on a solid-liquid interface with thin film magnets rotating in three dimensions and locomoting with an attack angle of 45 degrees.

These devices can also be integrated with thin-film magnets and steered in a magnetic field. A device being rotated in three axes by a uniform magnetic field is shown in Fig. 7.6e. This microswimmer with a maximum device dimension of 210 µm ejects bubbles with a radius of 3.3 µm at a frequency of roughly 30 Hz. For frames 4-6, the device is tilted at a 45-degree angle.

Bubble rockets that do not move along a solid-liquid interface despite bubbling, such as the device in Fig. 7.6e, are very common. For this microswimmer, tilting the device enables it to move. We posit that devices that are immobile despite bubbling are weakly adhered to the surface by surface forces but are otherwise functional. After being angled upward, the device in Fig. 7.6e moves forward at a velocity of roughly 3 µm/s, similar to the 3 µm/s predicted by eq. 6.3.

7.6 Bubble Adhesion for Increased Propulsion

At this point, it may seem like interactions between microswimmers and nearby solid surfaces is only detrimental to their functionality. However, these interactions prove beneficial to microswimmers in one particular case, shown in Fig. 7.7. These microswimmers are fabricated slightly differently, with a comparison of device geometries shown in Fig. 7.7a. For most microswimmers shown thus far, the cross-section of the electrode-containing tube is a four-sided rectangle. In contrast, the swimmer shown in Fig. 7.7 was fabricated without a bottom section of the bubble tube, so the growing bubbles are bounded by the swimming surface on one side.

As the bubble grows in the tube, it becomes adhered to the surface on which the microswimmer is locomoting. The bubble remains adhered to the surface even as it is ejected from the tube. With each bubble ejection, the microswimmer moves a distance dependent only on the bubble radius instead of the relative Stokes forces.

The microswimmer shown in Fig. 7.7b is moving at about 60 μm/s on a solid-liquid interface, with its displacement vs. time plot shown in Fig. 7.7b. Behind the device is a trail of bubbles that remain stationary on the surface as the microswimmer moves forward, as seen in Fig. 7.7b. This microswimmer is ejecting bubbles with a mean radius of 2.5 μm at about 150 Hz, so the theoretical velocity for this device in bulk fluid (from eq. 6.3) is about 20 μm/s. For our bubble rockets, this is the only case in which microswimmer velocity exceeds that given by eq. 6.3. This method for bubble propulsion on a solid-liquid interface has not been seen before in the bubble rocket literature.

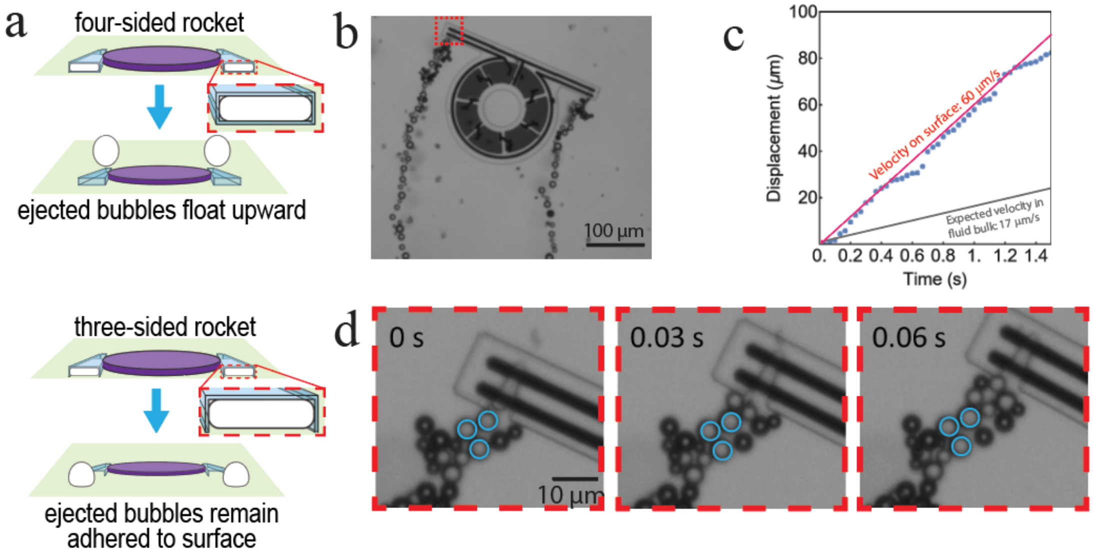

Figure 7.7: **Bubble Rocket Utilizing Bubble Surface Adhesion for Increased Swimming Velocity. a)** Diagram showing device geometry where ejected bubbles float upward (top) and where ejected bubbles remain adhered to the surface (bottom). **b)** Micrograph of microswimmer locomoting on glass-water interface with a trail of bubbles adhered to the surface behind it. **c)** Displacement as a function of time for device shown in (b) compared to maximum expected velocity using traditional bubble-propelled motion. **d)** Time lapse of device in (a) showing adhered bubbles outlined in blue.

7.7 Outlook for Microscopic Bubble Rockets

These microswimmers are the first microscopic robots that use onboard silicon electronics and optical power to drive bubble propulsion. These bubble rockets operate by splitting water and can therefore locomote in any aqueous solution. We demonstrate dynamic steering and pre-determined swimming trajectory, allowing advanced control of these robots. In a new development to bubble rocket research, we found that these devices can swim faster on a solid-liquid interface by using bubble adhesion to the surface as a new propulsion mechanism.

Similar to the autonomous microbots that utilize SEAs in Chapter 5, the ultimate goal for these bubble rockets is integration with CMOS circuitry for advanced control. To this end, we have partnered with the Molnar group at Cornell for the design of circuits that will enable advanced control of these devices. These advanced bubble rockets have an additional set of onboard electrodes or photodiodes to enable sensing of light and chemical gradients. The robots can then move toward or away from a light source or an increased concentration of redox molecules.

The circuits for these devices have been manufactured at a commercial foundry and the microswimmers are currently undergoing post-processing and characterization by Shahab Ghajari, a graduate student in the Molnar group. Like other microscopic robots whose circuits have been fabricated at a commercial foundry, such as those in Chapter 5, these microbots are fabricated in parallel. A micrograph showing an array of smart bubble rockets during fabrication is shown in Fig. 7.8a, with an SEM of an individual device in Fig. 7.8b.

In general, the circuits for these smart bubble rockets and those for the SEA

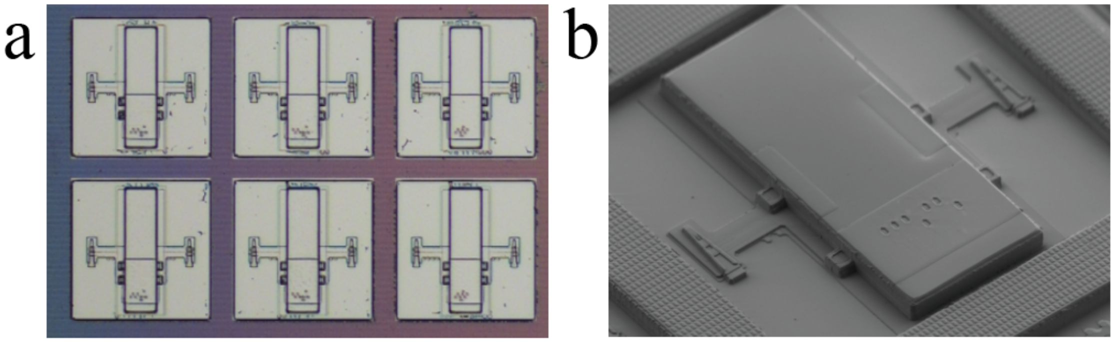

Figure 7.8: **Bubble Rockets with Onboard CMOS Circuits during Fabrication. a)** Optical micrograph showing smart bubble rockets arrayed during post-processing of samples from X-FAB. Image by Shahab Ghajari. **b)** SEM of a single smart bubble rocket prepared to be released from the substrate. Image by Shahab Ghajari.

microbots are very similar. Both circuits utilize an onboard clock, PTAT current source, and frequency divider. In addition, their fabrication approaches are so similar that they undergo simultaneous post-processing on the same wafer.

Much like the microbots previously discussed, we aim to use this platform for electrochemical propulsion as a launch point for microbots that can perform more complex tasks, interact with their environment, and communicate with the outside world. In addition to contributing to the field of microscopic robotics, this work on electrolytic bubble propulsion is also uniquely poised to contribute to the bubble rocket community. In the next chapter, we discuss how characterization of these bubble rockets sheds light on the electrochemical dynamics of gas-evolving reactions in confined geometries, such as microtubes.

CHAPTER 8

ELECTROCHEMISTRY OF A GAS-EVOLVING REACTION IN A MICROTUBE

In our discussion of water electrolysis-enabled microswimmers, we have glossed over two advantages of using voltage-driven electrolysis for bubble propulsion. One, bubble dynamics depend on the applied voltage, enabling advanced control over swimming behavior. Two, electrolytic bubble production allows us to study the current-voltage behavior of electrodes during bubble production, allowing insight into the electrochemical dynamics inside a tube during gas-evolving reactions.

In this chapter, we study the current-voltage behavior of rocket electrodes like those described in Chapter 7 and develop a model for the electrochemical dynamics of a bubble-producing microtube.

8.1 Basic Current-Voltage Behavior due to Bubbles

In order to study the electrochemical properties of a bubble rocket, we fabricate rocket electrodes on chip using the same process flow as described for the bubble-propelled microswimmers in Chapter 7. These electrodes are fabricated on a 20 mm square chip and are connected via lithographically patterned wires to macroscopic pads on the perimeter of the chip. The wires are insulated with SiO_2 and fluid is added to the center of the chip, such that the only metal exposed to fluid is the interior of the electrodes. Potentials are applied to a single electrode with respect to a Pt pseudo-reference in the electrolyte, and the current is measured with a transimpedance amplifier. Unless otherwise noted, these experiments are performed in 1 mM PBS solutions.

An optical micrograph and diagram of a bubble rocket as well as a measurement schematic are shown in Fig. 8.1a. These rockets, like those discussed in Chapter 7, are tapered hollow tubes with a rectangular cross-section. The metal electrodes are on the interior of the tube.

First, we sweep the potential on the rocket electrode at a constant rate of 100 mV/s and measure the resulting current. An I-V trace is shown in Fig. 8.1b. As the potential is increased to more positive values, the measured current remains near zero until the applied potential reaches about 1 V. At this point, the electrode potential is sufficient to drive water electrolysis, and the current begins to increase. At about 1.8 V, the current suddenly begins to fluctuate. This corresponds to the onset of bubble production and ejection from the tube.

This current-voltage behavior has significant implications for microscopic robots using bubbles for propulsion. Unlike other bubble rockets whose gas-evolving reactions proceed spontaneously, the bubble production efficiency of these microbots is zero unless they apply a voltage/current above the threshold needed for bubble production.

Fig. 8.1b shows I-V characteristics for both positive and negative applied potentials. For the rest of this chapter, we will focus primarily on positive applied potentials (O_2 production) while noting that similar behavior occurs at negative applied potentials (H_2 production).

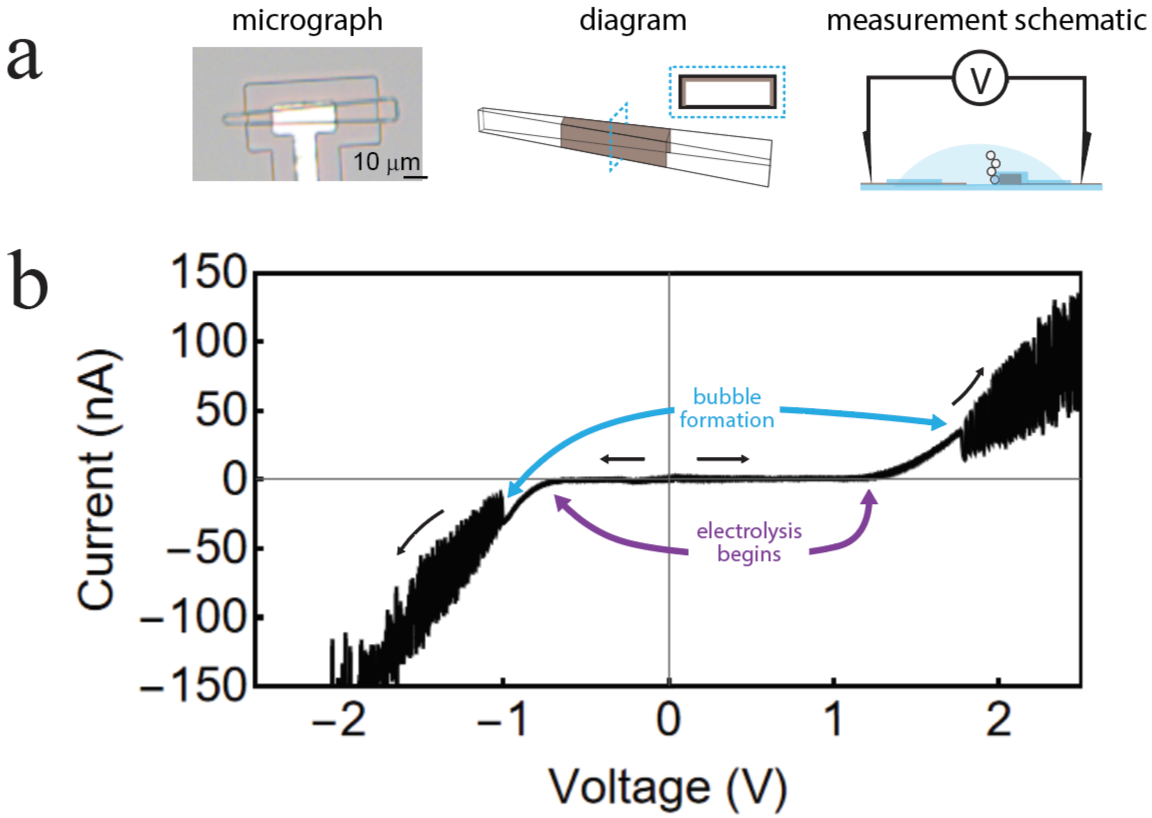

Figure 8.1: **I-V Characteristics of a Gas-Evolving Microtube Electrode.** **(a)** Microscope images and diagrams of on-chip bubble rocket and measurement scheme. **(b)** I-V curve of a bubble rocket showing the onset of electrolysis and bubble formation.

8.2 Current Fluctuations under DC Applied Potentials

The current measured on any rocket electrode producing and ejecting bubbles fluctuates similar to the trace shown in Fig. 8.1b. To further study these current fluctuations, we applied DC potentials to a bubble rocket and measured the current. These data are shown in Fig. 8.2a. First, we note that the frequency of these fluctuations increases with potential. The amplitude of these current fluctuations decreases slowly with time.

A more detailed current trace showing one fluctuation is shown in Fig. 8.2b. By performing simultaneous video and electrical measurements, we know that the frequency of these current fluctuations is the same as the frequency for bubble ejection. Further, from videos we know that the current during these fluctuations is at a maximum after a bubble is ejected from the tube, before a new one forms. We see what appears to be two different current states; a high-current state corresponding to no bubble in the tube, and a low-current state when the tube contains a bubble. Optical micrographs of a rocket electrode during bubble production and ejection are shown in Fig. 8.2c.

The dynamics inside a bubble rocket are complex, but we here attempt to relate these current fluctuations and other electrical characteristics of a bubble rocket to generic principles of electrochemistry.

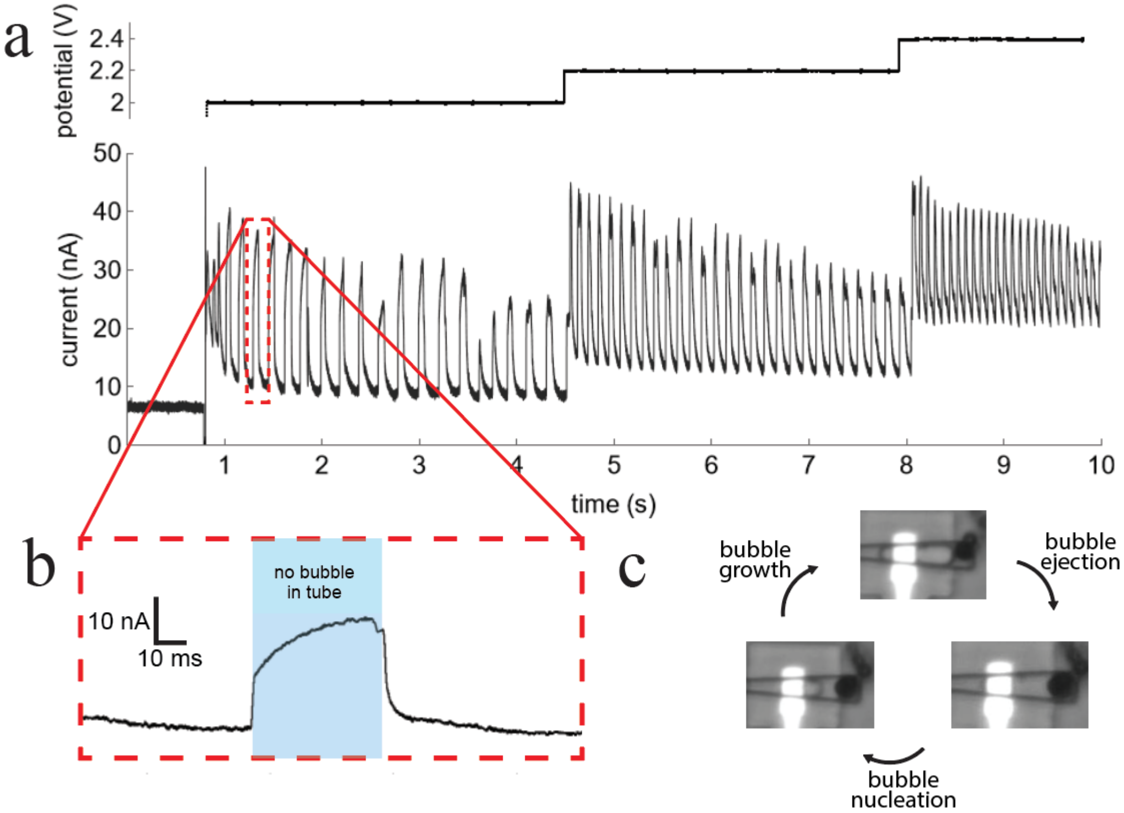

Figure 8.2: **Current Fluctuations on Bubble-Producing Electrode with DC Applied Potentials.** **(a)** Current fluctuations on a bubble rocket electrode while its applied potential is stepped from 2 to 2.4 V in steps of 0.2 V. **(b)** Inset of **a)** showing shape of one current fluctuation. **(c)** Optical micrographs showing the cycle of bubble nucleation, growth, and ejection.

8.3 Model of Resistances for Water Electrolysis

Here, we discuss the relative effects of both the fluid resistance R_F and the electrode-electrolyte resistance (also called charge-transfer resistance), R_{CT} on the I-V characteristics of a tube containing a metal electrode. These resistances are in series with each other. The applied voltage V_{APP} is the sum of the voltages across the electrode interface and the fluid,

$$V_{APP} = V_{CT} + V_F. \tag{8.1}$$

The fluid acts as an ohmic resistor, $V_F = iR_F$. Because the fluid and electrode-electrolyte interface are in series, the current i through these components is the same.

The dependence of the current i through the electrode-electrolyte interface with potential V_{CT} is more complex. This relationship is given by the Butler-Volmer equation:

$$i \propto e^{\alpha f(\eta_{conc} + V_{CT} - V_0)}. \tag{8.2}$$

Here, V_0 is the formal potential of the electrode, or the potential at which current begins to flow, $f = F/RT$ and α is the charge-transfer coefficient between 0 and 1 which describes the imbalance between the anodic and cathodic redox reactions; this is often taken to be 0.5, so we use the same value. η_{conc}, the concentration overpotential, represents the effect of nearby redox molecules on the electrode behavior. To understand η_{conc} for the reactions we've discussed so far, let's consider electrodes in water with a positive applied potential. These electrodes evolve oxygen gas: $2H_2O \rightarrow O_2 + 4H^+ + 4e^-$. For this oxygen evolution reaction, the concentrations of H_2O, O_2, and H^+ result in η_{conc} given by the Nernst equation as

$$\eta_{conc} = \frac{RT}{nF}\ln(\frac{[H^+]_{eq}^4[O_2]_{eq}[H_2O]^2}{[H^+]^4[O_2][H_2O]_{eq}^2}) = \frac{RT}{nF}\ln(\frac{[H^+]_{eq}^4}{[H^+]^4}) \tag{8.3}$$

Here we have neglected the $[H_2O]$ and $[O_2]$ terms. The concentration of water is constant. We neglect $[O_2]$ for simplicity – the effect of H^+ is much more pronounced as $[H^+]$ is raised to the fourth power. We can already see from eq. 8.2 that a changing concentration overpotential has the same effect on the current as changing the threshold voltage V_0. Eq. 8.2 can be inverted to give:

$$V_{CT} = \frac{1}{\alpha f}\ln i + V_0 - \eta_{conc}. \tag{8.4}$$

The complete relationship between the applied potential V_{APP} and the measured current i, then, is given by eq. 8.1 as:

$$V_{APP} = \frac{1}{\alpha f}\ln i + V_0 - \eta_{conc} + iR_F. \tag{8.5}$$

This implicit equation can be solved numerically, and the qualitative behavior is shown in Fig. 8.3. However, just by looking at eq. 8.5 we can gain an intuition for the effect of these impedances on the current. The logarithmic term in eq. 8.5 only matters at applied potentials near the formal potential ($V_{APP} \approx V_0$). However, the purpose of this chapter is to study bubble behavior, which occurs at applied potentials a few hundred mV above the formal potential. Near and above the bubble threshold, eq. 8.5 becomes

$$i = \frac{V_{APP} - V_0 + \eta_{conc}}{R_F}, \tag{8.6}$$

At high potentials, η_{conc} serves the same function as the formal potential, shifting the I-V curve to the left or right. The slope of the I-V line is the fluid conductance. We can see that even at extreme applied potentials where the charge-transfer resistance is low, changing ion concentrations near the electrode affects the current.

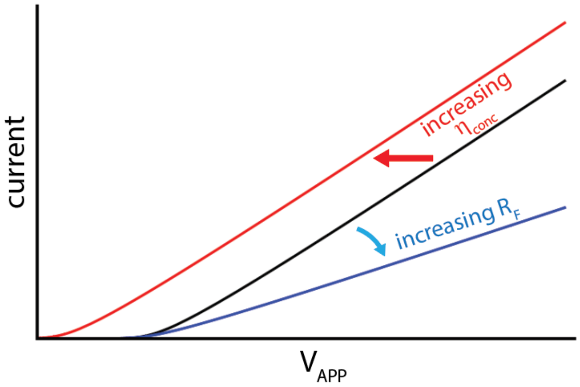

Figure 8.3: **Dependence of Measured Current on Electrode and Fluid Impedances.** Eq. 8.5 plotted for the current ratio i/i_0 as a function of V_{APP}.

8.4 Quantifying Ion Concentrations inside a Tube

So far, we have shown that the I-V characteristics of an electrode during water electrolysis depends on the concentration of ions near the electrode, particularly H^+ ions. Here, we develop a model for the H^+ concentration inside the microtubes.

First, we assume that the H^+ concentration in the tube varies length-wise, but not radially. We also assume that the H^+ concentration in the electrode section of the tube is homogenous and increases at a rate proportional to the current, and that ions diffuse a length L to leave the tube in some time τ. Here, L is the distance between the outside of the tube and the electrode section.

We can estimate τ by considering Fickian diffusion, where the flux J of ions out of the tube (number per unit area per unit time) is related to the diffusion coefficient D_0 and the concentration gradient $d[H^+]/dx$ by $J = -D_0\ d[H^+]/dx$. Assuming a very low ion concentration outside the tube and a uniform concentration gradient across the length L between the electrode and the outside of the tube, the diffusive time constant τ is $\tau = L^2/D_0$. For this system, a typical value for τ is about 50 ms.

The rate of change of $[H^+]$ then consists of a source term related to the current, and a sink term due to this diffusion. $d[H^+]/dt$ is

$$\frac{d[H^+]}{dt} = \frac{i\,n}{FV} - \frac{[H^+]}{\tau} \tag{8.7}$$

In the steady state, $\frac{d[H^+]}{dt} = 0$, so $\frac{i\,n}{FV} = \frac{[H^+]}{\tau}$. For any tube volume and current, we can then estimate the steady-state H^+ concentration. For instance, the device in Fig. 8.2b has a tube volume of about 1350 μm^3 and a current of about 30 nA in the high-current state. The steady-state H^+ concentration in this fluid-filled tube is about 10 mM, or a pH of about 2.6. During water electrolysis, the concentration of produced H^+ can approach or exceed the salt concentration in the electrolyte, affecting the fluid impedance.

8.5 Effect of a Bubble on Ion Concentration

Up until now, we have considered a fluid-filled microtube containing an electrode driving water electrolysis. We've discussed the effect of ion concentration on the electrode I-V characteristics and developed a model to estimate the steady-state H^+ concentration in such a tube. This discussion is valid for tubes in the high-current state as shown in Fig. 8.2 – that is, a tube with no bubble.

Now, we turn to discuss the other steady state of this system: the low-current state, when the tube contains a bubble. A bubble reduces the fluid volume in the tube, affecting the steady-state H^+ concentration as dictated by eq. 8.7. To estimate the volume of a tube with a bubble, we now consider the geometry of bubbles in tubes.

As a reminder, the cross section of these tubes is a rectangle; due to the finite surface tension of the bubble, there is still a conductive pathway between the electrode and the outside of the tube even when the bubble fills the tube. The exact shape of a bubble in a rectangular tube is complicated, but we approximate the cross section of a bubble in a tube of width w and height h as shown in Fig. 8.4a, an approximation used elsewhere in the literature[73]. The cross-sectional area A_{BOX} is simply $A_{BOX} = wh$, and the bubble cross-sectional area $A_{bubble} =$

$h(w-h)+\pi(h/2)^2$. The ratio A' of the fluid cross-sections is $A' = (A_{box} - A_{bubble})/A_{box}$. Fig. 8.4b shows a micrograph of a typical bubble rocket with the values of A' at two different positions on the rocket. We estimate A' to be about 0.1.

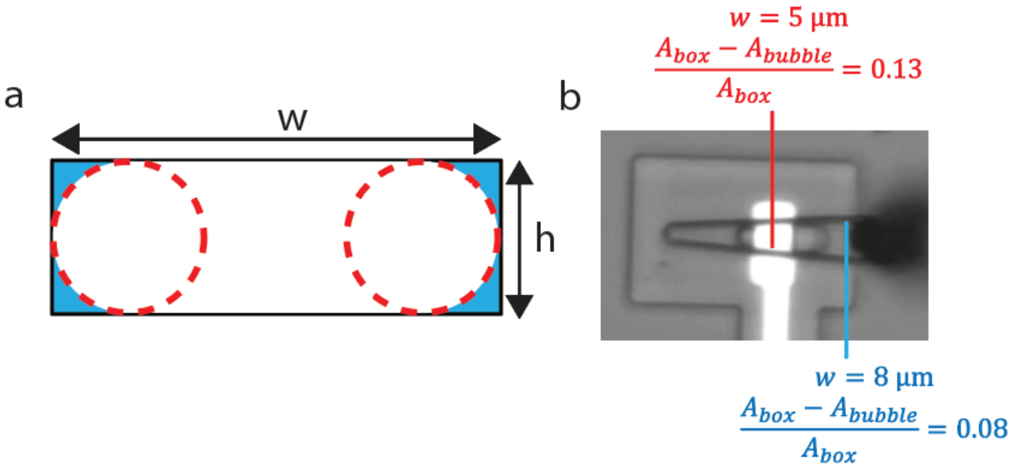

Figure 8.4: **Relevant Bubble Tube Dimensions.** **(a)** Cross-section of a bubble in a tube of width w and height h. **(b)** Ratio between fluid area with and without a bubble for two locations in the same bubble tube.

This factor of 10 decrease in fluid volume for the bubble-in-tube state is clearly a very rough estimate. This factor of 10 would increase if the bubble deforms to fill the tube corners, and decrease if the bubble is less than the length of the tube. This rough estimation, however, will allow us to make some estimations for expected ion concentration and I-V characteristics. From eq. 8.7, we know that a 10x smaller fluid volume means a 10x lower current is needed to support the same steady-state H^+ concentration. If we assume a similar current in the high- and low-current steady states, then eq. 8.7 predicts a 10x higher H^+ concentration for the bubble-in-tube state.

Now, we discuss the effect of this increased H^+ concentration on the fluid impedance and the concentration overpotential. The resistivity for 1 mM PBS is about 5×10^6 Ω µm. For a bubble-free tube, the fluid resistance between the electrode and the fluid bulk (outside of the tube) is about 4×10^6 Ω. If the fluid cross-sectional area is reduced by a factor of 10 due to a bubble, this fluid resistance increases to 4×10^7 Ω. As a reminder, the H^+ concentration the tube also affects impedance. In the data shown in Fig. 8.2b, a 2 V applied potential resulted in 50 nA of measured current, or about a measured resistance of 4×10^7 Ω as well. Because this estimated resistance is about the same as what we measure, the fluid impedance may play a role in the current fluctuations due to bubbles.

From eq. 8.3, a 10x higher H^+ concentration results in about a 60 mV increase in η_{conc}, the concentration overpotential. From the linearized current-voltage relationship in eq. 8.6 and given this range of values for R_F, we expect a change in the measured current of about 1.5 - 15 nA due to the change in concentration overpotential, about the same order of magnitude as the measured current fluctuation amplitude. Therefore, these current fluctuations may also be well-described by the changing concentration overpotential.

The presence of a bubble in a tube-like electrode increases both the fluid impedance and concentration overpotential of the electrode/tube system, and both of these effects may be important to the I-V characteristics measured here. Detangling the relative effects of these impedances requires additional experiments, but at this point we can begin to develop a model for what happens inside a tube during bubble ejection.

8.6 Ion Concentrations during Bubble Ejection

Now, we begin to identify more subtle features in the current fluctuations shown in Fig. 8.2b and relate these features to the impact a bubble has on the H^+ concentration in the tube, and therefore the current. We consider five stages of the bubble ejection/nucleation process, which are denoted by A-D in Fig. 8.5b.

A. **Bubble ejection.** When a bubble is ejected from a tube, more neutral pH fluid from outside the tube replenishes the tube and H^+ ions begin diffusing length-wise from the electrode area.

B. **Ion production in an empty tube.** The H^+ concentration, and therefore the current, begins to approach the steady state of an empty tube.

C. **Bubble nucleation.** Eventually, another bubble nucleates in the tube and grows rapidly, decreasing the fluid volume of the tube dramatically, therefore increasing H^+ concentration and narrowing the conduction pathway, both decreasing the current.

D. **Bubble has filled the tube.** Bubble occupies nearly the entire of the volume of the tube, suppressing the current, before being ejected.

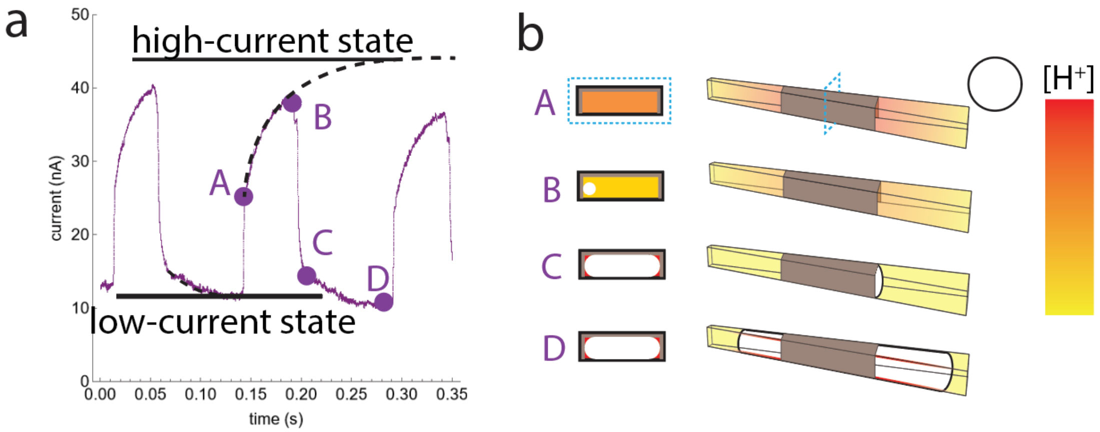

Figure 8.5: **Proposed Model for Current Fluctuations during Bubble Ejection.** **(a)** Current fluctuations under 2V applied potential in 1 mM PBS. **(b)** Graphical respresentation of tube (right) and cross-section (left) showing the bubble and H^+ concentrations denoted in **a.**

8.7 Current Density Required for Bubble Nucleation

The time for which a rocket is in the high-current state corresponds to the time between bubble ejection and the nucleation of a new bubble. The gas concentration inside the tube, then, should exceed the saturation concentration of O_2 in water, or about 1 mM. Similar to $[H^+]$ in eq. 8.7, we can calculate the steady-state O_2 concentration in the high-current state: $[O_2]_{SS} = \frac{in\tau}{FV}$. Compared to H^+, the stoichiometric ratio for the oxygen evolution reaction n and the diffusion coefficient D_0 for O_2 both decrease by about a factor of four. Since $n\tau \propto n/D_0$, the steady-state O_2 concentration is the same as the steady-state H^+ concentration, about 10 mM. This estimate for steady-state gas concentration inside the tube is in rough agreement with expected gas concentrations needed for nucleation, which typically exceed the saturation concentration by 1-2 orders of magnitude[74].

Next, we note that the concentration of oxygen molecules produced in the high-current state is proportional to the total charge passed Q divided by the fluid volume V of the electrode region. This quantity should be independent of electrode size. For simplicity, we disregard diffusion away from the electrode section of the tube. The charge Q is measured by multiplying the current ΔI and the time Δt in the high-current state as shown in Fig. 8.6. For this example, the measured current is about 35 nA on average for 50 ms on an electrode with width 30 μm. The total charge passed per unit volume, then, is 2×10^{-12} C/μm^3.

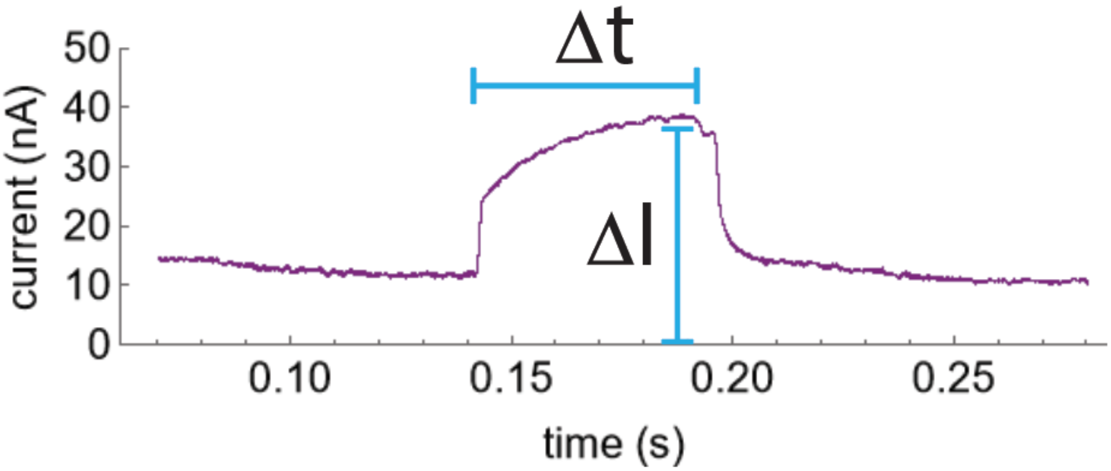

Figure 8.6: **Measuring the Charge Passed in the High-Current State.** ΔI and Δt for one period for a 30 μm electrode in a 50 μm tube.

We then performed the same analysis for a 5 μm wide electrode with an average measured current of 8 nA for 15 ms between the current increase and subsequent decrease, or 9×10^{-13} C/μm^3 charge density resulting in an O_2 concentration of 2 mM before bubble nucleation. Despite different applied potentials and a 6x difference in electrode size, the concentration of oxygen molecules produced in the electrode region in the high-current state only varies by a factor of 2.5x, and is consistent with the saturation concentration for O_2 in water.

Current traces at high bubble frequencies often contain other fluctuations and features that make it difficult to pinpoint bubble nucleation and ejection just by examining the current. For some traces, however, we can see by eye that the current and time are anticorrelated in the high-current state. In Fig. 8.2, especially under 2.2 V applied potential, we can see that the electrode spends more time in the high-current state as the total current decreases with time. Similarly, the time in the high-current state decreases with increased applied potential, as more current is passed. These findings are consistent with our understanding of bubble nucleation.

8.8 Outlook

Here, we've discussed some behavior of bubble-producing tube-shaped electrodes like those used for the microswimmers in Chapter 7. Specifically, we've discussed how the electrical characteristics of these electrodes depends on the presence or absence of a bubble in the tube. We've developed a basic model for bubble-induced ion depletion and replenishment to explain this behavior and discussed implications of this model.

This work benefits the development of future microscopic robots in a couple of ways. First, as a reminder, the current fluctuations discussed in this chapter occur with a DC applied signal. As such, these bubble rockets act like an oscillator reminiscent of those fabricated with more complicated circuitry earlier in this thesis. These oscillations are achieved without the use of a single transistor, and operate at low frequencies without a series of frequency dividers, paving the way for devices that utilize physical processes to generate a clock signal, which has been of interest recently[75].

In another envisioned application, microscopic robots could sense these current fluctuations to detect successful bubble ejection, providing real time feedback to onboard circuitry. More generally, understanding the interplay between bubble dynamics and the electrical characteristics of these electrodes is crucial for advanced control of bubble-propelled microscopic robots.

In addition, this work allows insight into bubble dynamics that was not possible in existing work. Until now, there was no way to perform measurements of chemical dynamics inside a tube during bubble propulsion. Here, we perform high-speed current measurements to illuminate bubble dynamics and ion diffusion in a gas-evolving tube-shaped electrode. This work opens the door to more advanced modeling and additional experiments to give unique insights into the electrochemistry of the bubble process.

CHAPTER 9

SUMMARY & OUTLOOK

At the beginning of this thesis, we sought to develop a microscopic toolkit for chemistry in very small fluid volumes. At the same time, we noted that the devices we use in our everyday life – smartphones, computers, vehicles – all consist of electronic components that are manufactured at the nanoscale. We proposed that this technology for miniaturized electronics could serve as a platform for performing chemistry in environments inaccessible to usual macroscopic techniques.

We began by discussing the tremendous world of applications for wirelessly powered microscopic devices in small fluid volumes, from implantable sensors to drug discovery to autonomous microscopic robots and beyond. We consider the ubiquity of electrochemically active fluids in the world around us, both natural and synthetic, and proposed electrochemistry as a way for microscopic electronics to interact with their chemical environments at the microscale.

Ultimately, we envisioned microscopic electronic devices that are powered by light and occupy a volume on the nanoliter scale. These devices would be capable of a wide range of functions – locomotion, chemical sensing, onboard computation, chemical synthesis, and wireless data transmission. We envisioned a technology that is manufactured the same way as the circuits that surround us in everyday life, enabling the advances made in microelectronics miniaturization to intersect with the demands of cutting edge research in biology and chemistry.

In Chapter 2, we developed optically powered microscale devices to drive electrochemical synthesis for drug discovery in the pharmaceutical industry. These devices, called SPECS, utilize onboard silicon photodiodes to drive electrochemical synthesis in high-throughput experimentation. This key innovation allows electrochemical synthesis reactions to be performed in high-throughput experiments. These devices are manufactured in massive parallel, resulting in a low-cost solution that is compatible with existing infrastructure for drug discovery.

In Chapter 3, we turned to discuss the emerging field of electrochemical sensors, with a focus on their miniaturization. We discussed the impact of local redox molecules on electrode behavior, enabling high-resolution chemical sensing. Finally, we discussed progress towards the development of truly microscopic electrochemical sensors, including a platform for wireless sensing developed at Cornell.

In Chapter 4, we showed the first steps toward a development of an optically powered microscopic electrochemical sensor. This sensor is designed to perform chemical measurements and communicate these data to the outside world by pulsing an onboard micro-LED. We performed initial testing of this sensor to demonstrate its ability to measure fluid salinity.

In Chapter 5, we turned to a discussion of electrochemical propulsion techniques for microscopic robotics. Specifically, we demonstrated fully autonomous microscopic robots that utilize electrochemical actuators to propel through fluid on a solid-liquid interface.

In Chapter 6, we discussed the physics and existing literature for another form of electrochemical propulsion: bubble ejection. These devices utilize gas-evolving reactions to produce and eject bubbles, propelling a microswimmer forward.

In Chapter 7, we developed optically powered bubble-propelled microswimmers. These devices consist of onboard silicon photodiodes that drive water-splitting under incident light. We demonstrated dynamic steering and trajectory control of these swimmers, and discovered a new method for bubble propulsion on solid-liquid interfaces. These are the first truly microscale bubble rockets with onboard silicon electronics, paving the way for integration of CMOS circuits with bubble propulsion.

In Chapter 8, we then measured the electrical characteristics of a gas-evolving tube-shaped electrode like those used in the microswimmers from Chapter 7. We were able to gain insight into the electrochemical dynamics of gas-evolving electrodes, advancing the scientific understanding of electrolytic bubbles and a crucial step toward advanced control of microscopic bubble-propelled robots.

In this work, we have shown a wide range of functionality for nanoliter electronic devices performing wireless chemistry. For instance, we've demonstrated chemical synthesis and sensing, onboard computation, and locomotion. All of these devices are wirelessly powered using light, and interact with their environment using electrochemistry.

All of the work described here is further compatible with standard approaches for the fabrication of microelectronics, allowing integration of more complex circuit components limited only by the desired footprint of the device. Ultimately, the types of advancements made here in the miniaturization of electronic devices for wireless chemistry will drive further innovation toward a microscopic toolkit used for a range of applications.

BIBLIOGRAPHY

[1] Maggie Villager. *Well Plates*. National Center for Advancing Translational Sciences.

[2] Products: Lumidox® LED Arrays Lamps - Lumidox® II - Analytical Sales and Services, Inc. — analytical-sales.com. https://www.analytical-sales.com/product-category/photoredox-parallel-synthesis/lumidox-led-arrays-lamps/lumidox-ii/. [Accessed 31-Dec-2022].

[3] Jonas Rein, James R. Annand, Michael K. Wismer, Jiantao Fu, Juno C. Siu, Artis Klapars, Neil A. Strotman, Dipannita Kalyani, Dan Lehnherr, and Song Lin. Unlocking the potential of high-throughput experimentation for electrochemistry with a standardized microscale reactor. *ACS Central Science*, 7(8):1347–1355, August 2021.

[4] Analyzing Cyclic Voltammetry at a Microdisk Electrode with Simulation — comsol.com. https://www.comsol.com/blogs/analyzing-cyclic-voltammetry-at-a-microdisk-electrode-with-simulation/. [Accessed 30-Dec-2022].

[5] Methods — Bioénergétique et Ingénierie des Protéines (BIP) — bip.cnrs.fr. https://bip.cnrs.fr/groups/bip08/methods/. [Accessed 30-Dec-2022].

[6] Ivan Ny Hanitra, Francesca Criscuolo, Nadezda Pankratova, Sandro Carrara, and Giovanni De Micheli. Multichannel front-end for electrochemical sensing of metabolites, drugs, and electrolytes. *IEEE Sensors Journal*, 20(7):3636–3645, April 2020.

[7] FreeStyle Libre 2 System — CGM with Real-Time Glucose Alarms — freestyle.abbott. https://www.freestyle.abbott/us-en/products/freestyle-libre-2.html. [Accessed 31-Dec-2022].

[8] Yu-Te Liao, Huanfen Yao, Andrew Lingley, Babak Parviz, and Brian P. Otis. A 3-$\mu\hbox{w}$ CMOS glucose sensor for wireless contact-lens tear glucose monitoring. *IEEE Journal of Solid-State Circuits*, 47(1):335–344, January 2012.

[9] B. Gil, S. Anastasova, and G.-Z. Yang. Low-powered implantable devices activated by ultrasonic energy transfer for physiological monitoring in soft tissue via functionalized electrochemical electrodes. *Biosensors and Bioelectronics*, 182:113175, June 2021.

[10] Tucker Stuart, William J. Jeang, Richard A. Slivicki, Bobbie J. Brown, Alex Burton, Victoria E. Brings, Lilian C. Alarcón-Segovia, Prophecy Agyare, Savanna Ruiz, Amanda Tyree, Lindsay Pruitt, Surabhi Madhvapathy, Martin Niemiec, James Zhuang, Siddharth Krishnan, Bryan A. Copits, John A. Rogers, Robert W. Gereau, Vijay K. Samineni, Amay J. Bandodkar, and Philipp Gutruf. Wireless, battery-free implants for electrochemical catecholamine sensing and optogenetic stimulation. *ACS Nano*, December 2022.

[11] M. Mujeeb-U-Rahman, Meisam Honarvar Nazari, and M. Sencan. A novel semiconductor based wireless electrochemical sensing platform for chronic disease management. *Biosensors and Bioelectronics*, 124-125:66–74, January 2019.

[12] Sunwoo Lee, Alejandro Javier Cortese, Aaron Mok, Chunyan Wu, Tianyu Wang, Ju Uhn Park, Conrad Smart, Shahaboddin Ghajari, Devesh Khilwani, Sanaz Sadeghi, Yanxin Ji, Jesse H. Goldberg, Chris Xu, Paul L. McEuen, and Alyosha Christopher Molnar. Fabrication of injectable microscale opto- electronically transduced electrodes (MOTEs) for physiological monitoring. *Journal of Microelectromechanical Systems*, 29(5):720–726, October 2020.

[13] Michael F. Reynolds, Alejandro J. Cortese, Qingkun Liu, Zhangqi Zheng, Wei Wang, Samantha L. Norris, Sunwoo Lee, Marc Z. Miskin, Alyosha C. Molnar, Itai Cohen, and Paul L. McEuen. Microscopic robots with onboard digital control. *Science Robotics*, 7(70), September 2022.

[14] Marc Z. Miskin, Alejandro J. Cortese, Kyle Dorsey, Edward P. Esposito, Michael F. Reynolds, Qingkun Liu, Michael Cao, David A. Muller, Paul L. McEuen, and Itai Cohen. Electronically integrated, mass-manufactured, microscopic robots. *Nature*, 584(7822):557–561, August 2020.

[15] Alexander A. Solovev, Yongfeng Mei, Esteban Bermúdez Ureña, Gaoshan Huang, and Oliver G. Schmidt. Catalytic microtubular jet engines self-propelled by accumulated gas bubbles. *Small*, 5(14):1688–1692, July 2009.

[16] Jinxing Li, Gaoshan Huang, Mengmeng Ye, Menglin Li, Ran Liu, and Yongfeng Mei. Dynamics of catalytic tubular microjet engines: Dependence on geometry and chemical environment. *Nanoscale*, 3(12):5083, 2011.

[17] Wei Gao, Renfeng Dong, Soracha Thamphiwatana, Jinxing Li, Weiwei Gao, Liangfang Zhang, and Joseph Wang. Artificial micromotors in the mouse's

stomach: A step toward in vivo use of synthetic motors. *ACS Nano*, 9(1):117–123, January 2015.

[18] Diana Vilela, Morgan M. Stanton, Jemish Parmar, and Samuel Sánchez. Microbots decorated with silver nanoparticles kill bacteria in aqueous media. *ACS Applied Materials &amp Interfaces*, 9(27):22093–22100, June 2017.

[19] Yin Chen, Huanhua Yang, Mingliang Li, Shilu Zhu, Shuo Chen, Liuyi Dong, Fuzhou Niu, and Runhuai Yang. 3d-printed light-driven microswimmer with built-in micromotors. *Advanced Materials Technologies*, 7(1):2100687, September 2021.

[20] Annie Xi Lu, Yijing Liu, Hyuntaek Oh, Ankit Gargava, Eric Kendall, Zhihong Nie, Don L. DeVoe, and Srinivasa R. Raghavan. Catalytic propulsion and magnetic steering of soft, patchy microcapsules: Ability to pick-up and drop-off microscale cargo. *ACS Applied Materials &amp Interfaces*, 8(24):15676–15683, June 2016.

[21] Laura Riva, Shuofeng Yuan, Xin Yin, Laura Martin-Sancho, Naoko Matsunaga, Lars Pache, Sebastian Burgstaller-Muehlbacher, Paul D. De Jesus, Peter Teriete, Mitchell V. Hull, Max W. Chang, Jasper Fuk-Woo Chan, Jianli Cao, Vincent Kwok-Man Poon, Kristina M. Herbert, Kuoyuan Cheng, Tu-Trinh H. Nguyen, Andrey Rubanov, Yuan Pu, Courtney Nguyen, Angela Choi, Raveen Rathnasinghe, Michael Schotsaert, Lisa Miorin, Marion Dejosez, Thomas P. Zwaka, Ko-Yung Sit, Luis Martinez-Sobrido, Wen-Chun Liu, Kris M. White, Mackenzie E. Chapman, Emma K. Lendy, Richard J. Glynne, Randy Albrecht, Eytan Ruppin, Andrew D. Mesecar, Jeffrey R. Johnson, Christopher Benner, Ren Sun, Peter G. Schultz, Andrew I. Su, Adolfo García-Sastre, Arnab K. Chatterjee, Kwok-Yung Yuen, and Sumit K. Chanda. Discovery of SARS-CoV-2 antiviral drugs through large-scale compound repurposing. *Nature*, 586(7827):113–119, July 2020.

[22] Elon Musk and Neuralink. An integrated brain-machine interface platform with thousands of channels. *Journal of Medical Internet Research*, 21(10):e16194, October 2019.

[23] Dongjin Seo, Ryan M. Neely, Konlin Shen, Utkarsh Singhal, Elad Alon, Jan M. Rabaey, Jose M. Carmena, and Michel M. Maharbiz. Wireless recording in the peripheral nervous system with ultrasonic neural dust. *Neuron*, 91(3):529–539, August 2016.

[24] Xing Chen, Babak Assadsangabi, Daniel Brox, York Hsiang, and Kenichi Takahata. A pressure-sensing smart stent compatible with angioplasty pro-

cedure and its in vivo testing. In *2017 IEEE 30th International Conference on Micro Electro Mechanical Systems (MEMS)*. IEEE, January 2017.

[25] Robert Herbert, Hyo-Ryoung Lim, Bruno Rigo, and Woon-Hong Yeo. Fully implantable wireless batteryless vascular electronics with printed soft sensors for multiplex sensing of hemodynamics. *Science Advances*, 8(19), May 2022.

[26] Sara Azimi, Allahyar Golabchi, Abdolhossein Nekookar, Shahram Rabbani, Morteza Hassanpour Amiri, Kamal Asadi, and Mohammad Mahdi Abolhasani. Self-powered cardiac pacemaker by piezoelectric polymer nanogenerator implant. *Nano Energy*, 83:105781, May 2021.

[27] You Yu, Joanna Nassar, Changhao Xu, Jihong Min, Yiran Yang, Adam Dai, Rohan Doshi, Adrian Huang, Yu Song, Rachel Gehlhar, Aaron D. Ames, and Wei Gao. Biofuel-powered soft electronic skin with multiplexed and wireless sensing for human-machine interfaces. *Science Robotics*, 5(41), April 2020.

[28] Yeongin Kim, Jun Min Suh, Jiho Shin, Yunpeng Liu, Hanwool Yeon, Kuan Qiao, Hyun S. Kum, Chansoo Kim, Han Eol Lee, Chanyeol Choi, Hyunseok Kim, Doyoon Lee, Jaeyong Lee, Ji-Hoon Kang, Bo-In Park, Sungsu Kang, Jihoon Kim, Sungkyu Kim, Joshua A. Perozek, Kejia Wang, Yongmo Park, Kumar Kishen, Lingping Kong, Tomás Palacios, Jungwon Park, Min-Chul Park, Hyung jun Kim, Yun Seog Lee, Kyusang Lee, Sang-Hoon Bae, Wei Kong, Jiyeon Han, and Jeehwan Kim. Chip-less wireless electronic skins by remote epitaxial freestanding compound semiconductors. *Science*, 377(6608):859–864, August 2022.

[29] Jihun Park, Joohee Kim, So-Yun Kim, Woon Hyung Cheong, Jiuk Jang, Young-Geun Park, Kyungmin Na, Yun-Tae Kim, Jun Hyuk Heo, Chang Young Lee, Jung Heon Lee, Franklin Bien, and Jang-Ung Park. Soft, smart contact lenses with integrations of wireless circuits, glucose sensors, and displays. *Science Advances*, 4(1), January 2018.

[30] Naïg Aurelia Ludmilla Chenais, Marta Jole Ildelfonsa Airaghi Leccardi, and Diego Ghezzi. Photovoltaic retinal prosthesis restores high-resolution responses to single-pixel stimulation in blind retinas. *Communications Materials*, 2(1), March 2021.

[31] C. Wyatt Shields IV, Catherine D. Reyes, and Gabriel P. López. Microfluidic cell sorting: a review of the advances in the separation of cells from debulking to rare cell isolation. *Lab on a Chip*, 15(5):1230–1249, 2015.

[32] Vasant Iyer, Zijian Yang, Jina Ko, Ralph Weissleder, and David Issadore. Advancing microfluidic diagnostic chips into clinical use: a review of current challenges and opportunities. *Lab on a Chip*, 22(17):3110–3121, 2022.

[33] Alejandro J. Cortese, Conrad L. Smart, Tianyu Wang, Michael F. Reynolds, Samantha L. Norris, Yanxin Ji, Sunwoo Lee, Aaron Mok, Chunyan Wu, Fei Xia, Nathan I. Ellis, Alyosha C. Molnar, Chris Xu, and Paul L. McEuen. Microscopic sensors using optical wireless integrated circuits. *Proceedings of the National Academy of Sciences*, 117(17):9173–9179, April 2020.

[34] Jack W. Scannell, Alex Blanckley, Helen Boldon, and Brian Warrington. Diagnosing the decline in pharmaceutical r&ampd efficiency. *Nature Reviews Drug Discovery*, 11(3):191–200, March 2012.

[35] Wei Gao, Daniel Kagan, On Shun Pak, Corbin Clawson, Susana Campuzano, Erdembileg Chuluun-Erdene, Erik Shipton, Eric E. Fullerton, Liangfang Zhang, Eric Lauga, and Joseph Wang. Cargo-towing fuel-free magnetic nanoswimmers for targeted drug delivery. *Small*, 8(3):460–467, December 2011.

[36] Steven M. Mennen, Carolina Alhambra, C. Liana Allen, Mario Barberis, Simon Berritt, Thomas A. Brandt, Andrew D. Campbell, Jesús Castañón, Alan H. Cherney, Melodie Christensen, David B. Damon, J. Eugenio de Diego, Susana García-Cerrada, Pablo García-Losada, Rubén Haro, Jacob Janey, David C. Leitch, Ling Li, Fangfang Liu, Paul C. Lobben, David W. C. MacMillan, Javier Magano, Emma McInturff, Sebastien Monfette, Ronald J. Post, Danielle Schultz, Barbara J. Sitter, Jason M. Stevens, Iulia I. Strambeanu, Jack Twilton, Ke Wang, and Matthew A. Zajac. The evolution of high-throughput experimentation in pharmaceutical development and perspectives on the future. *Organic Process Research &amp Development*, 23(6):1213–1242, May 2019.

[37] Melani G. Sullivan, Henry Utomo, Paul J. Fagan, and Michael D. Ward. Automated electrochemical analysis with combinatorial electrode arrays. *Analytical Chemistry*, 71(19):4369–4375, August 1999.

[38] Allen J. and Larry R Faulkner. *Electrochemical Methods*. John Wiley & Sons, Nashville, TN, 2 edition, December 2000.

[39] Petr V. Dudin, Michael E. Snowden, Julie V. Macpherson, and Patrick R. Unwin. Electrochemistry at nanoscale electrodes: Individual single-walled carbon nanotubes (SWNTs) and SWNT-templated metal nanowires. *ACS Nano*, 5(12):10017–10025, November 2011.

[40] Tom Terlouw, Christian Bauer, Russell McKenna, and Marco Mazzotti. Large-scale hydrogen production ivia/i water electrolysis: a techno-economic and environmental assessment. *Energy &amp Environmental Science*, 15(9):3583–3602, 2022.

[41] Chengzhou Zhu, Guohai Yang, He Li, Dan Du, and Yuehe Lin. Electrochemical sensors and biosensors based on nanomaterials and nanostructures. *Analytical Chemistry*, 87(1):230–249, December 2014.

[42] Eun-Hyung Yoo and Soo-Youn Lee. Glucose biosensors: An overview of use in clinical practice. *Sensors*, 10(5):4558–4576, may 2010.

[43] Kwang Bok Kim, Won-Chul Lee, Chul-Ho Cho, Deog-Su Park, Seong Je Cho, and Yoon-Bo Shim. Continuous glucose monitoring using a microneedle array sensor coupled with a wireless signal transmitter. *Sensors and Actuators B: Chemical*, 281:14–21, February 2019.

[44] Amay J. Bandodkar, Denise Molinnus, Omar Mirza, Tomás Guinovart, Joshua R. Windmiller, Gabriela Valdés-Ramírez, Francisco J. Andrade, Michael J. Schöning, and Joseph Wang. Epidermal tattoo potentiometric sodium sensors with wireless signal transduction for continuous non-invasive sweat monitoring. *Biosensors and Bioelectronics*, 54:603–609, April 2014.

[45] A.M.Vinu Mohan, Vinoth Rajendran, Rupesh K. Mishra, and Mathiyarasu Jayaraman. Recent advances and perspectives in sweat based wearable electrochemical sensors. *TrAC Trends in Analytical Chemistry*, 131:116024, October 2020.

[46] Alan S. Campbell, Jayoung Kim, and Joseph Wang. Wearable electrochemical alcohol biosensors. *Current Opinion in Electrochemistry*, 10:126–135, August 2018.

[47] Tamoghna Saha, Tanner Songkakul, Charles T. Knisely, Murat A. Yokus, Michael A. Daniele, Michael D. Dickey, Alper Bozkurt, and Orlin D. Velev. Wireless wearable electrochemical sensing platform with zero-power osmotic sweat extraction for continuous lactate monitoring. *ACS Sensors*, 7(7):2037–2048, July 2022.

[48] Yongkuk Lee, Connor Howe, Saswat Mishra, Dong Sup Lee, Musa Mahmood, Matthew Piper, Youngbin Kim, Katie Tieu, Hun-Soo Byun, James P. Coffey, Mahdis Shayan, Youngjae Chun, Richard M. Costanzo, and Woon-

Hong Yeo. Wireless, intraoral hybrid electronics for real-time quantification of sodium intake toward hypertension management. *Proceedings of the National Academy of Sciences*, 115(21):5377–5382, May 2018.

[49] Puchakayala Swetha, Umamahesh Balijapalli, and Shien-Ping Feng. Wireless accessing of salivary biomarkers based wearable electrochemical sensors: A mini-review. *Electrochemistry Communications*, 140:107314, July 2022.

[50] Rongfeng Li, Hui Qi, Yuan Ma, Yuping Deng, Shengnan Liu, Yongsheng Jie, Jinzhu Jing, Jinlong He, Xu Zhang, Laura Wheatley, Congxi Huang, Xing Sheng, Milin Zhang, and Lan Yin. A flexible and physically transient electrochemical sensor for real-time wireless nitric oxide monitoring. *Nature Communications*, 11(1), June 2020.

[51] Zhibin Xiao, Xi Tan, Xianliang Chen, Sizheng Chen, Zijian Zhang, Hualei Zhang, Junyu Wang, Yue Huang, Peng Zhang, Lirong Zheng, and Hao Min. An implantable RFID sensor tag toward continuous glucose monitoring. *IEEE Journal of Biomedical and Health Informatics*, pages 1–1, 2015.

[52] C. Mc Caffrey, K. Twomey, and V.I. Ogurtsov. Development of a wireless swallowable capsule with potentiostatic electrochemical sensor for gastrointestinal track investigation. *Sensors and Actuators B: Chemical*, 218:8–15, October 2015.

[53] M. Mujeeb-U-Rahman, Meisam. Honarvar Nazari, M. Sencan, and William Van Antwerp. A novel needle-injectable millimeter scale wireless electrochemical glucose sensing platform for artificial pancreas applications. *Scientific Reports*, 9(1), November 2019.

[54] Katharina Melzer, Marcel Brändlein, Bogdan Popescu, Dan Popescu, Paolo Lugli, and Giuseppe Scarpa. Characterization and simulation of electrolyte-gated organic field-effect transistors. *Faraday Discuss.*, 174:399–411, June 2014.

[55] Berta Esteban-Fernández de Ávila, Pavimol Angsantikul, Jinxing Li, Miguel Angel Lopez-Ramirez, Doris E. Ramírez-Herrera, Soracha Thamphiwatana, Chuanrui Chen, Jorge Delezuk, Richard Samakapiruk, Valentin Ramez, Marygorret Obonyo, Liangfang Zhang, and Joseph Wang. Micromotor-enabled active drug delivery for in vivo treatment of stomach infection. *Nature Communications*, 8(1), August 2017.

[56] Wei Gao, Xiaomiao Feng, Allen Pei, Yonge Gu, Jinxing Li, and Joseph

Wang. Seawater-driven magnesium based janus micromotors for environmental remediation. *Nanoscale*, 5(11):4696, 2013.

[57] K. Jagajjanani Rao, Fei Li, Long Meng, Hairong Zheng, Feiyan Cai, and Wei Wang. A force to be reckoned with: A review of synthetic microswimmers powered by ultrasound. *Small*, 11(24):2836–2846, April 2015.

[58] Baohu Dai, Jizhuang Wang, Ze Xiong, Xiaojun Zhan, Wei Dai, Chien-Cheng Li, Shien-Ping Feng, and Jinyao Tang. Programmable artificial phototactic microswimmer. *Nature Nanotechnology*, 11(12):1087–1092, October 2016.

[59] Tianlong Li, Jinxing Li, Hongtao Zhang, Xiaocong Chang, Wenping Song, Yanan Hu, Guangbin Shao, Elodie Sandraz, Guangyu Zhang, Longqiu Li, and Joseph Wang. Magnetically propelled fish-like nanoswimmers. *Small*, 12(44):6098–6105, September 2016.

[60] Leonardo Ricotti, Barry Trimmer, Adam W. Feinberg, Ritu Raman, Kevin K. Parker, Rashid Bashir, Metin Sitti, Sylvain Martel, Paolo Dario, and Arianna Menciassi. Biohybrid actuators for robotics: A review of devices actuated by living cells. *Science Robotics*, 2(12), November 2017.

[61] Qingkun Liu, Wei Wang, Michael F. Reynolds, Michael C. Cao, Marc Z. Miskin, Tomas A. Arias, David A. Muller, Paul L. McEuen, and Itai Cohen. Micrometer-sized electrically programmable shape-memory actuators for low-power microrobotics. *Science Robotics*, 6(52), March 2021.

[62] Wei Wang, Qingkun Liu, Ivan Tanasijevic, Michael F. Reynolds, Alejandro J. Cortese, Marc Z. Miskin, Michael C. Cao, David A. Muller, Alyosha C. Molnar, Eric Lauga, Paul L. McEuen, and Itai Cohen. Cilia metasurfaces for electronically programmable microfluidic manipulation. *Nature*, 605(7911):681–686, May 2022.

[63] Yuting Zhou, Liguo Dai, and Niandong Jiao. Review of bubble applications in microrobotics: Propulsion, manipulation, and assembly. *Micromachines*, 13(7):1068, July 2022.

[64] Jemish Parmar, Diana Vilela, and Samuel Sanchez. Tubular microjets: Fabrication, factors affecting the motion and mechanism of propulsion. *The European Physical Journal Special Topics*, 225(11-12):2255–2267, November 2016.

[65] Giacomo Gallino, François Gallaire, Eric Lauga, and Sebastien Michelin.

Physics of bubble-propelled microrockets. *Advanced Functional Materials*, 28(25):1800686, 2018.

[66] Tobias Metz, Nils Paust, Roland Zengerle, and Peter Koltay. Capillary driven movement of gas bubbles in tapered structures. *Microfluidics and Nanofluidics*, 9(2-3):341–355, December 2009.

[67] Liangxing Hu, Kai Tao, Jianmin Miao, and Gerhard Grüber. Hydrogen-peroxide-fuelled platinum–nickel–SU-8 microrocket with steerable propulsion using an eccentric nanoengine. *RSC Advances*, 6(104):102513–102518, 2016.

[68] Davide Pantarotto, Wesley R. Browne, and Ben L. Feringa. Autonomous propulsion of carbon nanotubes powered by a multienzyme ensemble. *Chem. Commun.*, (13):1533–1535, 2008.

[69] Jian-Yu Hsieh, Po-Hung Kuo, Yi-Chun Huang, Yu-Jie Huang, Rong-Da Tsai, Tao Wang, Hung-Wei Chiu, Yao-Hung Wang, and Shey-Shi Lu. A remotely-controlled locomotive IC driven by electrolytic bubbles and wireless powering. *IEEE Transactions on Biomedical Circuits and Systems*, 8(6):787–798, December 2014.

[70] Vladimir M. Fomin, Markus Hippler, Veronika Magdanz, Lluis Soler, Samuel Sanchez, and Oliver G. Schmidt. Propulsion mechanism of catalytic microjet engines. *IEEE Transactions on Robotics*, 30(1):40–48, February 2014.

[71] Zhihua Lin, Changyong Gao, Daolin Wang, and Qiang He. Bubble-propelled janus gallium/zinc micromotors for the active treatment of bacterial infections. *Angewandte Chemie*, 133(16):8832–8836, March 2021.

[72] Liqiang Ren, Nitesh Nama, Jeffrey M. McNeill, Fernando Soto, Zhifei Yan, Wu Liu, Wei Wang, Joseph Wang, and Thomas E. Mallouk. 3d steerable, acoustically powered microswimmers for single-particle manipulation. *Science Advances*, 5(10), October 2019.

[73] Mirco Magnini. Bubbles in capillaries: Relaxing traditional assumptions. *Science Talks*, 2:100020, June 2022.

[74] Qianjin Chen, Long Luo, Hamaseh Faraji, Stephen W. Feldberg, and Henry S. White. Electrochemical measurements of single hsub2/sub nanobubble nucleation and stability at pt nanoelectrodes. *The Journal of Physical Chemistry Letters*, 5(20):3539–3544, October 2014.

[75] Jing Fan Yang, Thomas A. Berrueta, Allan M. Brooks, Albert Tianxiang Liu, Ge Zhang, David Gonzalez-Medrano, Sungyun Yang, Volodymyr B. Koman, Pavel Chvykov, Lexy N. LeMar, Marc Z. Miskin, Todd D. Murphey, and Michael S. Strano. Emergent microrobotic oscillators via asymmetry-induced order. *Nature Communications*, 13(1), October 2022.